ION-BEAM-INDUCED MODIFICATIONS OF THIN FILM STRUCTURES AND FORMATION OF METASTABLE PHASES

Thesis by

Bor-Yeu Tsaur

In Partial Fulfillment of the Requirements

for the Degree of

Doctor of Philosophy

California Institute of Technology

Pasadena, California

1980

(Submitted April 21, 1980)

ACKNOWLEDGMENTS

It gives me great pleasure to express my profound appreciation to Prof. James W. Mayer and Prof. Marc-A. Nicolet for their guidance, encouragement, incessant advice and support throughout the course of this work. It has been a pleasant and unforgettable experience working in the solid state group under their supervision.

Part of work reported here was performed with Dr. Silvanus S. Lau, Dr. Zong-Long Liau and Dr. King-Ning Tu. I was really privileged to have worked with them. My sincere appreciation to them. I also wish to thank Drs. Walter L. Brown, Samuel E. Matteson, John M. Poate, Chang C. Tsuei and Martin van Allmen for their interest and many fruitful discussions.

Special thanks go to Prof. Thad Vreeland Jr. for his help and guidance in using the Siemens transmission electron microscope and x-ray diffraction facilities. I am also indebted to Prof. William L. Johnson for giving me access to the superconducting transition temperature measurement equipment. Dr. Joseph D. Graczyk and Mr. Tan-Tsu Sheng are gratefully acknowledged for the contributions of part of TEM analysis.

I would like to express my appreciation to Rouel Fernandez, Rob Gorris, Jeff J. Mallory and Daniel G. Tonn for outstanding technical work and to Mrs. Michell L. Parks and Vere Snell for kind assistance in typing the manuscript.

The financial support received from the California Institute of Technology, the Office of Naval Research, the International Business

Machines Corporation and the Office of Army Research is deeply appreciated.

Finally, I wish to thank my parents and my fiancee, Jennifer, for their spiritual support and patience.

ABSTRACT

The influences of energetic ion bombardment on the composition and structure of thin film materials and the utilization of ion-beam-mixing techniques to produce compounds and alloys are reported in this thesis.

Motivated by recent experimental observations that ion bombardment can induce alteration of atomic distributions in composite materials, a systematic study of ion-induced modification of interface profile and structure has been carried out. By bombarding through a thin transition-metal film deposited on a Si substrate, significant atomic mixing was observed near the metal-Si interface at dose levels of $\sim 10^{15} cm^{-2}$. The atomic mixing led to the formation of well-defined silicide phases which are identical to those obtained by normal thermal treatment. A macroscopic model based on collision-cascade mixing and radiation-enhanced diffusion mechanisms was proposed to account for the ion-induced interface reaction. The mixing process and its products were found to be strongly influenced by the implantation conditions such as ion energy, mass, fluence and sample temperature, as well as by the intrinsic properties of target material such as thermal diffusivity and radiation stability. Ion-beam-mixing at higher ion doses ($\sim 10^{16} cm^{-2}$) led to the formation of more Si-rich phases or disordered metal-Si layers which are difficult to form or, in some cases, inaccessible by normal thermal process. The phenomenon of ion-induced silicide formation is similar to that observed in thermal

annealing except that the radiation stability of phase structure is important in determining whether a silicide phase is formed or a disordered metal-Si mixture is formed. (Chapter 2)

The ion-beam-mixing process was then utilized to investigate the production of nonequilibrium (or metastable) phases. A metastable silicide phase of a stoichiometry Pt_2Si_3 has been obtained by heat treating a Si-rich amorphous Pt-Si alloy layer produced by ion-beam-mixing of thin PtSi (or Pt) films on Si. The Pt_2Si_3 phase is absent in the equilibrium phase diagram of Pt-Si and has not been reported before. X-ray diffraction analysis established the crystal structure of Pt_2Si_3 to be hexagonal with lattice parameters a = 3.841 Å, c = 11.924 Å and with 10 atoms per unit cell. The metastable phase was found to exhibit a superconducting transition onset at about 4.2K and to become completely superconductive at temperature below 3.6K. For the first time, a compound of this structure was observed to be a superconductive material. The transformation behavior of the ion-induced amorphous Pt_2Si_3 alloy has been studied by using resistivity measurements. The amorphous to metastable crystalline transformation occurred at $\sim 400^{\circ}C$ as indicated by an abrupt decrease of resistivity. The metastable phase then gradually decomposed into an equilibrium PtSi and Si mixture at temperatures above $550^{\circ}C$. The kinetics of amorphous to crystalline transformation have been determined by isothermal treatment over the temperature interval $376\text{-}392^{\circ}C$. The results were interpreted in terms of a classical nucleation and growth

mechanism with a t^4 (time) dependence and an apparent activation enthalpy of 4.69 eV (108 kcal/mole). The microstructures of the alloys at various stages of transformation were studied by transmission electron microscopy and diffraction. The results were found to correlate well to the phase transformation behavior observed by resistivity measurements. (Chapters 3 and 4)

To further investigate the production of metastable phases by ion-beam mixing, experiments have been performed in the simple eutectic system of Au-Si. An amorphous alloy with a uniform composition Au-28 at.% Si ($\sim Au_5Si_2$) was formed by bombarding through a thin Au film on Si, a result distinctly different from that obtained in normal thermal treatment. Upon thermal annealing, the amorphous phase transforms into a metastable crystalline phase at $\sim 100^{\circ}C$, which then gradually decomposes into an equilibrium Au and Si mixture at higher temperatures. The present observations were compared with those obtained previously by rapid quenching techniques. The comparison of metastable phase formation in the Pt-Si and Au-Si systems revealed a correlation between the existence of metastable phases and eutectic compositions, as well as the importance of sample temperature during implantation for direct observation of metastable phases. (Chapter 5)

As an extension of compound formation by ion-beam-mixing of a thin layer on a thick substrate, we investigated the mixing of thin deposited layers as a scheme for producing compounds or alloys of desirable compositions. Multiple-layered samples consisting of thin alternate

layers of two elements were prepared by sequential vacuum deposition of the two components onto an inert substrate such as SiO_2 or Al_2O_3. The relative thicknesses of the individual layers were adjusted such that the average film composition was equal to a fixed, predetermined value. Ion bombardment was then performed to homogenize the layers on an atomic scale. Formation of supersaturated Ag-Cu and Au-Co solid solutions over a wide range of composition has been achieved. Extensions of alloy solubility and formation of amorphous phases have been obtained in the almost completely immiscible systems of Ag-Ni and Cu-Ta, respectively. The present scheme may promise to be a new technique for producing metastable phases which are difficult to form or unattainable by conventional rapid quenching techniques. (Chapter 6)

Finally, we consider the possibility of using ion-beam-mixing techniques as an alternative approach to direct high dose implantation for material surface modification. Comparison between ion-beam-mixing and high dose implantation is made to demonstrate the "effectiveness" of ion-beam mixing in incorporating Au or Ag in single crystal Cu substrates. A simple diffusion model for the evolution of ion-beam-mixing of a thin surface layer on a thick substrate was then proposed. The model predicts the influence of implantation conditions and material properties on the redistribution of the thin surface layers. From a practical point of view, the technique of introducing foreign species by ion-beam-mixing process exhibits many attractive advantages over direct implantation because of significantly lower ion doses required and the ability to use simple ion sources. (Chapter 7)

Parts of this thesis either have been or will be published under the following titles:

1. "Ion-Beam-Induced Silicide Formation" B. Y. Tsaur, Z. L. Liau and J. W. Mayer, Appl. Phys. Lett. 34, 168 (1979).
2. "Inert-Gas-Bubble Formation in the Implanted Metal/Si System" B. Y. Tsaur, Z. L. Liau and J. W. Mayer, J. Appl. Phys. 50, 3978 (1979).
3. "Ion-Beam-Induced Formation of the PdSi Silicide" B. Y. Tsaur, S. S. Lau and J. W. Mayer, Appl. Phys. Lett. 35, 225 (1979).
4. "Formation of Si-Enriched Metastable Compounds in the Pt-Si System Using Ion Bombardment and Post Annealing" B. Y. Tsaur, Z. L. Liau and J. W. Mayer, Phys. Lett. A 71, 270 (1979).
5. "Ion-Beam-Induced Intermixing of Surface Layers" B. Y. Tsaur, S. S. Lau, Z. L. Liau and J. W. Mayer, Thin Solid Films 63, 31 (1979).
6. "Depth Dependence of Atomic Mixing by Ion-Beams" B. Y. Tsaur, S. Matteson, G. Chapman, Z. L. Liau and M-A. Nicolet, Appl. Phys. Lett. 35, 825 (1979).
7. "Ion-Beam-Induced Interface Mixing and Thin Film Reactions" B. Y. Tsaur, in Thin Film - Interfaces and Interactions, J. E. E. Baglin and J. M. Poate, eds., (Electrochemical Society, Princeton, New Jersey, 1979).
8. "Metastable Au-Si Alloy Formation Induced by Ion-Beam Interface Mixing" B. Y. Tsaur, J. W. Mayer, M-A. Nicolet and K. N. TU, in Surface Modification of Materials by Ion Implantation, J. K. Hirvonen and C. M. Preece, eds., (Material Research Society, University Park, PA. 1979)
9. "Continuous Series of Metastable Ag-Cu Solid Solutions Formed by Ion-Beam-Mixing" B. Y. Tsaur, S. S. Lau and J. W. Mayer, Appl. Phys. Lett. May 1, 1979 (in press).

10. "Amorphous to Superconducting Crystalline Transformation of the Ion-Induced Metastable Pt_2Si_3 Phase" B. Y. Tsaur, J. W. Mayer and K. N. Tu, (submitted to Phys. Rev. Lett.).

11. "Ion-Beam-Induced Metastable Pt_2Si_3 Phase - I. Formation, Structure and Properties" B. Y. Tsaur, J. W. Mayer and K. N. Tu, (submitted to J. Appl. Phys.).

12. "Ion-Beam-Induced Metastable Pt_2Si_3 Phase - II. Kinetics and Morphology" B. Y. Tsaur, J. W. Mayer and K. N. Tu, (submitted to J. Appl. Phys.).

13. "Influence of Atomic Mixing and Preferential Sputtering on Depth Profiles and Interfaces" Z. L. Liau, B. Y. Tsaur and J. W. Mayer, J. Vac. Sci. Technol. 16, 121 (1979).

14. "High Dose Implantation and Ion-Beam Mixing" J. W. Mayer, S. S. Lau, B. Y. Tsaur, J. M. Poate and J. K. Hirvonen, in Surface Modification of Materials by Ion Implantation (same as 8.)

15. "Ion-Beam-Induced Metastable Phases in the Au-Co System" B. Y. Tsaur, S. S. Lau and J. W. Mayer (to be submitted to Phil. Magz.).

16. "Supersaturated Metastable Ag-Ni Solid Solutions Formed by Ion-Beam-Mixing" B. Y. Tsaur and J. W. Mayer (in preparation).

17. "A Macroscopic Model for the Evolution of Ion-Beam Mixing of a Thin Surface Layer on an Infinitely Thick Substrate" B. Y. Tsaur (in preparation).

TABLE OF CONTENTS

	Page
ACKNOWLEDGMENTS	ii
ABSTRACT	iv
Chapter 1: INTRODUCTION	1
1.1 Background on Ion-Induced Atomic Mixing	1
1.1.1 Theoretical	2
1.1.2 Experimental	5
1.2 Outline of Thesis	7
References	12
Chapter 2: ION-BEAM-INDUCED SILICIDE FORMATION	14
2.1 Introduction	14
2.2 Experimental Procedures	15
2.3 Ion-Beam-Induced Atomic Mixing at Low Ion Doses — Formation of First Silicide Phases	16
2.4 Mechanisms of Ion-Induced Interface Reactions and Factors Affecting the Formation of Silicide Phases	20
2.4.1 Formation Mechanisms	20
2.4.2 Intrinsic Diffusion Properties of the System	25
2.4.3 Implantation Temperature	28
2.4.4 Ion Energy and Mass	33
2.4.5 Ion Dose	35
2.4.6 Radiation Stability	39
2.5 Ion-Beam-Induced Atomic Mixing at High Ion Doses	40

2.5.1 Formation of Second Silicide Phase — the Pd-Si System 41
2.5.2 Formation of Disordered Metal-Si Mixed Layers 46
2.5.2 Formation of Inert-Gas Bibble at Interfaces 50
2.6 Conclusion 55
References 60
Chapter 3: ION-BEAM-INDUCED METASTABLE Pt_2Si_3 PHASE — FORMATION, STRUCTURE AND PRCPERTIES 64
3.1 Introduction 64
3.2 Ion-Beam-Induced Interface Mixing of PtSi on Si and Formation of the Metastable Pt_2Si_3 Phase 65
3.3 Effcts of Bombardment with Different Ion Doses and Ion Species on the Interface Mixing and Compound Formation 68
3.4 X-ray Diffraction Analysis and Crystal Structure 72
3.5 Prcperties of the Ion-Induced Pt_2Si_3 Phase 81
3.5.1 Metastability 81
3.5.2 Superconductivity 82
3.6 Co-deposited Amorphous $Pt_{40}Si_{60}$ Films 84
3.7 Discussions 86
3.8 Conclusion 91
References 93
Chapter 4: ION-BEAM-INDUCED METASTABLE Pt_2Si_3 PHASE — KINETICS AND MORPHOLOGY 95

4.1 Introduction 95

4.2 Sample Preparations and Analytical Techniques 96

4.3 Results 98

4.3.1 Resistivity Measurements 98

4.3.2 Microstructure 104

4.3.3 Kinetics Analysis 110

4.4 Discussions 114

4.5 Conclusion 118

References 120

Chapter 5: METASTABLE Au-Si ALLOYS FORMATION INDUCED BY ION-BEAM-MIXING 121

5.1 Introduction 121

5.2 Formation of Amorphous Au-Si Alloys 122

5.3 Transformation Behavior of the Ion-Induced Au-Si Alloys 127

5.4 Microstructure 134

5.5 Discussions 138

5.5.1 Formation Mechanisms of the Amorphous Au_5Si_2 Phase 138

5.5.2 Comparisons Between Ion-Induced and Liquisol-Quenched Au-Si Alloys 143

5.5.3 Comparisons of Metastable Phase Formation in the Au-Si and Pt-Si Systems 147

5.6 Conclusion 150

References 154

Chapter 6: ION-BEAM-INDUCED MIXING OF THIN ALTERNATE LAYERS (MULTIPLE-LAYERS) 157

6.1 Introduction 157

6.2 Formation of Superconducting V_3Si Phase 160

6.3 Formation of Continuous Series of Metastable Ag-Cu and Au-Co Solid Solutions 165

6.4 Extension of Alloy Solubility in the Ag-Ni System 179

6.5 Formation of Amorphous Cu-Ta Alloys 186

6.6 Summary 188

References 189

Chapter 7: IMPLICATION OF ION-BEAM-MIXING TECHNIQUES IN MATERIAL SURFACE MODIFICATIONS 190

7.1 Introduction 190

7.2 Comparisons of Substitutional Au-Cu (Ag-Cu) Solid Solutions Formed by Direct Implantion and Ion-Beam-Mixing 192

7.3 Ion-Beam-Induced Mixing of a Thin Surface Film on a Thick Substrate 197

7.3.1 A Model 197

7.3.2 An Example 206

7.4 Discussion and Conclusion 212

References 217

Chapter 1

INTRODUCTION

1.1 Background on Ion-Induced Atomic Mixing

Ion implantation has emerged in the past two decades as a powerful method of changing the properties of solids within shallow depths of the bombarded surface [1]. The scope of materials under investigation ranges from bulk crystalline solids, such as semiconductors [2] and metals [3], to thin film targets in that a variety of materials with different compositions and structures can be prepared. The incentive of studying ion implantation in thin films arises mainly from the requirements placed on microelectronic device technology where proper modifications of macroscopic electrical or other physical properties of thin films are necessary to achieve desirable performances [4]. In this respect, numerous investigations have been carried out and the field is still of growing research interest.

Because the thickness of the film is comparable to the ion range, the ions may penetrate through the film and into the substrate. The original interface profile will be altered if the target atoms are displaced significantly from their original positions due to the atomic collisions initiated by the incident ions. The alteration of atomic distributions near the interface regions of a thin-film target by ion bombardment is termed "ion-induced atomic mixing". Redistribution of atoms may result in a drastic change of structural and hence the physical properties of the film and the substrate. Study of ion-

induced atomic mixing in thin film structures is interesting not only because of its importance in the applications of ion-beam material modification, but also because of new insights into atomic collisions and interdiffusion in composite materials.

In this section, some theoretical aspects related to this phenomenon are briefly reviewed and the experimental results previously observed on ion-induced atomic mixing will be enumerated.

1.1.1 Theoretical

A. Recoil Implantation

One of the most frequently observed phenomena associated with ion implantation into a thin film is the incorporation of atoms originally in the film into the substrate as a result of passage of the ions through the interface. This effect, called recoil implantation, was first [5] proposed by Nelson (1969) as a possible technique to introduce impurities into a quite thin layer of the solid surface. Theoretical calculations have been made by Nelson to estimate the recoil yield, which is defined as the number of atoms recoiled from the film into the substrate for one incident ion, of a very thin target under bombardment with heavy projectiles. An analogous theory was developed by Sigmund [6] at about the same time to deal with forward (transmission) sputtering of a thin foil, a situation similar to recoil implantation. Both theories are developed based on collision cascade model [7] and yield, roughly speaking, a similar conclusion: the recoil yield is proportional to the elastic energy loss (or the maximum energy transferred in the elastic collision process) in the passage of swift

ions through the thin film. A typical recoil yield is estimated to be of the order of one to ten in the ion energy range of a few tens to hundreds keV. The profile of recoiled atoms, according to the calculation by Nelson, is shallow and sharply peaked at the film-substrate interface. For example, 10^{16} B atoms/cm^2 recoiled into a Si substrate by implanting 100 keV $5x10^{16}$ Ne^+/cm^2 will have a distribution of ∿100 at.% near the original interface and only 1 at.% in a depth of 300 Å underneath the interface.

B. Cascade Mixing

Recoil implantation is basically a single-collision mechanism and some degree of "anisotropy" in atomic displacement will exist due to the asymmetry of momentum transfers. In other words, the displaced (recoiled) atoms following primary collisions are predicted to be mostly confined to the forward hemisphere. However, many experimental results show that both forward and backward displacements of atoms during collisions are present [8,9], i.e., substrate atoms can also be recoiled "backward" into the film. This phenomenon has been attributed to a multiple-collision mechanism — the so-called "cascade mixing". Cascade mixing is a process in which atoms in the target are transported by successive displacements arising from repeated collisions.

Theoretical [10-13] and numerical [14] (computer simulation) treatments have been attempted by a number of investigators to relate interface mixing to the parameters of ion and target materials. The most simple model is to consider atomic migration due to cascade

mixing as a random-walk process under the assumption of isotropic momentum transfer, i.e., motions of atoms in the collision cascades are equally possible in all directions. The transport of atoms is then characterized by an effective diffusion coefficient which is proportional to the ion energy deposited into the atomic process (i.e., nuclear energy loss) and the incident ion flux. Based on this concept, an original delta function (step function) of atomic distribution will be smeared into a Gaussian distribution (error function). The broadening will increase with ion energy (in the range below a few hundred keV), masses of ion and target materials and total ion fluence. Numerical estimates [15] of this process for 300 keV 5×10^{15} Xe^{+}/cm^{2} into Si yield a "diffusion length" of the order of 100 Å.

C. Radiation-Enhanced Diffusion

Radiation-enhanced diffusion is a process where atomic diffusion (or migration) is enhanced due to the presence of bombardment-induced defects. This mechanism is differentiated from the cascade mixing by its dependence on thermally-activated defect migration, i.e., the process is sensitive to the implantation temperature because of the defect-assisted diffusion mechanism. A theoretical steady-state kinetic treatment [16] was first developed by Dienes and Damask (1958) for enhanced self-diffusion (by vacancy or interstitial mechanism) in a crystalline solid. Their formulisms have been used to account for the enhanced diffusion of dilute impurities ($\lesssim$ 1 at.%) in single-crystal Al [17] or Si [18] substrates induced by light ions (such as H^{+}, He^{+} and Ne^{+}) irradiation. However, no theoretical considerations

have been given to deal with enhanced diffusion between a film and a substrate. The treatment for a dilute impurity in a crystalline solid described in the above may not be applicable to the thin film case because of the high concentration of "impurities" in the intermixed region.

1.1.2 Experimental

The early experimental observations on ion-induced atomic mixing are summarized as follows:

It was found by Stroud *et al* [19] that for thin Al films on glass substrates bombarded with energetic Ar ions through the interface, the substrate was doped with Al and the Al film contained oxygen as well. Significant improvement of adhesion [20] between the Al and the glass substrate was observed for Ar doses greater than $10^{15}cm^{-2}$. This increase in bonding was attributed to the formation of an intermediate structure at the Al-glass interface due to ion-induced atomic mixing effect.

Nishi *et al* [21] have studied the effects of Ar ion bombardment on the interface between a metal (Mo or Cr) and a Si (or SiO_2) substrate. By backscattering measurements, they observed the presence of Mo (Cr) atoms in the substrates after chemical removal of the Mo (Cr) films. About one to five Mo (Cr) atoms were found incorporated in the substrates for one incident ion. Moreover, the metal content in the Si substrate is about two or three times higher than that in the SiO_2 substrate under identical implantation conditions. Although recoil implantation was proposed as the dominant mechanism for mixing, the enhanced-mixing effect observed in the metal/Si systems suggests a

possible influence of chemical interactions (between metal and Si) on interface mixing. However, no structural or chemical information of those mixed layers were reported in their paper.

In contrast to the result observed in the Mo (Cr)-Si system, Lee et al [22] observed a "pronounced intermixing" between Pd films and crystal Si substrates under P ion bombardment. The number of intermixed Pd atoms was found to be substantially greater than what is expected from the atomic recoil process. A somewhat more detailed study was carried out subsequently by van der Weg et al [23] using 100-400 keV Ar ions and various thickness of Pd films (ranging from 300 to 1100 Å) on Si. Backscattering and x-ray diffraction measurements indicated the formation of rather uniformly mixed layers containing the Pd_2Si silicide phase if the ions were energetic enough to penetrate through the Pd-Si interface. The ion-induced Pd_2Si phase had the same structure as the phase obtained by normal thermal treatment of Pd films on Si at temperatures $\simeq 200^{o}C$. This is the first observation of interfacial compound formation induced by ion bombardment. A similar experiment was carried out by Poate et al [24] to examine the ion-induced interface interactions in the Pt-Si system. By implanting 120 keV 1×10^{16} Ar ions/cm^2 through a 150Å Pt film deposited on a Si <100> substrate, they observed formation of a Pt-Si mixture with a composition close to PtSi. However, the silicide phase was not identified in the Pt-Si mixed layer.

The results of ion-induced atomic mixing between a metal film and a Si substrate described in the above had not been put in consistent

framework due to the complex nature of the mixing process. Not only does the amount of mixing vary drastically from one system to another, but also the intermixed layers produced for different metal films (on Si) show significant differences in structure and atomic distribution. A quantitative comparison between the experimental results and the theoretical predictions described in the previous section was not made because the atomic mechanisms involved in the mixing process were not fully appreciated. In an attempt to elucidate the mechanisms of mixing, we have carried out a systematic study of mixing in various metal/Si systems. Considerable attention has been paid on the structure and atomic distribution of interfacial mixed layers. The influence of implantation conditions such as ion energy, mass, fluence and implantation temperature was also carefully examined. Aside from the study of fundamental mechanisms of mixing, we have investigated the possibility of utilizing the ion-induced atomic mixing process to produce thin film compounds or alloys. Equilibrium phases as well as nonequilibrium phases (metastable phases) have been achieved under various conditions. Much of our effort has been concentrated on the characterizations of those ion-induced metastable phases. We also place emphasis on the mechanisms of metastable phase formation as well as the potential of ion-beam-mixing techniques in the area of material surface modification.

1.2 Outline of Thesis

In Chapter 2, ion-induced atomic mixing and compound formation as a result of energetic ion bombardment through a thin transition-metal film deposited on a Si substrate is described. Examples are

first given to demonstrate the formation of well-defined silicide phases under low dose ion bombardment and the results are compared with those obtained previously by normal thermal treatment. A simple macroscopic model is then proposed to account for the ion-induced interface reactions. The atomic mechanisms involved in the interface mixing process as to the formation of silicide phases are discussed based on the results observed in various systems. The factors affecting those mechanisms such as implantation conditions and intrinsic properties of target materials will be described. Ion-beam mixing at high ion doses can lead to the formation of more Si-rich silicide phases or disordered metal-Si mixed layers which are difficult to form or in some cases inaccessible by normal thermal treatment. Examples with Pd-Si and Pt-Si systems are given to demonstrate the effects. In the last section, "interface" bubble formation as a result of condensation of implanted gas ions is described. This provides another demonstration of the long-range atomic mobility in the ion-beam-mixing process.

In Chapter 3 we report the production of a new metastable phase, Pt_2Si_3, by using ion-beam-mixing techniques. To form the phase, a thin PtSi film on a Si substrate is first converted into a Si-rich amorphous Pt-Si mixed layer by implantation with energetic ions through the PtSi-Si interface. The amorphous alloy then transforms into the metastable crystalline phase upon post-annealing between 350 and 500°C as indicated by backscattering and x-ray diffraction measurements. The crystal structure of the phase, determined from the angular positions of the crystalline reflections, is presented. We have also determined the

atomic positions within the unit cell based on the relative intensities of the diffraction lines and the forbidden reflections. The properties of the Pt_2Si_3 phase such as metastability and especially, the superconducting transition behavior are described. Experiments using co-deposited amorphous Pt_2Si_3 films have been performed in an attempt to produce the metastable Pt_2Si_3 phase without using ion-beams. The results are compared with those obtained from ion-bombarded films. The mechanisms of metastable phase formation will be discussed.

In Chapter 4, the kinetics of phase transformation, morphology and microstructural changes of the ion-induced Pt_2Si_3 alloyed layers studied by resisitivity measurements and transmission electron microscopy will be presented. Isochronal annealing between R.T. and 800^oC was first performed to study the transformation behavior of the ion-induced amorphous Pt_2Si_3 alloys. The kinetics of amorphous to metastable crystalline transformation was then determined by isothermal treatment over a narrow temperature interval. The results are analyzed in terms of a classical nucleation and growth mechanism; the apparent activation energy and the mode of transformation are determined. A qualitative discussion is given for the correlation between the kinetics of phase transformation and the microstructure of the alloyed layers.

In Chapter 5 we investigate the ion-induced atomic mixing process in the simple eutectic Au-Si system. By bombarding through a thin Au film deposited on a Si substrate, an amorphous Au-Si layer with a uniform composition Au-28 at.% Si ($\sim Au_5Si_2$) is formed at the interface.

The thickness of this layer increases with ion dose until the consumption of the Au layer. These results are distinctly different from those obtained in normal thermal treatment where the interface reaction is nonuniform and no amorphous phases are observed. Upon thermal annealing, the amorphous phase transforms into a metastable crystalline phase at $100^{o}C$, which then gradually decomposes into an equilibrium Au and Si mixture at higher temperatures. The mechanisms of interface mixing as to the formation of amorphous phase are discussed. The present observations are compared with those obtained previously by rapid quenching techniques. A comparison of results observed in the Au-Si and Pt-Si system is given with emphasis on the process of metastable phase formation.

Chapter 6 is concerned with a new scheme of producing compounds or alloys by using ion-beam-mixing techniques. Multiple-layered samples consisting of thin alternate layers of two elements are prepared by sequential deposition of the two components onto an inert substrate such as SiO_2 or Al_2O_3. Ion bombardment is then performed to homogenize those layers on an atomic scale. Example with V-Si is given to demonstrate the formation of the A-15 V_3Si phase by post-annealing the ion-mixed V-Si layers with a composition V_3Si. Application of the multiple-layered structure in the Ag-Cu and Au-Co systems can lead to the formation of supersaturated solid solutions over a wide range of composition. Extension of alloy solubility and formation of amorphous phases will be shown in the almost completely immiscible systems of Ag-Ni and Cu-Ta, respectively.

In Chapter 7 we consider the possibility of using ion-beam mixing techniques as an alternative approach to direct high dose implantation for material surface modification. Comparison between ion-beam mixing and high dose implantation is first given to demonstrate the "effectiveness" of ion-beam mixing in producing substitutional Au-Cu or Ag-Cu alloyed layers on single crystal Cu substrates. A simple mathematical model for the evolution of ion-beam-mixing of a thin surface layer on a thick substrate is then presented and examples given. Finally, the advantages and limitations of using ion-beam mixing techniques in the area of material surface modification will be discussed.

REFERENCES

1. See, for example, G. Dearnaly, J. H. Freeman, R. S. Nelson and J. Stephen, Ion Implantation , (North-Holland Publishing Company, Amsterdam, 1973).

   G. Carter, J. S. Colligon and W. A. Grant, eds., Applications of Ion Beams to Materials (Institute of Physics Conference Series number 28, 1975).

2. J. W. Mayer, L. Eriksson and J. A. Davies, Ion Implantation in Semiconductors (Academic Press, New York, 1970).
3. S. T. Picraux, E. P. EerNisse and F. L. Vook, Eds., Applications of Ion Beams to Metals (Plenum Press, New York, 1974).
4. P. T. Stroud, "Ion Bombardment and Implantation and Their Application to Thin Films". Thin Solid Film 11, 1 (1970).
5. R. S. Nelson, Rad. Effects, 2, 47 (1969).
6. P. Sigmund, Phys. Rev. 184, 383 (1969).
7. C. Erginsoy, A. Englert and G. Vineyard, Phys. Rev. 133, 595 (1964).
8. J. A. McHugh, Rad. Effects 21, 209 (1974).
9. B. Y. Tsaur, S. Matteson, G. Chapman, Z. L. Liau and M-A. Nicolet, Appl. Phys. Lett. 35, 825 (1979).
10. P. Sigmund, Appl. Phys. Lett. 14, 114 (1969).
11. P. K. Haff and Z. E. Switkowski, J. Appl. Phys. 48, 3383 (1977).
12. W. O. Hofer and V. Littmark, Phys. Lett. 71A, 457 (1979).
13. H. H. Andersen, Appl. Phys. 18, 131 (1979).
14. T. Ishitani and R. Shimizu, Appl. Phys. 6, 241 (1975).

15. S. Matteson, G. Mezey and M-A. Nicolet, Proceedings of Thin Film Interface and Interactions, ECS Meeting Oct. 1979, Los Angeles.

16. G. T. Dienes and A. C. Damask, J. Appl. Phys. 29, 1717 (1958).

17. S. M. Myers and S. T. Picraux, J. Appl. Phys. 46, 4774 (1925).

18. B. Masters and E. Gorey, J. Appl. Phys. 49, 2717 (1978).

19. P. T. Stroud, L. E. Collins, J. G. Perkins and K. G. Stephens, European Conference on Ion Implantation (Peter Peregrinus Ltd., England, 1970).

20. L. E. Collins, J. G. Perkins and P. T. Stroud, Thin Solid Films 4, 41 (1969).

21. H. Nishi, T. Sakurai and T. Furuya, Ion Implantation in Semiconductors ed. S. Namba (Plenum, New York 1975) p. 347.

22. D. H. Lee, R. R. Hart, D. A. Kiewit and O. J. Marsh, Phys. Stat. Sol.(a) 15, 645 (1973).

23. Ref. 3, page 209.

24. J. M. Poate and T. C. Tisone, Appl. Phys. Lett. 24, 391 (1974).

Chapter 2

ION-BEAM-INDUCED SILICIDE FORMATION

2.1 Introduction

In this chapter, we report silicide formation induced by ion-bombardment through a thin transition-metal film deposited on a Si substrate. During the past ten years, extensive studies of contact reactions between thin transition-metal films and crystal Si substrates have been pursued in detail [1]. The incentive arises from the requirement placed on integrated circuit technology, where metal-silicides are widely used for Ohmic contact and Schottky barriers to achieve reliable and stable characteristics [2,3]. It was generally found that silicide phases can be formed at temperatures well below the eutectic or peritectic temperatures. For example, Pd_2Si is formed at temperatures of 200^oC [1], while the lowest eutectic is 760^oC. This low temperature reaction is suggestive of high reactivity (or high atomic mobility) in the transition-metal-Si system. Consequently, our initial ion-beam mixing experiments have been directed primarily toward silicide forming systems in view of the high reactivity of the metal-Si interface. We found that ion bombardment through a metal-Si interface can initiate the formation of a silicide phase that is identical to the one obtained by normal thermal treatment. Examples will first be presented to demonstrate this phenomenon. The mechanisms of interface reactions and factors affecting those mechanisms will be discussed subsequently based on comparison of results observed in different systems under various implantation conditions.

2.1 Experimental Procedures

Thin metal films, a few hundred Å thick, were prepared by electron-gun evaporation of high purity transition-metals (Pt, Ni, Cr, V, etc.) onto Si single crystal substrates of <100> and <111> orientations. The Si wafers were organically cleaned with trichloroethylene, acetone, and methanol, etched in dilute HF ($H_2O:HF \approx 10:1$), and rinsed in deionized water immediately prior to loading in an oil-free vacuum system. The distance between the Si wafer and the evaporated charge was ∿30 cm. During evaporation the background pressure was maintained at or below $5x10^{-7}$ Torr with an average deposition rate of 10 Å/sec. The depositions are performed at room temperature; no intentional heating or cooling of the Si substrates was introduced.

The samples were cut into several pieces, each 5x10 mm, for ion-beam experiments. Implantation was carried out in a 400 keV ion-implantor at ion energies between 100-300 keV. Spatially uniform Ar^+, Kr^+, Xe^+ and Si^+ beams were obtained by scanning the beam across a 1x2 tantalum aperture, which was placed ∿20 cm in front of the sample. The pressure in the target chamber was $\sim 8x10^{-8}$ Torr before implantation and increased to $\sim 5x10^{-7}$ Torr during implantation. Typical beam current densities were about 1-2 $\mu A/cm^2$ and ion doses ranging from $2x10^{14}$ to $2x10^{16} cm^{-2}$ were used.

The sample temperature during implantation was monitored by an Alumel-Chromel thermocouple attached to the sample holder. The holder could be cooled down to 80K by LN_2 cooling and heated to excess of 300^oC by circulating hot air. Adequate thermal contact of samples to

the sample holder was assured by a thin layer of heat sinking compound. The temperature change during implantation was found to be less than $20^{o}C$. The sample normal was usually misaligned against the beam axis by 7° in order to avoid channeling effects during implantation.

In-depth compositional profiling measurements were performed using Rutherford backscattering technique (RBS) with 2.0 Mev ^{4}He ions. The backscattered He particles were detected at an angle of 170° with respect to the incident beam by a silicon surface-barrier detector. The depth resolution was ∿200Å for normal incidence. This could be improved by a factor of 2,3, or 4 by tilting the sample at an angle of 60°, 70.5^{o} or 75.5^{o}, respectively, against the incident beam. Glancing angle x-ray diffraction analysis with $CuK\alpha$ radiation in a Read camera was employed to examine the phase structure of the surface layers. Detailed descriptions of these two techniques in thin film analysis have been recently reviewed (4,5). In some cases, transmission electron microscopic analysis was performed to study the microstructure of the ion-irradiated layers.

2.3 Ion-Beam-Induced Atomic Mixing at Low Ion Doses - Formation of First Silicide Phases

Figure 2.1 shows the ion backscattering spectra of two samples, each with a 500 Å Ni (or V) film on top of a Si substrate, bombarded with 300 keV Xe^{+} at room temperature to a dose of $6\times10^{15}cm^{-2}$. The projected ranges (R_p) of Xe in Ni and V are 450 Å and 550 Å, respectively, so that the implanted Xe distributions have a peak

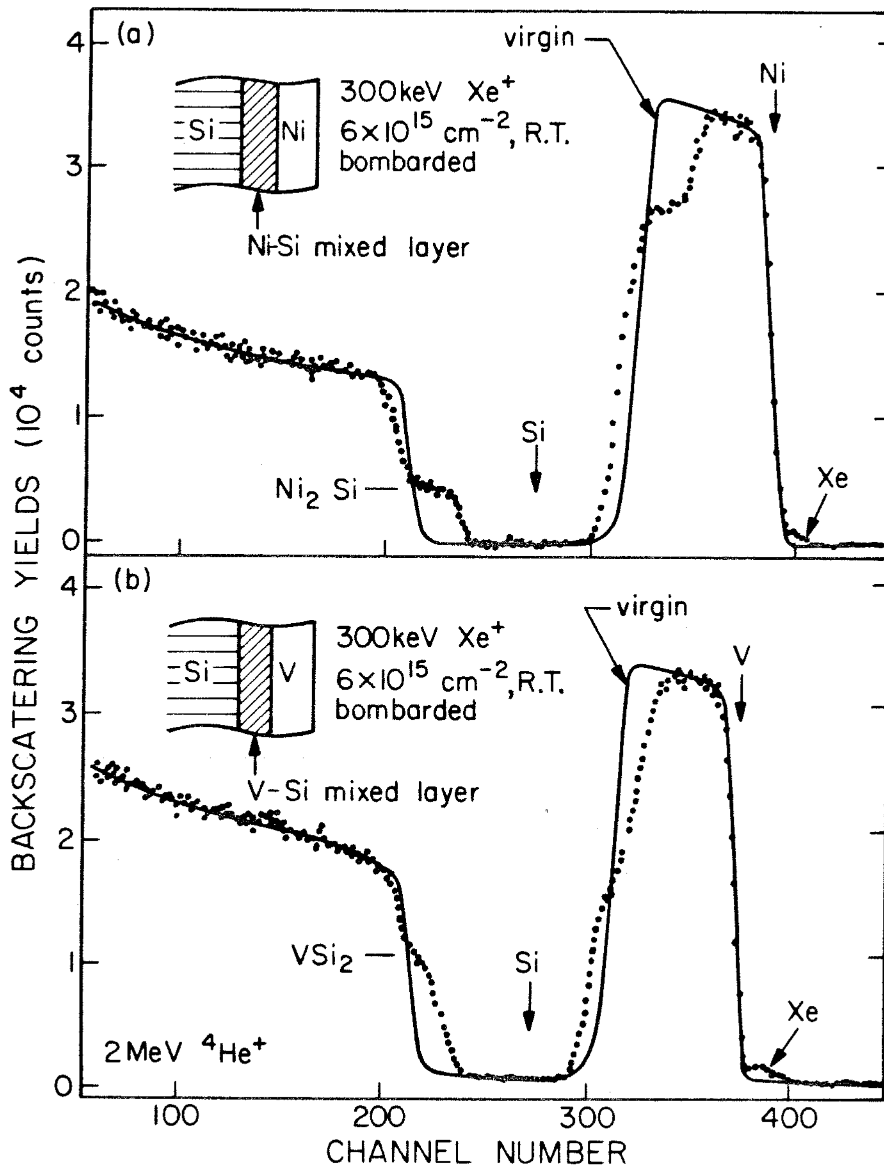

Fig. 2.1 Ion backscattering spectra which show the formation of the Ni_2Si and VSi_2 phases by implanting 300 keV $6x10^{15}$ Xe^+/cm^2 through a thin layer of Ni or V on top of a Si substrate. The ion-induced silicide phases are the same as those formed by thermal annealing of Ni (or V) films on Si.

roughly corresponding to the metal-Si interface. As can be seen in Fig. 2.1, well-defined intermixed layers with compositions close to Ni_2Si and VSi_2, respectively, are formed near the interfaces. These results are quite similar to those observed in normal thermal treatment where formation of the Ni_2Si and VSi_2 phases are obtained at temperatures of $\sim 200^oC$ and 600^oC, respectively [1]. The presence of the Ni_2Si phase was confirmed by x-ray diffraction analysis, where polycrystalline reflections corresponding to both Ni_2Si and Ni were observed. However, the VSi_2 phase was not clearly resolved by our detection techniques because of weak crystalline reflections in the x-ray diffraction pattern.

A summary of our observations on the first phase formed with ion-beam mixing in the transition-metal/Si systems is given in Table II-1. For comparison, the compounds obtained by normal thermal treatment are also included [1]. The intermixed layer produced usually exhibited a composition corresponding to that of a particular compound. In noble-metal/Si systems, compounds of well-defined layered structure (such as Ni_2Si shown in Fig. 2.1(a)) were observed and the phases have been identified by x-ray diffraction measurements. For most of the refractory-metal/Si systems, however, the compound layers were less uniform (such as VSi_2 shown in Fig. 2.1(b)) and phase identification was incomplete mainly because the crystalline reflections were too weak to be unambiguously determined. The differences of results observed between noble-metal/Si and refractory-metal/Si systems and the factors affecting the formation and crystalline structure of the ion-induced silicide phases will be discussed

TABLE II-1 Comparison of the First Phase Formed by Thermal Annealing and by Ion-Beam Mixing[(a)] in the Transition-Metal/Si Systems

	Metal/Si	Compounds Observed		Phase Formed by Termal Anneal	Ref.
		Composition[(b)]	Phase[(c)]		
Noble-Metal	Ni/Si	Ni_2Si	Ni_2Si	Ni_2Si	6
	Pd/Si	Pd_2Si	Pd_2Si	Pd_2Si	7,8,9
	Pt/Si	Pt_2Si	Pt_2Si	Pt_2Si	6
	Co/Si	~ Co_2Si	Co_2Si*	Co_2Si	10
	Fe/Si	~ FeSi	-	FeSi	10
Refractory-Metal	Ti/Si	~ $TiSi_2$	-	$TiSi_2$	10
	V/Si	~ VSi_2	-	VSi_2	10
	Cr/Si	$CrSi_2$	$CrSi_2$**	$CrSi_2$	10,11
	Nb/Si	$NbSi_2$	$NbSi_2$**	$NbSi_2$	10,12,13
	Hf/Si	HfSi	-	HfSi	6

(a) Implantations performed with 100-300 keV inert-gas ions (Ar^+, Kr^+ or Xe^+) at doses of 10^{14} - 10^{16} ions/cm^2.

(b) Composition determined by backscattering measurements.

(c) Phase structure determined by glancing angle x-ray diffraction measurements (Read camera).

* Weak crystalline reflections.

** Phases observed for samples implanted at elevated temperatures ($300^{o}C$).

\- Phases not clearly identified because of very weak crystalline reflections.

in the following section. As can be seen in Table II-1, the first silicide phase formed by ion-beam mixing is in general identical to that obtained by normal thermal treatment.

2.4 Mechanisms of Ion-Induced Interface Reactions and Factors Affecting the Formation of Silicide Phases

In this section, a simple model is first proposed to account for the interface reactions induced by ion bombardment. The atomic mechanisms involved in the interface mixing process related to the formation of silicide phases are then discussed. Factors such as implantation conditions and intrinsic properties of target materials affecting those mechanisms will be described based on the experimental results observed in various metal-Si systems.

2.4.1 Formation Mechanisms

There are two obvious mechanisms for silicide formation; namely, (1) sample heating during ion bombardment [14] or (2) recoil of metal atoms into the Si substrate [15] as described in Chapter 1. The experimental results, however, do not support either mechanism. The beam-heating effect can be effectively ruled out by the following reasons: (1) An interface reaction is observed only when the ions are energetic enough to reach beyond the interface. No reaction can be seen if the incident ions stop within the metal film [6,7]. (2) Implantations with a very low ion flux (or beam current) have been

performed to minimize the beam-heating effect. Almost the same amount of intermixing as that obtained with a high ion flux was observed. (3) The sample area adjacent to the implanted region, but not exposed to the beam, does not show any interface reaction. On the other hand, it is also unlikely that intermixing results from knock-on implantation. For a typical ion dose ($\sim 10^{15} cm^{-2}$) used, a number of metal atoms in excess of $10^{17} cm^{-2}$ appeared intermixed with Si atoms. This number is substantially greater than what can be accounted for by recoil implantation [(15)].

The atomic processes involved in ion-induced interface mixing are complicated and have been the subject of many recent investigations [(16-20)]. Theoretical considerations have been made to relate the interfacial diffusion (mixing) to the nuclear stopping power of the incident ions [(21,22)]. In an attempt to understand the kinetics of the interface reaction, we conjecture that the process might be composed of many "localized" elemental processes each initiated by one incident ion [(23)]. In other words, each incident ion triggers a local region of atomic mixing which results in forming an "island" of intermixed material near the interface as shown in Fig. 2.2a. This assumption is consistent with the experimental observation that atomic mixing extends only over a depth comparable to the ion range.

Let us first consider the mixing due to one incident ion. This is demonstrated in Fig. 2.3. Initially, the sharp interface is disturbed as a result of the dynamic collision process (cascade mixing) initiated by the passage of the primary ion. Further interdiffusion of atomic

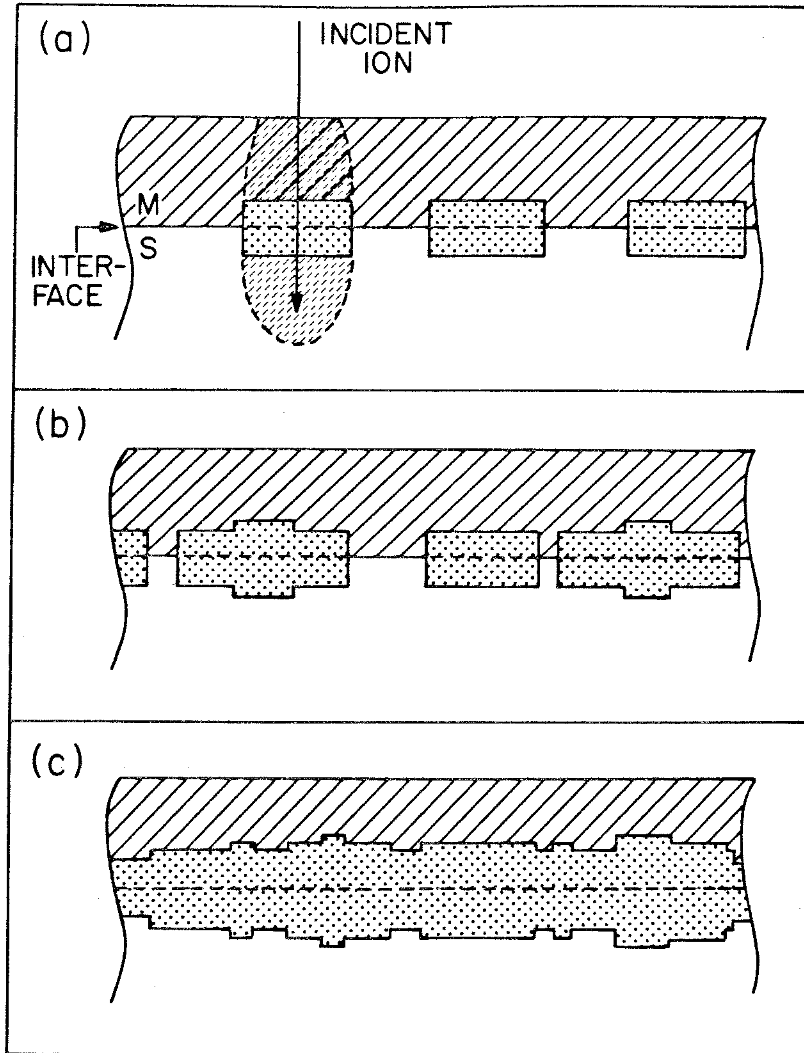

Fig. 2.2 Ion-induced interface reaction can be considered as being composed of many "localized" elemental processes each initiated by one incident ion(a). The elemental processes overlap (b) and a layer structure is obtained at high ion doses (c).

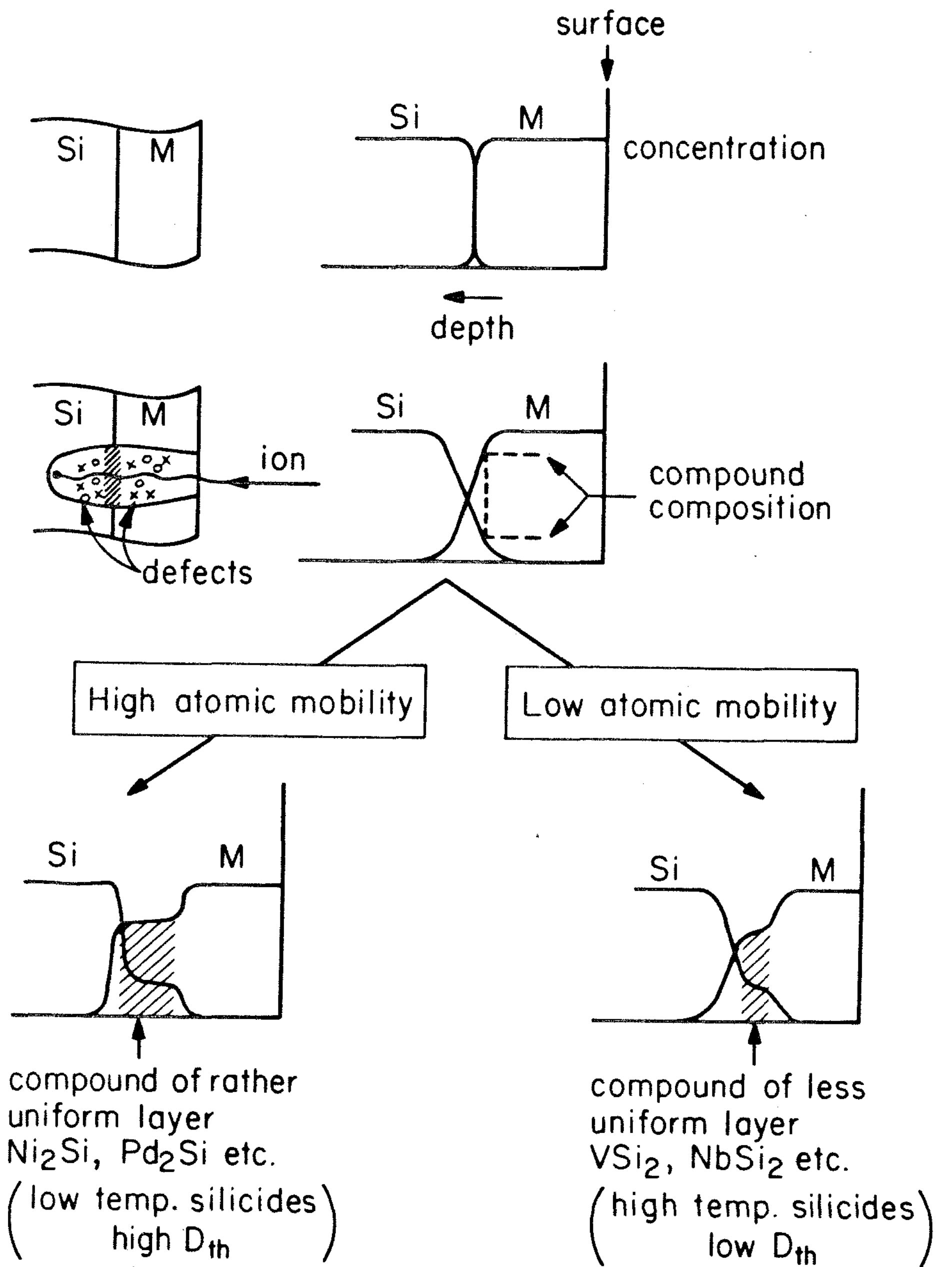

Fig. 2.3 Schematic picture which demonstrates the ion-induced formation of interfacial mixed region where silicide phase can be initiated. The thickness and uniformity of the silicide layer depend strongly on the intrinsic diffusion property of the system.

species within the cascade volume can be promoted due to the presence of bombardment-induced defects (such as vacancies and interstitials). If the composition at certain depth in the intermixed region is close to the stoichiometry of a particular compound, compound formation will be initiated because it is energetically favorable. In other words, the intermixed region, which originally contains randomly distributed atoms due to the cascade mixing process, is in a nonequilibrium high energy state. It will tend to relax to a low energy configuration closer to thermal equilibrium via phase formation. This can be achieved not only because it is thermodynamically favorable but also because the presence of bombardment-induced defects can enhance atomic interdiffusion. It is found that the dominant phase formed in the intermixed region is the same as that obtained by the normal thermal process. As more and more ions come in, more such intermixed regions are created. The regions are likely to cover the whole interface and an incident ion may therefore hit on an intermixed region which is already present. In the overlapped regions, we assume the reaction can be promoted further as shown in Fig. 2.2b. At high ion doses, a layer structure is obtained (Fig. 2.2c), which is similar to the growth of planar silicide phases near the metal-Si interface by thermal treatment [1].

The thickness and uniformity of the intermixed layer are strongly dependent on the elemental process initiated by one incident ion and, hence, of the intrinsic diffusion property of the system. If the system has a high intrinsic atomic mobility (diffusivity), a uniform reacted region will be formed (Fig. 2.3). This seems to be

the case for the noble-metal/Si systems where silicide phases can be formed at rather low temperatures ($\sim 250^{o}C$), which indicates a high atomic mobility. For refractory-metal/Si system, however, the reacted region will be thinner and less uniform because formation of the phases usually requires higher temperatures ($>600^{o}C$) and the atomic mobility is relatively lower. These effects can be seen clearly in the examples with Ni/Si and V/Si shown in Fig. 2.1.

2.4.2 Intrinsic Diffusion Properties of the System

To demonstrate further the intrinsic diffusion properties of target materials on interface mixing, examples with Ni/Si, Co/Si and Fe/Si are given in Fig. 2.4. The Ni, Co and Fe are chosen because they have almost identical mass (less than 5% difference). If samples with the same thickness were bombarded under identical implantation conditions, the atomic collision (cascade mixing) process will be quite similar. However, the results shown in Fig. 2.4 indicate significant differences in the amount of interface mixing. The mixing in the Ni/Si is greater than that in the Co/Si, and the mixing in the Co/Si is greater than that in the Fe/Si.

A plot of the numbers of Si atoms/cm^2 (measured from the shaded area in the RBS spectra of Fig. 2.4) contained in the mixed layers versus the square root of ion doses is given in Fig. 2.5a. For comparison, the thermal diffusion coefficient for the formation of the Ni_2Si, Co_2Si and FeSi phases (the first silicide phases formed in those

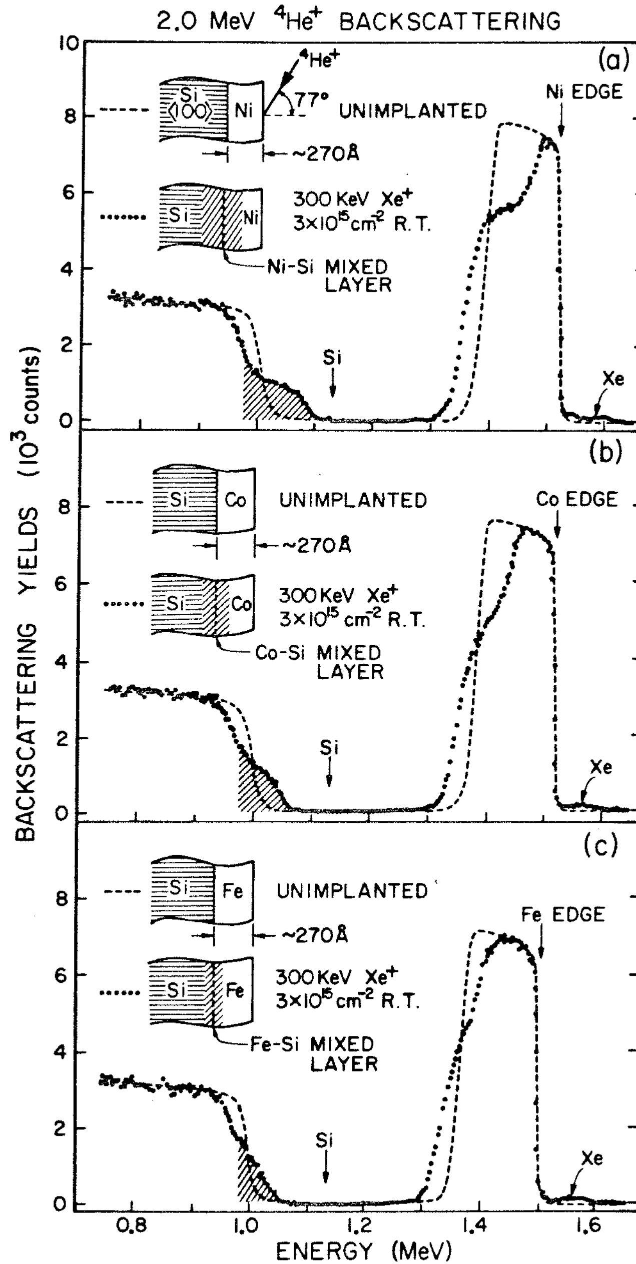

Fig. 2.4 Ion backscattering spectra of samples with Ni, Co and Fe films on Si substrates, bombarded with 300 keV Xe ions at R.T. to a dose of $3x10^{15}$ cm^{-2}. Significant differences in the amount of intermixing can be seen although the atomic collision processes are quite similar in those systems.

systems [24]) are shown in Fig. 2.5b. A noticeable correlation can be seen between the results obtained by ion-beam mixing and those by thermal annealing, i.e., the mixing process is more pronounced for systems which tend to react (interdiffuse) thermally at lower temperature. Moreover, the square-root dependence of reaction on ion dose (Fig. 2.5a) is

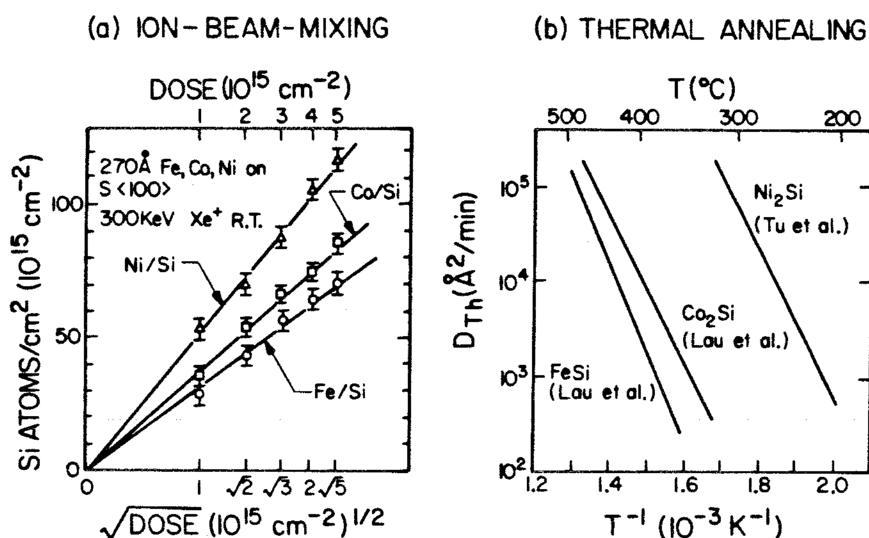

Fig. 2.5 (a) Number of Si atoms/cm^2 in the intermixed layers as a function of the square root of ion dose.
(b) Thermal diffusion coefficients for the formation of the Ni_2Si, Co_2Si and FeSi phases. The ion-induced interface mixing displays a strong metallurgical dependence in the sense that the mixing is more pronounced for systems which tend to react (interdiffuse) thermally at lower temperatures.

also somewhat similar to the kinetics of the square root of time dependence [24] in thermal treatment for all three cases. Notice that the total ion <u>dose</u> is proportional to the total implantation <u>time</u> if the

dose rate (or ion flux) is maintained constant (and it was in our experiments). A detailed description of the relation between silicide thickness and ion dose will be presented in Section 2.4.5.

Comparisons have also been made in other systems such as Nb/Si and Pd/Si (m_{Nb} = 93, m_{Pd} = 106), and Hf/Si and Pt/Si (m_{Hf} = 180, m_{Pt} = 195). The results showed that the reactions were greater for the Pd/Si and Pt/Si systems, which, again, agree with those observed in normal thermal treatment. The dependence of interface mixing on intrinsic diffusion properties of the materials is consistent with the picture that atomic interdiffusion (due to the presence of bombardment induced defects) is required to form the silicide phase.

2.4.3 Implantation Temperature

Since formation of silicide phases require interdiffusion of atomic species during ion bombardment, one would expect that the substrate temperature during ion bombardment will have an influence on the atomic mobility (or diffusivity) and hence the amount of interface mixing. Indeed, a temperature dependence of interface mixing has been observed in all the metal/Si systems we have studied. As an example, Fig. 2.6 shows the backscattering spectra of 300Å Cr/Si samples, bombarded with 300 keV Xe ions at various substrate temperatures (from LN_2 temperature to 270°C) but under otherwise identical implantation conditions. The intermixed layers produced at low temperatures (LN_2 and R.T.) are nonuniform but the layers become progressively more uniform (with a composition close to Cr_2Si) as the implantation temperature

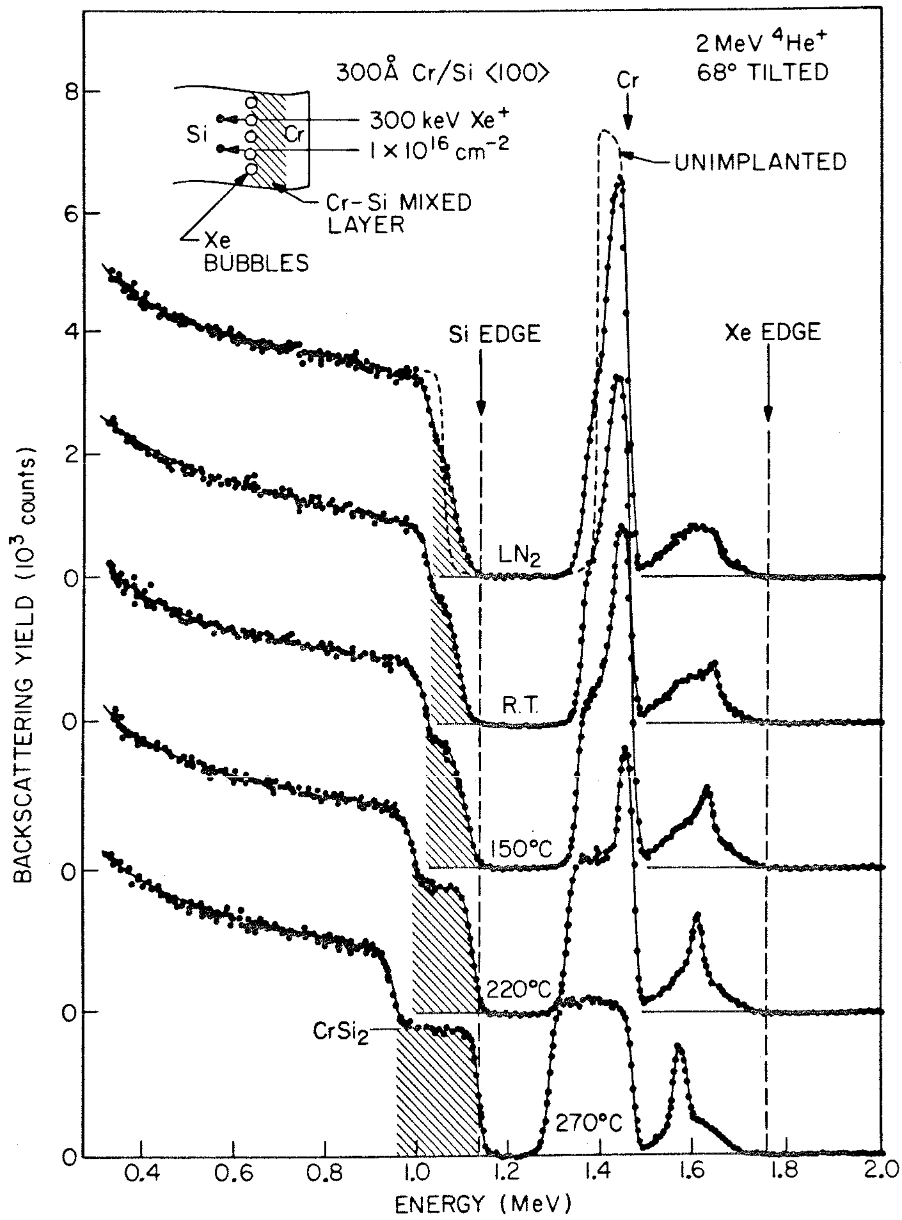

Fig. 2.6 Ion backscattering spectra for 300 Å Cr/Si samples bombarded with 300 keV Xe^{+} at various substrate temperatures to a constant dose of $1x10^{16}$ cm^{-2}. The amount of intermixing increases with increasing temperature.

increases. To ensure the reactions observed at high temperatures are not caused by thermal effects, a controlled sample, which was mounted on the same heating stage but shielded from the ion-beam, was used to monitor the reactions induced by the thermal heating only. No visible reaction was observed as indicated by backscattering measurements. Notice that a sharp peak in the Xe signals is developed due to "interfacial bubble" formation (inset of Fig. 2.6) which will be described in detail in Section 3.5.3. With increasing temperature, the position of the peak, following the movement of Si-silicide ($CrSi_2$) interface, shifts progressively toward the lower energy part of the spectra.

Fig. 2.7 shows a plot of the amount of Si atoms intermixed with the Cr film (shaded area in Fig. 2.6) as a function of reciprocal temperature. As can be seen in the figure, the mixing is relatively insensitive to temperature at temperatures below R.T., but the reaction increases drastically above R.T. This behavior can be interpreted as follows: At low temperatures, the mixing is dominated by a dynamic collision process (cascade mixing) which depends mainly on the ion energy and the masses of ion and target atoms. This process is relatively insensitive to temperature. Nonuniform mixed layers are usually observed for mixing in this temperature regime because phase formation is unlikely due to the lack of atomic mobility. In some cases, completely random (amorphous) structures are found in those nonuniform mixed layers. On the contrary, defect-enhanced-diffusion becomes dominant in the high temperature regime because the displaced atoms would have enough mobility to migrate under the presence of bombardment-induced defects.

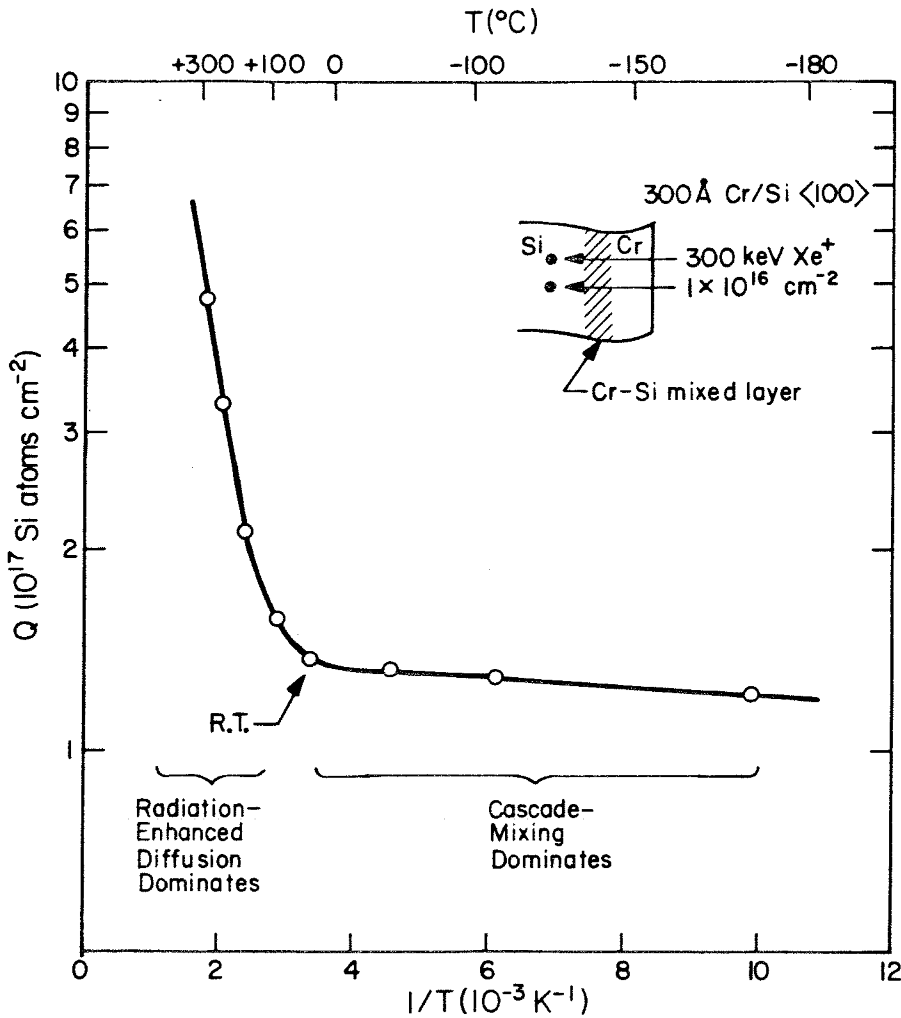

Fig. 2.7 The amount of Si atoms contained in the Cr-Si mixed layers, Q, versus reciprocal implantation temperature. Two distinct regimes are observed: At low temperature the mixing is dominated by a dynamic collision process (cascade mixing) which is relatively insensitive to temperature, whereas at high temperature radiation-enhanced diffusion mechanism becomes dominant amd the mixing increases drastically with temperature.

Uniform mixed layers with well-defined phase structure are usually obtained. Radiation-enhanced diffusion is, in general, a thermally activated process. Its temperature dependence is closely related to the intrinsic properties of materials such as vacancy (or interstitial) migration rate and densities of defects (dislocations and grain boundaries) contained in the materials [25]. Consequently, the "onset temperature" of the transition at which drastic increase of mixing occurs and the slope of the curve in the higher temperature part will vary from system to system. However, the general shape of the temperature dependence curve is found to be roughly the same for the systems (Cr/Si, Ni/Si, V/Si and Pt/Si) we have studied.

Radiation-enhanced diffusion phenomenon has, in the past, been extensively studied [26,27] for light projectiles (proton or He) in bulk single crystals (Si, Ge or Al) containing dilute impurities ($\sim$1 at.%). Theoretical considerations have also been given to correlate enhanced-diffusion coefficients to material parameters under various implantation conditions [28,29]. However, the situation becomes much more complex for heavily doped materials and the experimental results are not readily interpretable [30]. In the present case of ion-beam mixing, the situation is further complicated by the formation of silicide phases. We believe that enhanced-diffusion between a thin surface layer and a substrate induced by ion bombardment is still an open field worth detailed future investigation. A simple macroscopic model for the evolution of ion-beam induced diffusion of a thin surface layer into an infinitely thick substrate will be presented in Chapter 7.

2.4.4 Ion Energy and Mass

Aside from dependence on intrinsic diffusion properties of target materials and implantation temperature, ion-induced interface reactions can also be affected by the projectile parameters such as ion energy, mass and fluence. In general, the phase obtained is independent of the energy and mass of the incident ions. However, the thickness of the intermixed layer was found to increase with ion energy (in the range of 100-300 keV) and ion mass. This can be expected because energetic heavy ions are more effective in initiating atomic collisions and generating defects in the material; therefore, the mixing process is more pronounced. As an example, Fig. 2.8 shows a plot of intermixed Si atoms cm^{-2}, Q Si, versus square root of ion dose for 450 Å Pt/Si bombarded with 300 keV Xe^+, Kr^+ or Ar^+ at LN_2 temperature. The intermixed layers produced are nonuniform, which suggests the mixing is mostly contributed from the dynamic collision process. As shown in Fig. 2.8, a square root dependence of amount of mixing on ion dose has been observed. The reaction is more pronounced for bombardment with heavy mass ions.

A square root of dose dependence suggests a "diffusion-like" process for the cascade mixing. Since dose is proportional to time, the effective diffusion coefficients ($D^* \alpha\ Q^2/t$) for the mixing induced by Xe^+, Kr^+ or Ar^+ bombardment is proportional to the square of the slope for each straight line shown in Fig. 2.8. Such a calculation gives a ratio $(2.7)^2 : (2.1)^2 : 1^2 = 7.3:4.4:1$ for the effective diffusion coefficients for Xe^+, Kr^+ and Ar^+ implantations. This ratio

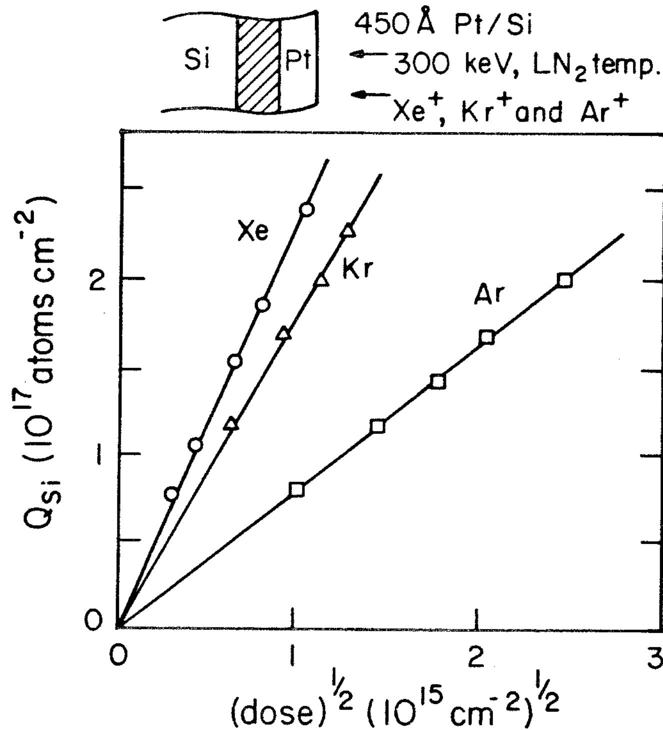

Fig. 2.8 Number of intermixed Si atoms, Q, as a function of the square root of ion dose.

is very close to the ratio of average nuclear energy loss (i.e., energy dissipated in the elastic collision process), $5.8 \times 10^3 : 3.3 \times 10^3 : 0.82 \times 10^3$ (in unit of keV/ μm) ≃ 7.1:4:1, calculated for 300 keV Xe^+, Kr^+ or Ar^+ in a 400 Å Pt film [31]. The approximate agreement between these two ratios is consistent with the theoretical model for the cascade mixing process [21, 32, 33] in which intermixing is considered as a pseudo-diffusion (random walk) process with an effective diffusion coefficient proportional to the nuclear energy loss of the incident projectile.

2.4.5 Ion Dose (Fluence)

In normal thermal treatment the silicide phase grows in thickness with increasing annealing time. Similarly, we found that the thickness of the ion-induced silicide layer increase with ion dose. Both square root of dose and linear dose dependences have been observed. The square root of dose dependence is demonstrated in Fig. 2.9, where the backscattering spectra of an unimplanted 300 Å Ni/Si and two Kr^+ implanted samples are shown superimposed upon one another. The thickness of the Ni_2Si phase increases by a factor of two when a four-fold higher dose is implanted. The linear dose dependence is illustrated in Fig. 2.10 using Cr/Si as an example. The implantations were performed with 300 keV Xe^+ at 250^oC to doses ranging between $2x10^{15}$ and $8x10^{15}cm^{-2}$. Well defined $CrSi_2$ layers are formed and the thicknesses increase linearly with ion doses. In Table II-2, we summarize the kinetics of silicide formation induced by ion-beam mixing in the transition-metal/Si systems. For comparison, the results observed in normal thermal treatment are also included. As can be seen in the table, the formation kinetics of silicides produced by ion-beam-mixing and thermal annealing are almost identical for the systems studied.

This similarity suggests that the atomic processes of silicide formation induced by ion beams may be closely related to those by thermal treatment. For example, a square root dependence on ion dose indicates that the thickening (or growth rate) of the silicide layer is limited by the transport of atomic species through the silicide layer,

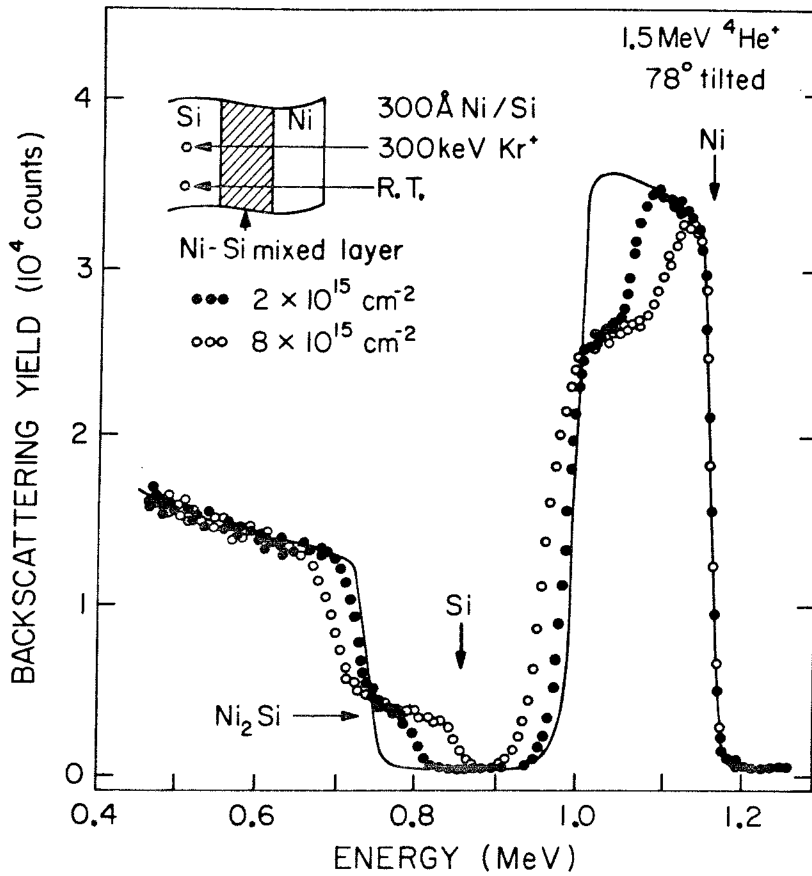

Fig. 2.9. Backscattering spectra of a thin (300 Å) Ni film on a Si substrate after being bombarded with 300 keV Kr ions to two different doses. The Ni_2Si phase is formed near the Ni-Si interface and the thickness of the silicide phase increases with the square root of ion dose.

i.e., the reaction is diffusion controlled. If one incident ion produces an interfacial intermixed region with thickness ℓ, another ion impinging at the same spot will then cause the "growth" of this reacted region to a thickness $\sqrt{2}\,\ell$ (see Fig. 2.2). On the other hand, the linear dose dependence seems to suggest that the reaction is interface (or reaction) controlled. It has been shown that in the case

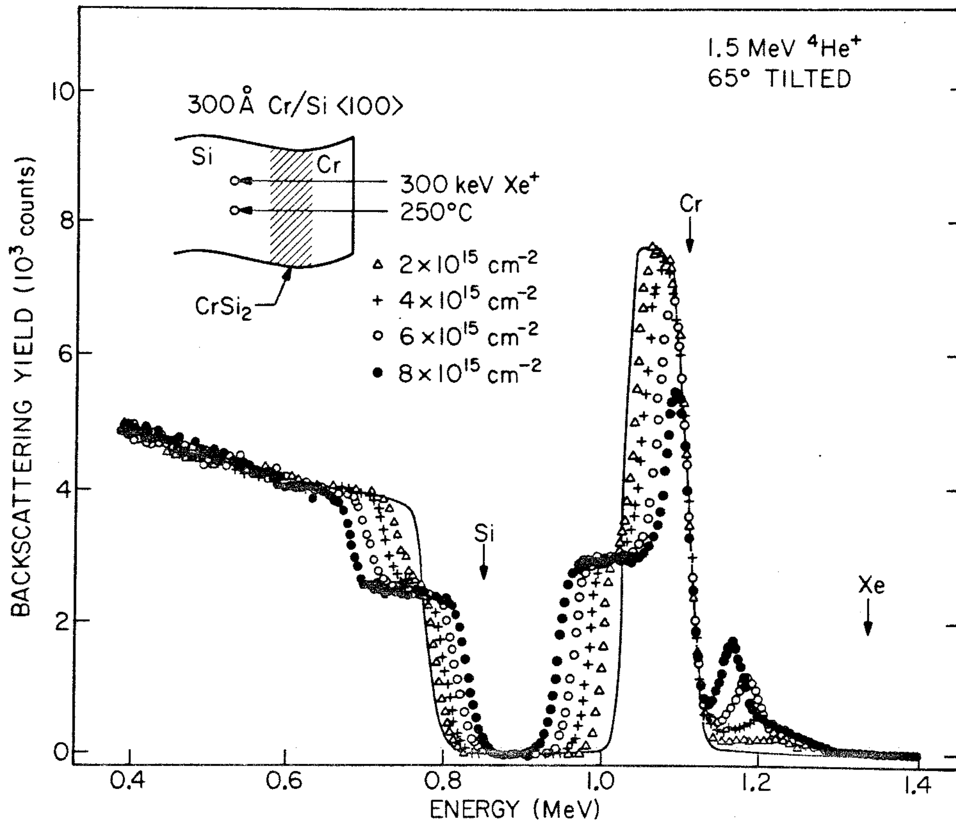

Fig. 2.10. Backscattering spectra which shows the layered growth of the $CrSi_2$ phase induced by ion-beam mixing. The thicknesses of $CrSi_2$ increase linearly with ion doses, which is similar to the kinetics of linear time dependence in normal thermal treatment.

of disilicides Si is the dominant diffusion species in thermal treatment and release of Si atoms from the Si lattices is proposed to be the rate limiting factor for the growth of those disilicides [1]. It is possible that similar mechanisms proceed in the case of ion-beam mixing and the linear dose dependence can be expected because the total amount

TABLE II-2 Kinetics of Silicide Formation Induced by Ion-Beam Mixing and Thermal Annealing

Metal/Si	Impl. Temp.	Compound Observed[a]	Kinetics	
			Ion-Beam	Thermal
Ni/Si	R.T.	Ni_2Si	$(dose)^{1/2}$	$t^{1/2}$
Pd/si	R.T.	Pd_2Si	$(dose)^{1/2}$	$t^{1/2}$
Pt/Si	R.T.	Pt_2Si	$(dose)^{1/2}$	$t^{1/2}$
Co/Si	R.T.	Co_2Si	$(dose)^{1/2}$	$t^{1/2}$
Fe/Si	R.T.	FeSi	$(dose)^{1/2}$	$t^{1/2}$
Cr/Si	$250^{o}C$	$CrSi_2$	dose	t
Nb/Si	$300^{o}C$	$NbSi_2$	dose	t, $t^{1/2}$ [b]
Hf/Si	R.T.	HfSi	$(dose)^{1/2}$	$t^{1/2}$

(a) Compounds obtained by ion-beam mixing are the same as those formed by thermal annealing (see TABLE II-1).

(b) Both t[1] and $t^{1/2}$ [34] dependence have been reported.

of Si released from the substrate should be proportional to the number of incident ions, i.e., the ion doses.

2.4.6. Radiation Stability

One important material parameter which may influence the crystallinity of the silicide produced by ion-beam-mixing is the "radiation stability" (or radiation resistance) of the phase structure. Although formation of compound phases can be initiated by ion-beam, radiation damage will also be produced in the compound during ion bombardment. Therefore, the ability of the phase to maintain its crystal structure will then depend on the stability of the phase structure under ionic irradiation.

It is known that most of the transition-metal silicides possess metallic properties and are called intermetallic compounds, but the degree of metallic bonding varies from one compound to another. Recently, Phillips has pointed out that the heat for formation per metal atom scales with the degree of metal-Si bond covalency in the silicides [35]. For Si atoms then, the bonding is least covalent (or more metallic) in the low ΔH_f compounds (noble-metal silicides) and becomes progressively more covalent as ΔH_f increases (refractory-metal silicides). This argument has been involved by Roth *et al* [36] to explain the observed Si(LVV) peak splitting in their Auger studies of transition-metal silicides. If the bonding is metallic in nature, the compound will be relatively insensitive to radiation damage. The extreme examples are pure metals. On the other hand, if the bonding is more covalent-like, the structure

will be more sensitive to radiation damage. The extreme examples are elemental semiconductors which can be easily made amorphous. As can be seen in Table II-1, well-defined silicide phases have been identified for noble-metal silicides but not for refractory-metal silicides (except for those bombarded at elevated temperatures). These results seem consistent with the picture that noble-metal silicides are metallic bonded in nature and refractor-metal silicides more covalent bonded in nature, consequently, the former should be relatively insensitive to radiation damage. In order to retain crystalline structure in refactory metal silicides, bombardment at elevated substrate temperatures is required so that the defects can be annealed out due to the enhanced defect mobility.

2.5 Ion-Beam-Induced Atomic Mixing at High Ion Doses

As mentioned in Section 2.4.5, the thickness of ion-induced silicide layers increases with ion dose, which is somewhat similar to the "layered growth" of silicide phase by thermal annealing. At higher doses, when all the metals are consumed in forming the silicide phase (first phase), ion-beam mixing can lead to the formation of a more Si-rich phase (second phase), or can produce a disordered metal-Si mixed layer. The former case, which so far has been observed in the Pd/Si system, will be described in Section 2.5.1. The latter case, however, was found to be quite general in other metal/Si systems we have studied and will be described in Section 2.5.2 using Pt/Si as an example. In addition to initiating atomic mixing, ion bombardment with inert gas ions to high doses causes formation of gas bubbles. The bubbles were

found to form predominantly near the interface between the Si substrate and the intermixed layer [37]. This will be discussed in Section 2.5.3.

2.5.1 Formation of Second Silicide Phase-the Pd/Si System

Figure 2.11 shows the backscattering spectra of a sample with a 400 Å Pd film on a Si substrate that has been bombarded with 300 keV Xe^+ to various doses. The Pd_2Si phase is formed at low ion doses; this phase grows consuming all the available Pd and then a second phase, PdSi, starts to form at the Pd_2Si-Si interface with increasing Xe^+ dose. Implantation into samples with a Pd_2Si film (formed by thermal annealing) on a Si substrate produces a similar formation of PdSi, but at somewhat lower doses. Fig. 2.12 shows the backscattering spectra of implanted samples which have been post-annealed at 350°C for various periods. As can be seen in the spectra, an intermixed layer near the Pd_2Si-Si interface is produced due to Xe ion bombardment. Subsequent thermal annealing results in further interdiffusion between the Pd_2Si and the Si atoms underneath. A rather uniform layer with a Pd to Si atomic concentration ratio close to unity is achieved at the final stage of the annealing.

Figure 2.13 shows the x-ray diffraction patterns for the unimplanted Pd_2Si/Si, as implanted and post-annealed samples, respectively. The corresponding backscattering spectra are shown in Fig. 2.12. The Pd_2Si phase formed on Si <100> substrate has polycrystalline structure with a slight texture (Fig. 2.13a). After Xe^+ bombardment, the presence

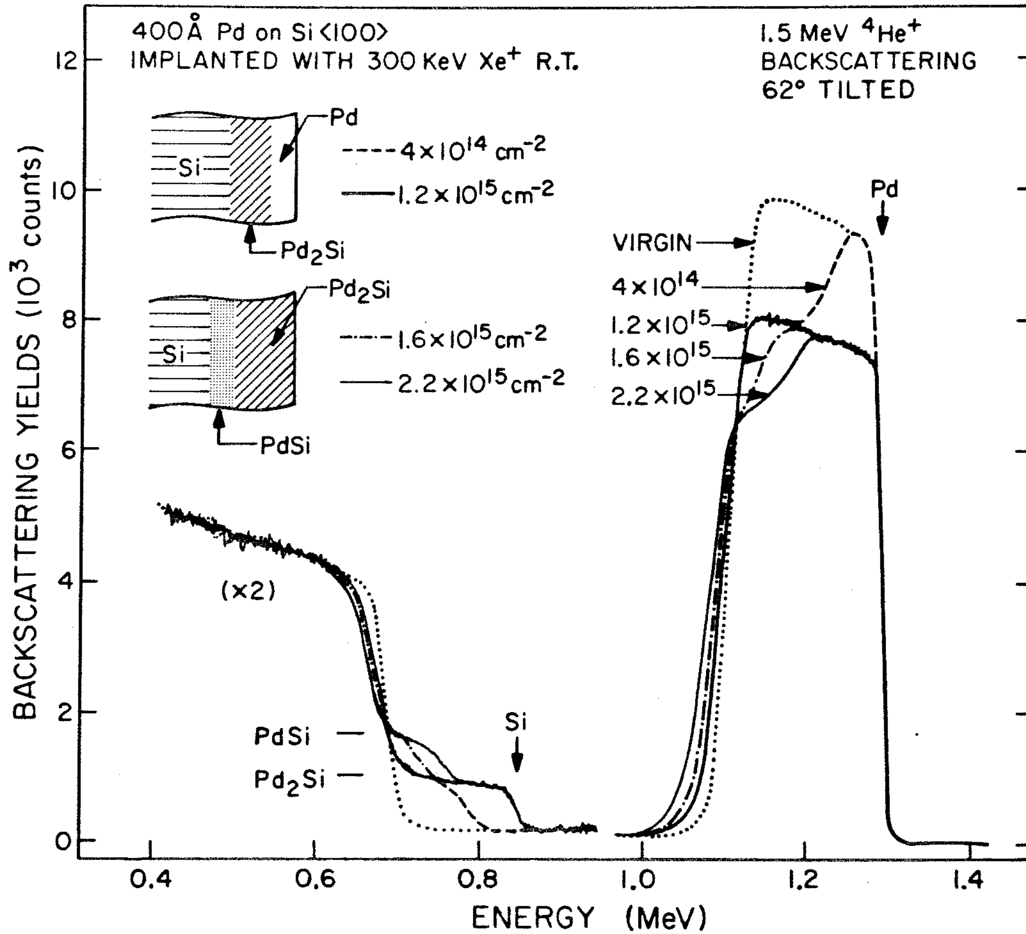

Fig. 2.11 Backscattering spectra of a 400 Å Pd film on Si substrates bombarded with 300 keV Xe^+ at room temperature to various doses. Formation of the Pd_2Si and PdSi is observed at different dose levels.

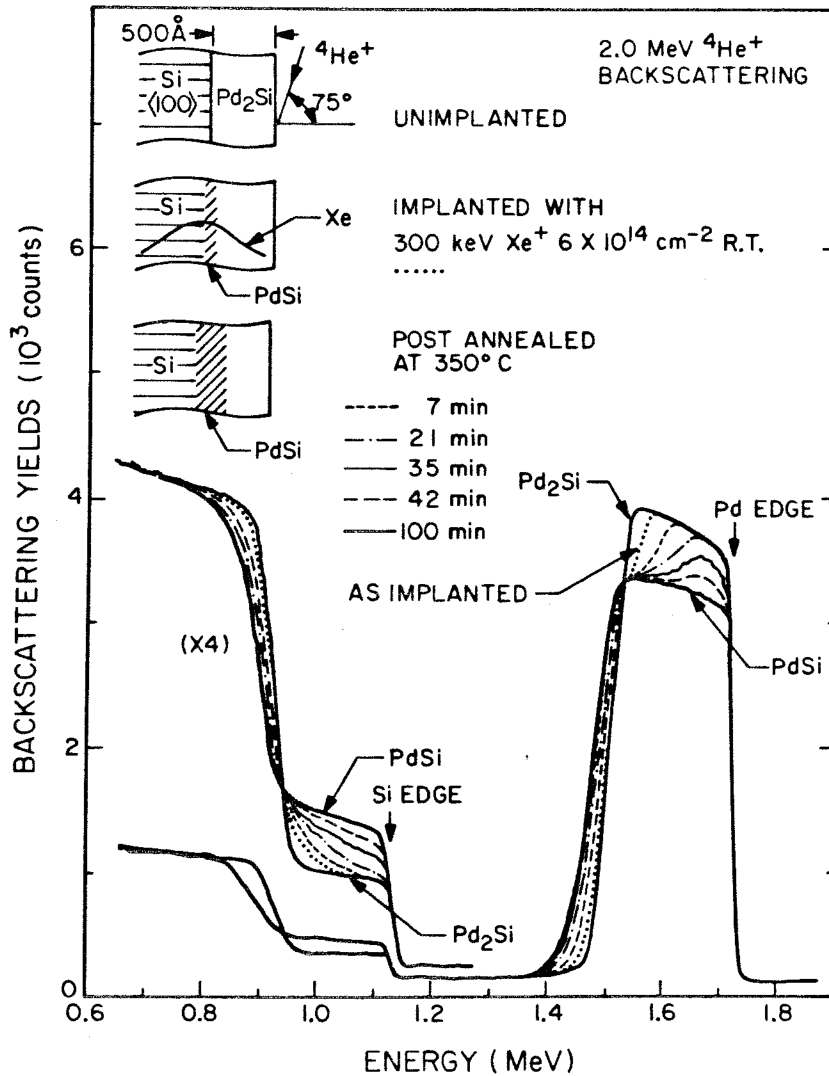

Fig. 2.12 Ion backscattering spectra of a thin Pd_2Si film on a Si substrate bombarded with 300 keV Xe^+ ions at R.T. The PdSi phase was formed near the Pd_2Si-Si interface and the formation of the phase was further promoted by post annealing.

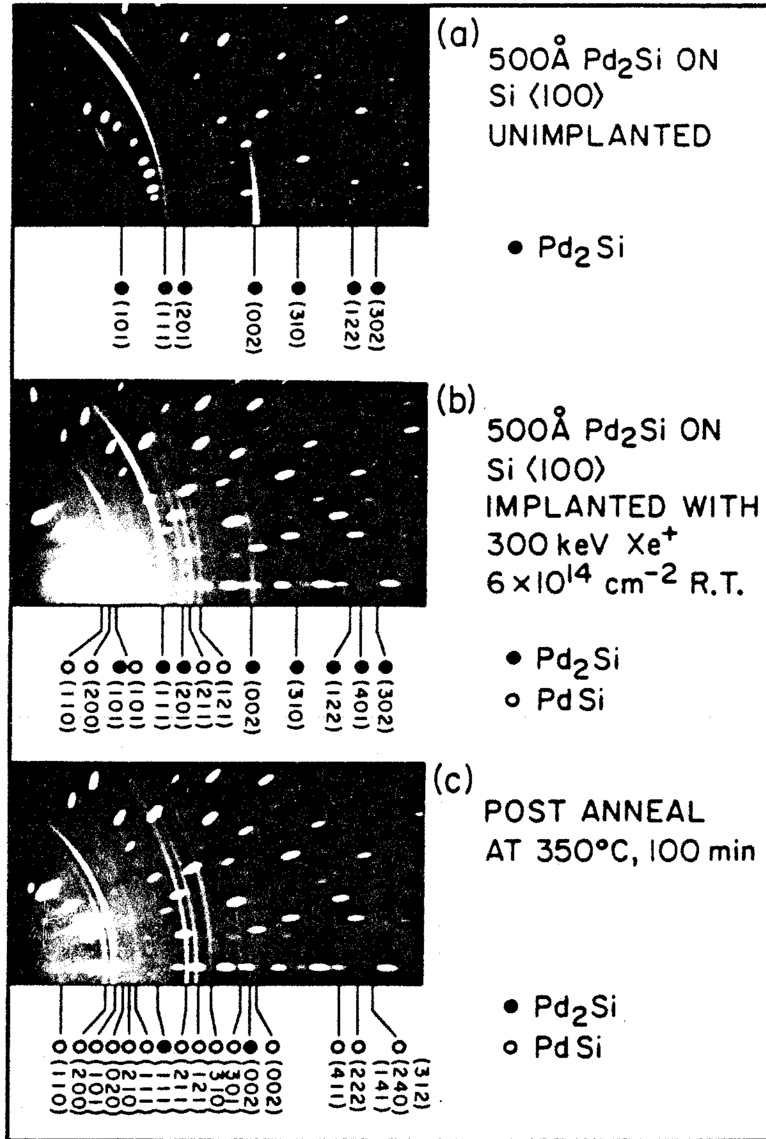

Fig. 2.13 X-ray diffraction patterns taken from a Read camera which demonstrate the formation of the PdSi phase by ion-beam mixing and post-annealing. The diffraction lines have been labeled with plane index according to the ASTM Standards[38].

of the PdSi phase can be detected (Fig. 2.13b). It is formed presumably in the intermixed layer near the Pd_2Si-Si interface. The PdSi phase grows successively after post thermal annealing along with the gradual disappearance of the original Pd_2Si structure. The end phase contains predominantly the PdSi structure as indicated in Fig. 2.13c.

The formation of PdSi by ion-beam mixing and "growth" of this phase at temperatures below 400°C are intriguing. They are in great contrast with the results observed in normal thermal treatment where formation of PdSi required very high temperatures (750-800°C) although the first phase, Pd_2Si, can be formed at rather low temperatures (∿200°C) [39,40]. According to the early work by Hutchins et al [40] and a recent report by R. Anderson et al [41], high temperature formation of PdSi displays a nucleation controlled mechanisms: the phase forms suddenly as islands or rods extending normally through the Pd_2Si film. The islands then grow laterally along with the growth of Si between or inside the islands. The end structure contains discontinuous PdSi islands penetrating deep into the Si substrate.

The reason of high thermal stability of the Pd_2Si phase with respect to the transformation to the PdSi phase is not completely understood. One reason suggested by Tu [1] is that Pd_2Si grows epitaxially on Si single-crystal substrate (especially on (111) surface). This produces a coherent (or semi-coherent) interface of low-free energy, and hence Pd_2Si exhibits high stability. This argument seems consistent with the experimental results by Hutchins et al,

which showed that the nucleation and growth rates of the PdSi phase were inversely related to the crystalline perfection of the Pd_2Si film [40]. We propose that it is the stability of the Pd_2Si-Si interface which prevents low temperature formation of PdSi. Once the interface is disturbed, in our case by ion-beam mixing, nucleation of PdSi may be initiated and it can then grow at temperatures around 400^oC. The silicide layers so obtained are quite uniform in composition and in depth. Resistivity measurements have been performed which showed a value of 18 $\mu\Omega$-cm. This value is lower than the resistivity (25-35 $\mu\Omega$-cm) for thin film Pd_2Si silicide [42,43] and has not been reported before.

2.5.2 Formation of Disordered Metal-Si Mixed layers

In contrast to the Pd/Si system, implantation with higher doses in other transition-metal/Si systems (such as Pt/Si) produces disordered metal-Si mixed layers instead of forming second phase (such as PtSi). X-ray diffraction-measurements indicated a gradual disappearance of the original silicide structure patterns with increasing ion dose. No traces of crystalline reflections were observed during further ion bombardment. As an example, Fig. 2.14 shows the backscattering spectra of two Pt/Si samples with different thicknesses after being bombarded with 300 keV Xe^+ at R.T. to various doses. The Pt_2Si phase was observed at low ion dose ($1x10^{14}cm^{-2}$) in both cases (Fig. 2.14a). The thickness of Pt_2Si increases with ion dose, gradually consuming all the Pt and

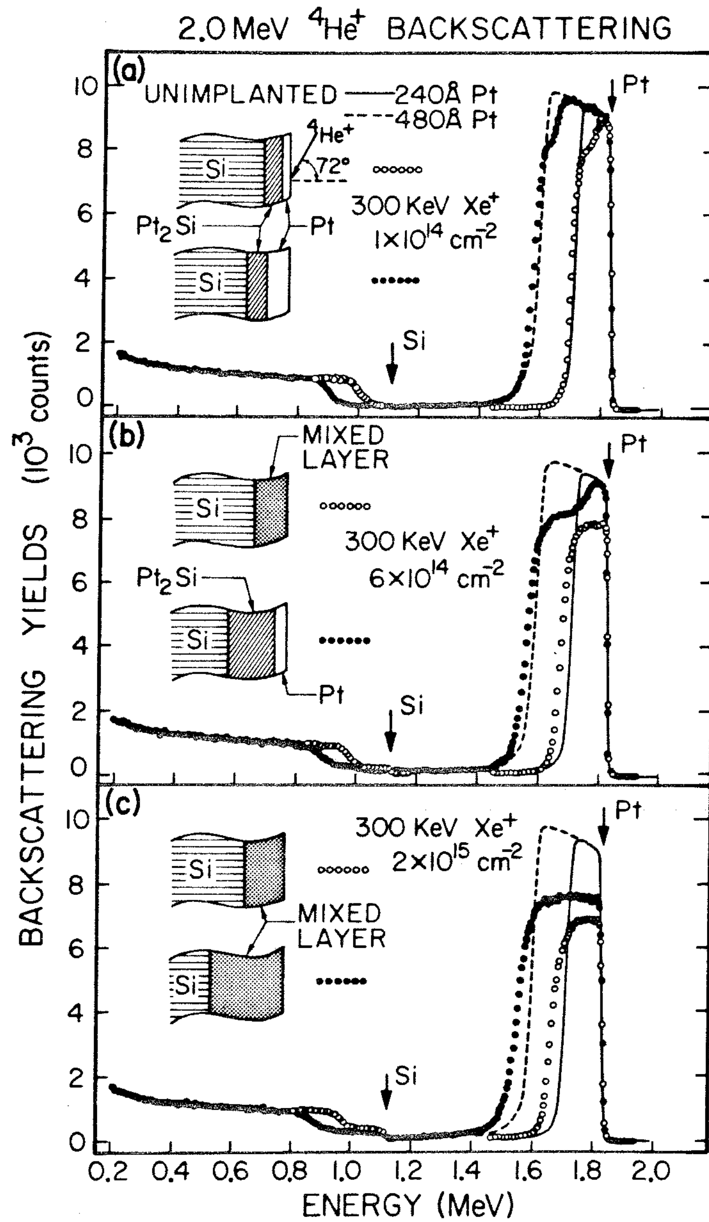

Fig. 2.14 Ion backscattering spectra of two Pt/Si samples with different Pt film thickness after being bombarded with 300 keV Xe^+ to various doses. At low ion dose, the Pt_2Si phase is formed at the interface. The thickness of Pt_2Si increases with ion dose, gradually consuming all the Pt and a Pt-Si mixed layer is formed at high ion doses.

a Pt-Si mixed layer is formed at higher doses. The onset of this transformation is determined by the availability of free Pt; thus, the onset occurs at lower doses for thinner Pt films as shown in Fig. 2.14b and c. Upon further ion bombardment, the Pt is mixed into deeper regions of the Si substrate and the compositon of this mixed layer becomes progressively more Si-rich. This is demonstrated in Fig. 2.15 where the backscattering spectra of two Pt-Si mixed layers resulting from bombardment with two different doses are shown. The mixing process continues until a mixed layer with a thickness roughly corresponding to the ion penetration depth is achieved. After this stage, the thickness of the mixed layer remains approximately constant while the Pt concentration decreases gradually due to successive sputter removal of Pt atoms on the surface. The observation of atomic mixing extending over a depth commensurate with the range of incident ions has been shown earlier in alloy sputtering experiments [44]. This phenomenon was found to have significant influences on sputter-depth-profiling techniques for impurity and interface measurements [44,45].

The formation of amorphous Pt-Si layers instead of the second phase PtSi is somewhat surprising because PtSi can be formed thermally at 300°C after formation of the first phase Pt_2Si. The result is also in contrast with what we found in the Pd/Si system: PdSi can be formed by ion bombardment although formation of PdSi by thermal annealing requires a high temperature (800°C). We attribute the difference in behavior between the Pd system and the Pt system to the stability of PdSi under

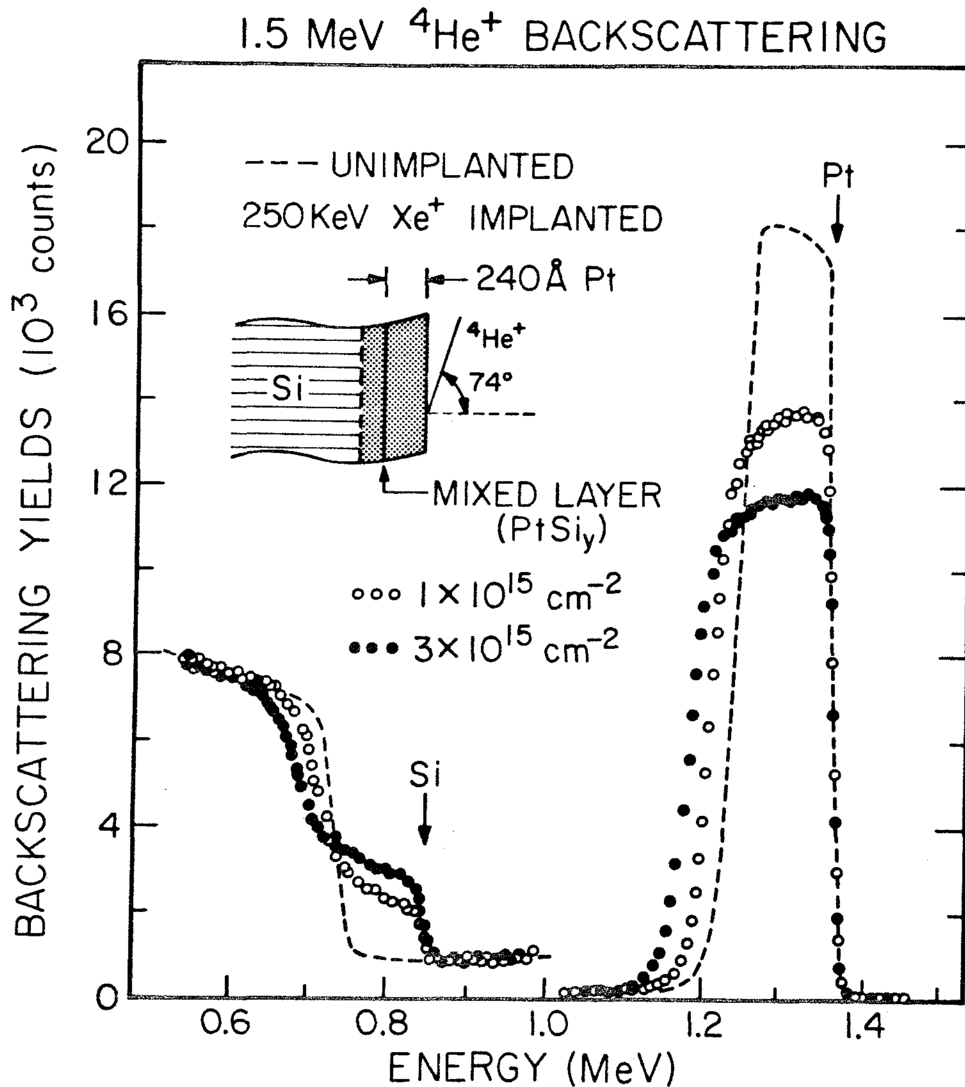

Fig. 2.15 Ion backscattering spectra of a Pt/Si sample bombarded with 250 keV Xe^+ to doses of $1x10^{15}$ and $3x10^{15}$ cm^{-2}, respectively. All the Pt has been consumed in forming Pt_2Si and a disorded Pt-Si mixed layer is formed. The thickness of this intermixed layer increases with ion dose and the composition becomes progressively more Si-rich.

ion bombardment. This is evidenced by the experimental observation that irradiation of samples of PdSi and PtSi with 2×10^{15} Xe ions/cm^2 at an energy of 300 keV resulted in the disappearance of the x-ray diffraction lines of PtSi, but only to a weakening of the PdSi lines.

2.5.3 Formation of Inert-Gas Bubbles at Interfaces

Most of our ion-beam-mixing experiments were carried out using inert-gas ions because they are chemically inert and require only simple ion sources. The presence of implanted gas-ions was found to have minor effects on the silicide formation; identical results were obtained by using Si ions as bombarding species. However, formation of gas bubbles as a result of condensation of implanted gas ions was observed at high implantation doses.

Figure 2.16 shows a series of backscattering spectra of two Cr/Si samples (with different Cr thickness 340 Å and 680 Å, respectively) which have been bombarded with 300 keV Xe^+ at R.T. to various doses. The projected range of Xe in Cr is 500 Å so that the peak of implanted Xe distribution should be underneath the Cr layer (i.e., in the Si substrate) for the case of 340 Å Cr/Si, while the peak should be within the Cr layer for the 680 Å Cr/Si samples. The evolution of Xe distribution shown in Fig. 2.16 indicates the development of a very sharp peak which increases drastically for higher Xe doses (spectra 4,5 and 6 in the figure). The positions of the peak are different for samples with different Cr film thicknesses. Comparisons of the peak position with the film thickness showed that the peak is located at a depth cor-

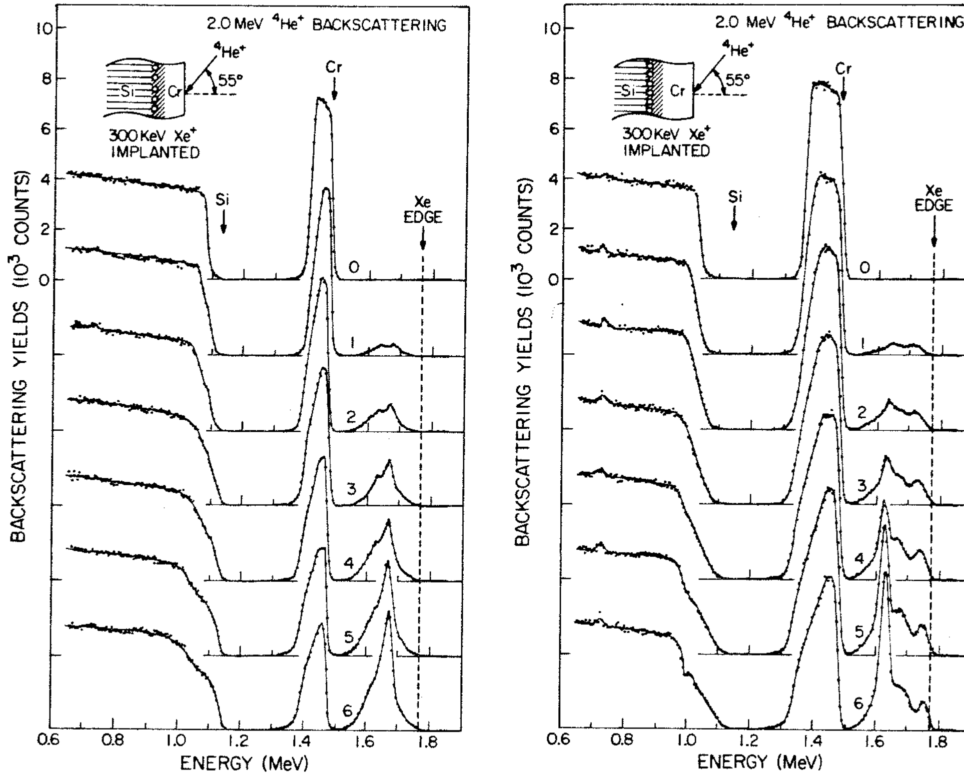

Fig. 2.16 Ion backscattering spectra of a sequence of Xe implanted Cr/Si samples. (a) 340 Å Cr on Si, Xe^+ dose = 0.3×10^{16} cm^{-2} x number, (b) 680 Å Cr on Si, Xe^+ dose = 0.4×10^{16} cm^{-2} x number. The shape and position of the Xe signals indicate Xe bubble formation near the interface between the Si substrate and the Cr-Si intermixed layer.

responding to the interface between the Si substrate and intermixed layer.

It has been demonstrated that the formation of bubbles can affect the shape of implanted gas ion signals in the backscattering spectra[46]. Due to the reduction in energy loss of the He ions in traversing a gas bubble, the signals from the gas in the bubble are characterized by a sharp peak appearing in a narrower region of the spectra. A description of the influence of bubble formation on the backscattering spectra is given in the last part of this section. The formation of a sharp Xe peak as shown in the spectra is therefore an indication of condensation of Xe ions into gas bubbles. The small dip in the Si signal near 1.0 MeV in spectrum 6 of Fig. 2.16b (which is caused by the sharp peak of Xe distribution) provides another evidence for "interfacial" bubble formation.

To further investigate the phenomenon, cross sections of the samples were studied by TEM. Fig. 2.17 shows the result of a Cr/Si sample implanted with Xe under conditions corresponding to those of the sample of spectrum 6 in Fig. 2.16a. As can be seen in the figure, an amorphous Si layer is found, followed by a disordered region underneath. These layers in Si are caused by the bombardment damage of Xe ions and have been previously observed in high-dose implantation in single-crystal Si [47]. Some circular and more transparent regions appearing near the interface between the amorphous Si layer and the surface layer are indications of bubble formation. The surface layer is metal (Cr) enriched and, hence, less transparent in contrast.

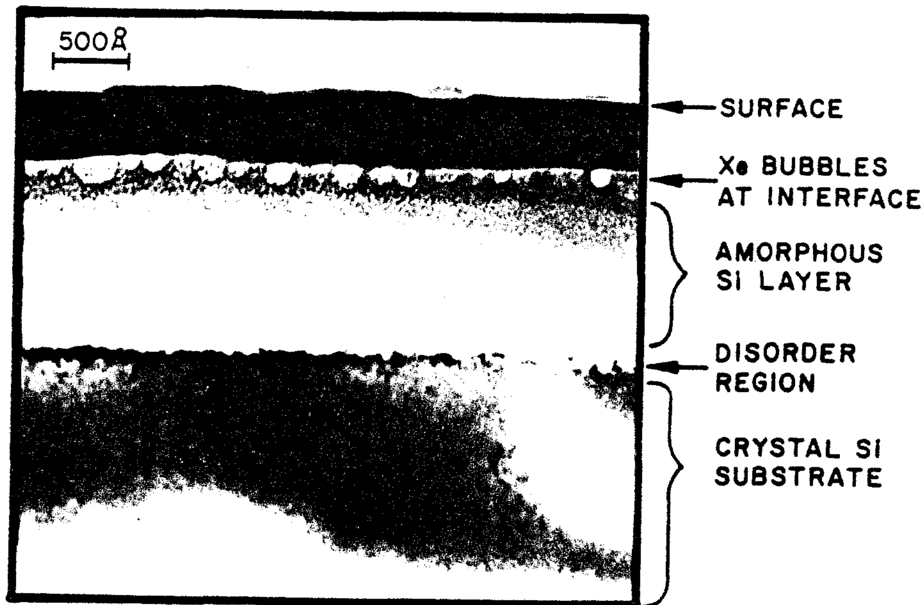

Fig. 2.17. Cross sectional TEM picture showing the Xe bubble formation near the interface between the Si substrate and the surface layer.

Implantation with higher Xe^+ doses have also been carried out. We found that almost the whole surface layer disappear suddenly after a Xe^+ dose of $4x10^{16}cm^{-2}$. The sudden peeling-off of the layer is interpreted as due to either the high pressures in the bubbles or the larger number of bubbles that tend to cover a major portion of the interface area. This phenomenon is consistent with the observation of "interfacial" bubble formation.

It has been found that gas bubbles were most likely to form near the grain boundaries or the dislocation networks produced by ion bombardment for crystalline materials [46,48]. The present case of bubble formation

at the interface is probably due to a similar reason. Our view of this process is that during implantation the Xe ions deposit energy along their track causing enhanced atomic migration throughtout the collision cascade. Any Xe ion within one of the collision cascades tends to migrate to a nucleation site (the interface in this case) and gas bubble is formed. During prolonged bombardment the number of atoms trapped at the bubble continues to grow. This phenomenon was found to be quite general for various thin film systems (Cr/Si, V/Si, Ni/Si, Pd/Si, etc.) and rare-gase ions.

Finally, we would like to discuss briefly the effect of bubble formation on the implanted gas ion signals in the backscattering spectra. This is demonstrated in Fig. 2.18. Suppose there are equal numbers of Xe ions distributed in the same depth region near the interface between the Si substrate and a surface metal-Si mixed layer of samples A and B. The shapes of the Xe signals in the backscattering spectra will, however, look rather different if, in case A, the gas atoms are uniformly embedded in the material, while in case B the ions condense to form bubbles. This is because, in backscattering analysis, the He ions suffer much less energy loss traveling through the bubble atmosphere than through the solid materials. Therefore, with bubble formation, the signals will appear in a narrower region (and, hence, larger signal height) in the backscattering spectrum. In addition, a depression of Si signals near the interface will be observed if the number of Xe ions trapped in the bubbles is sufficiently large. Considering a Xe distribution over the surface layer and across the inter-

face, the profiles will be a superposition of a normal range distribution and a narrow peak if the implanted ions near the interface tend to form gas bubbles at the interface. Thus, the present argument seems quite consistent with the observed Xe bubble formation as illustrated in Fig. 2.16.

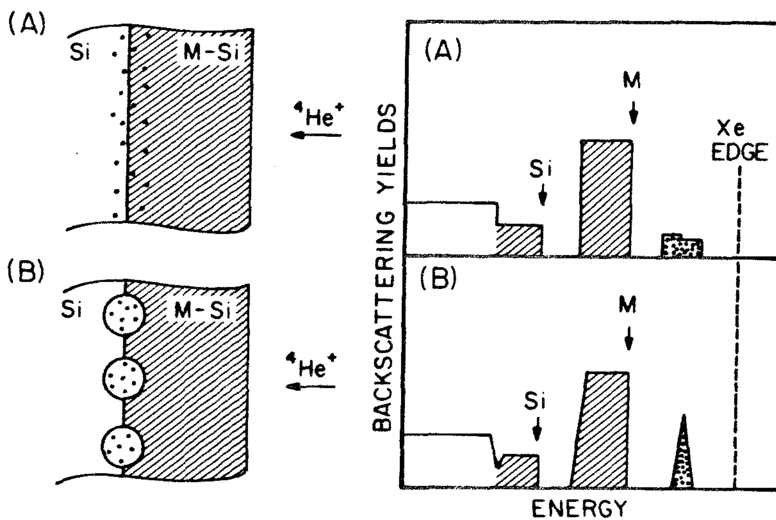

Fig. 2.18. A schematic picture which illustrates the effect of bubble formation on the backscattering spectrum. The dots represent Xe atoms in the samples. For equal numbers of Xe atoms in samples A and B the area under the Xe signals of A and B should be approximately equal. Bubble formation causes the Xe spectrum to sharpen up.

2.6 Conclusion

In summary, ion-induced interface mixing and compound formation as a result of energetic ion bombardment through a thin transition-metal film on a Si substrate have been observed. A schematic summary for the

evolution of ion-induced interface reactions with ion doses are shown in Fig. 2.19 using the Pt/Si and Pd/Si systems as examples. No appreciable reaction is observed if the ions do not reach beyond the interface. The initial phases (Pt_2Si and Pd_2Si) formed when the ion-beams penetrate through the interface are the same as those formed in thermal treatments. The thicknesses of the silicide layers increase with ion doses, which is similar to the "layered growth" of silicide phases by thermal annealing.

At higher doses, when all the metals are consumed in forming the metal-rich silicides, ion beam mixing can lead to the formation of a more silicon-rich phase or can produce an amorphous metal-silicon mixed layer. For example, the PdSi phase is formed near the Pd_2Si-Si interface; a phase that is extremely difficult to form by thermal treatment of Pd film on Si. In contrast with the Pd-Si system, implantation with higher doses in the Pt-Si system (and other transition-metal/Si systems) produces an amorphous Pt-Si mixed layer instead of forming a second-phase (PtSi). The layer becomes progressively more Si-rich with increasing ion dose because of the incorporation of more Si atoms from the substrate into the intermixed layer. The final stage of mixing extends to a depth roughly corresponding to the ion penetration range.

The atomic mechanisms involved in the interface mixing process are complicated. Comparisons of results observed in different metal/Si systems indicate that the mixing process and its products are strongly influenced by the implantation conditions such as ion energy, mass,

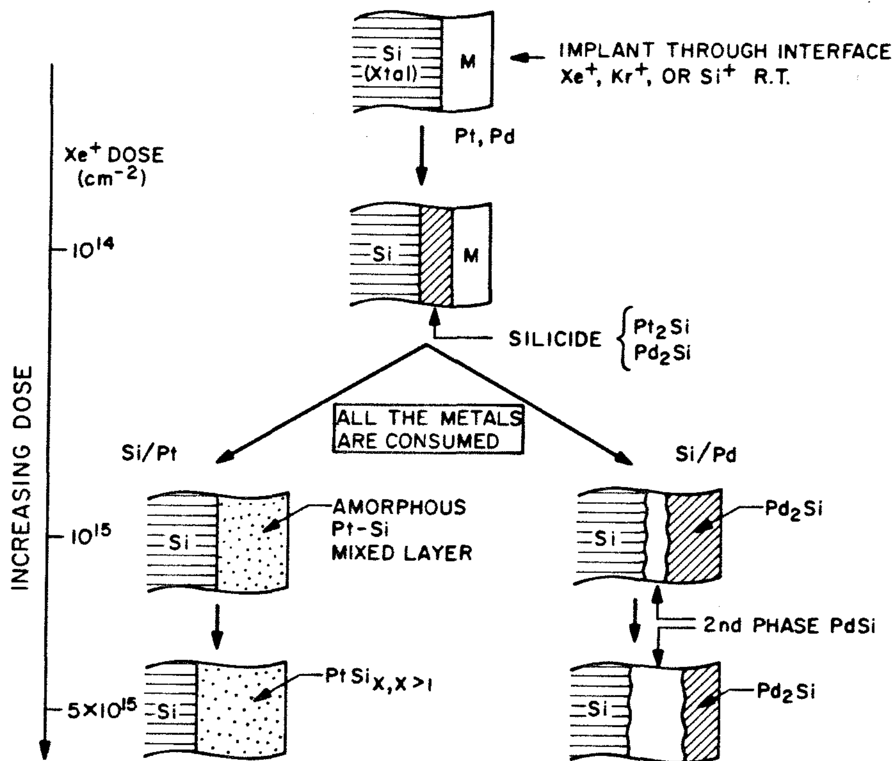

Fig. 2.19. Schematic diagram showing the ion-beam-induced interface reactions in metal/Si systems.

fluence and substrate temperature, and also by the intrinsic properties of the target materials such as thermal diffusivity and radiation stability. The mechanisms of interface mixing and factors affecting the formation and properties of these ion-induced silicides are summarized as follows:

(1) Ion-induced interface reaction is considered as being composed of many localized elemental processes, each initiated by one incident ion. At low ion doses, isolated intermixed regions are formed

near the interface. With increasing ion dose the reacted regions tend to cover the whole interface and further intermixing is promoted due to overlapping of mixed regions. Under prolonged bombardment, a continous intermixed layer is formed and the thickness increases with ion doses.

(2) Two mechanisms have been proposed for the interface reaction: (i) dynamic cascade mixing and (ii) radiation-enhanced diffusion. Cascade mixing is a process in which atoms are transported by successive displacements which arise from repeated collision cascades. It is primarily responsible for the mixing observed at lower temperatures in that graded intermixed layers lacking ordered phase structure are usually formed. The reaction induced by cascade mixing depends mainly on the energy deposited in the elastic collision process and the process is relatively insensitive to temperature. In high temperature regime, radiation-enhanced diffusion is the dominant mechanism for intermixing because the displaced atoms (due to cascade mixing) would have enough mobility to diffuse (to a long range) under the presence of bombardment-induced defects. Formation of uniform mixed layers with well-defined phase structuresa are usually observed. Morever, the process exhibits a strong temperature dependence in that the mixing increases drastically with increasing temperature.

(3) The phenomenon of ion-induced silicide formation was found to display a strong metallurgical dependence in the sense that the mixing is more pronounced for systems which tend to react (interdiffuse) thermally at lower temperatures. Moreover, the radiation stability of the phase structure also plays an important role in determining

whether the phase can maintain its crystalline structure during the bombardment or not.

(4) The ion-induced silicide formation show a square root or linear dependence of thickness on ion dose, which is similar to the kinetics of square root or linear time dependence in normal thermal treatment. This similarity suggests the atomic processes of silicide formation induced by ion beams may be closely related to those involved in the reactions by thermal treatment.

REFERENCES

1. See, for example, K. N. Tu and J. W. Mayer, in Thin-Films - Interdiffusion and Reactions, J. M. Poate, K. N. Tu and J. W. Mayer, Eds., (Wiley, New York, 1978), Chapter 10.
2. J. A. Borders and S. T. Picraux, Proc. IEEE 62, 1224 (1974).
3. J. W. Mayer and K. N. Tu, J. Vac. Sci. Technol. 11, 86 (1974).
4. W. K. Chu, J. W. Mayer and M-A. Nicolet, Backscattering Spectrometry (Academic Press, New York, 1978).
5. K. N. Tu and S. S. Lau, in Thin-Films-Interdiffusion and Reactions, J. M. Poate, K. N. Tu and J. W. Mayer, Eds., (Wiley, New York, 1978) Chapter 5.
6. B. Y. Tsaur, Z. L. Liau and J. W. Mayer, Appl. Phys. Lett. 34, 168 (1979).
7. W. F. van der Weg, D. Sigurd and J. W. Mayer, in Applications of Ion Beams to Metals, S. T. Picraux, E. P. EerNisse, and F. L. Vook, Eds., (Plenum Press, New York, 1974), p. 209.
8. G. Chapman, S. S. Lau and J. W. Mayer, J. Appl. Phys. 50, 6231 (1979).
9. B. Y. Tsaur, S. S. Lau and J. W. Mayer, Appl. Phys. Lett. 35, 225 (1979).
10. B. Y. Tsaur, Electrochemical Society Meeting, Oct. 1979, Los Angeles, paper to be published in the Proceedings of Thin-Film Symposium.
11. S. S. Lau, J. W. Mayer, B. Y. Tsaur and M. von Allmen, Material Research Society Meeting, Nov. 1979, Boston, paper to be published in the Proceedings of Laser and Electron Beam Processing of Materials.

12. T. Kanayama, H. Tanoue, and T. Tsurushima, Appl. Phys. Lett. 35, 222 (1979).
13. S. Matteson, J. Roth and M-A. Nicolet, Rad. Effects (in press).
14. G. Dearnaley, J. H. Freeman, R. S. Nelson and T. Stephen, Ion Implantation, (North-Holland Publishing Company, Amsterdam, 1973), p. 421.
15. R. S. Nelson, Rad. Effects, 2, 47 (1969).
16. J. A. McHugh, Rad. Effects 21, 209 (1974).
17. R. R. Hart, H. L. Dunlap, and O. J. Marsh, J. Appl. Phys. 46, 277 (1975).
18. W. Wach and K. Wittmaack, Nucl. Instrum. Methods, 149, 259 (1978).
19. T. Ishitani, R. Shimizu and H. Tamura, Appl. Phys. 6, 277 (1975).
20. T. J. Chuang and K. Wandelt, IBM J. Res. Develop. 22, 277 (1978).
21. P. K. Haff and Z. E. Switkowski, J. Appl. Phys. 48, 3383 (1977).
22. T. Ishitani and R. Schimizu, Appl. Phys. 6, 241 (1975).
23. Z. L. Liau and B. Y. Tsaur (unpublished).
24. S. S. Lau, J. W. Mayer and K. N. Tu, J. Appl. Phys. 49, 4005 (1978).
25. G. Dearnaley, in Ref. 14, page 228.
26. R. L. Minear, D. G. Nelson and J. F. Gibbons, J. Appl. Phys. 43, 3468 (1972).
27. S. M. Myers and S. T. Picraux, J. Appl. Phys. 46, 4774 (1975).
28. G. J. Dienes and A. C. Damask, J. Appl. Phys. 29, 1713 (1958).
29. B. Masters and E. Gorey, J. Appl. Phys. 49, 2717 (1978).
30. H. Ryssel, et al, in Ion Implantation in Semiconductors, (Plenum, New York and London, 1975), p. 169.

31. J. F. Gibbons, W. S. Johnson and S. W. Mylroie, Projected Range Statistics - Semiconductors and Related Materials, 2nd Edition, (Dowden, Hutchinson & Ross, Inc., 1975).

32. B. Y. Tsaur, S. Matteson, G. Chapman, Z. L. Liau and M-A. Nicolet, 35, 825 (1979).

33. S. Matteson, G. Mezey and M-A. Nicolet, Electrochemical Society Meeting, Oct. 1979, Los Angeles.

34. R. J. Wagner, S. S. Lau, J. W. Mayer and J. A. Roth, Proceedings of Thin-Film Phenomena - Interfaces and Interactions, J.E.E. Baglin and J. M. Poate, Eds. (Electrochemical Society, 1978) p. 66.

35. J. M. Andrews and J. C. Phillips, Phys. Rev. Lett. 35, 56 (1975).

36. J. A. Roth and C. R. Crowell, J. Vac. Sci. Technol. 15, 1317 (1979).

37. B. Y. Tsaur, Z. L. Liau, J. W. Mayer, J. Appl. Phys. 50, 3978 (1979).

38. ASTM cards No. 6-0559 (Pd_2Si) and No. 7-127 (PdSi).

39. R. W. Bower, R. E. Scott and D. Sigurd, Solid-State Electron. 16, 1461 (1973).

40. G. A. Hutchins and A. Shepela, Thin Solid Films, 18, 343 (1973).

41. R. Anderson, J. Baglin, J. Dempsey, W. Hammer, F. d'Heurle and S. Petersson, Appl. Phys. Lett. 35, 285 (1979).

42. C. Canali, F. Catellani, S. Mantovani and M. Prudenziati, J. Phys. D. Appl. Phys. 10, 2481 (1977).

43. M. Wittmer, D. L. Smith, P. W. Lew and M-A. Nicolet, Solid-State Electron. 21, 573 (1978).

44. Z. L. Liau, Thesis, California Institute of Technology (1979).

45. Z. L. Liau, B. Y. Tsaur, J. W. Mayer, J. Vac. Sci. Technol. 16, 121 (1979).

46. Z. L. Liau and T. T. Sheng, Appl. Phys. Lett. 32, 716 (1978).

47. L. Csepregi, E. F. Kennedy, S. S. Lau, J. W. Mayer and T. W. Sigmon, Appl. Phys. Lett. 29, 645 (1976).
T. E. Seidel, G. A. Pasteur and J. C. C. Tsai, Appl. Phys. Lett. 29, 648 (1976).

48. G. Dearnaley, in Ref. 14, page 245.

Chapter 3

ION-BEAM-INDUCED METASTABLE Pt_2Si_3 PHASE – FORMATION, STRUCTURE AND PROPERTIES

3.1 Introduction

In Chapter 2, we reported silicide formation induced by energetic ion bombardment through a thin metal-film on a Si substrate. Many similarities have been found between ion-beam-mixing and thermal annealing in producing silicide phases. Formation of equilibrium silicide phases is, perhaps, not unexpected because it is energetically favorable and, moreover, metal-Si interfaces are thermally unstable so that reactions will take place if energy is provided. However, nonequilibrium structures can also be produced under certain implantation conditions. For example, disordered metal-Si mixtures are usually formed at high implantation doses (Section 2.5.2). The compositions of those mixed layers may be far from those of equilibrium compounds. Relaxation from a disordered structure (which is in a high energy state) to a state closer to thermal equilibrium will then proceed upon post-thermal treatments. This opens the possibility of producing nonequilibrium phases (or the so-called metastable phases) with composition and structure distinctly different from those of equilibrium compounds.

In the present investigation, implantations with energetic ions through a thin PtSi film on a Si substrate have been performed in an attempt to modify the thermally stable interface. The PtSi phase, which is known to exist in equilibrium [1] with Si, can be formed by thermal treatments of Pt on Si at temperatures of 300-350°C [2]. At

higher temperatures, agglomeration between PtSi and Si occurs [3] but no new phases have been detected. By using ion-beam mixing, a Si-rich metastable phase of Pt_2Si_3 composition has been obtained. We present in this chapter experimental results of the formation, crystal structure, and properties of the ion-induced Pt_2Si_3 phase studied by a combination of $^4He^+$ backscattering, glancing incidence x-ray diffraction and superconducting T_c measurements. In the next chapter, we report the kinetics of phase formation, morphology and microstructural changes of the ion-induced Pt-Si layers during phase transformation studied by using resistivity measurements and transmission electron microscopy and diffraction.

3.2 Ion-Beam-Induced Interface Mixing of PtSi on Si and Formation of the Metastable Pt_2Si_3 Phase

Figure 3.1 shows a series of backscattering spectra which demonstrate the formation of the Pt_2Si_3 phase by ion-beam mixing and post annealing. The virgin samples consisting of a 300 Å PtSi film on Si substrates were bombarded with 300 keV Xe^+ to a dose of $1 \times 10^{15} cm^{-2}$ and annealed subsequently at 400^oC for various periods. As can be seen in the spectra, the PtSi film has been mixed with Si atoms from the substrate and a Si-riched Pt-Si mixed layer is formed. The composition of the layer varies in depth, and the Si/Pt concentration ratio is changing from 1.34 at the surface to 1.65 at the interface. X-ray diffraction measurements showed the disappearance of crystalline diffraction reflections of the original PtSi phase, yet no reflections of

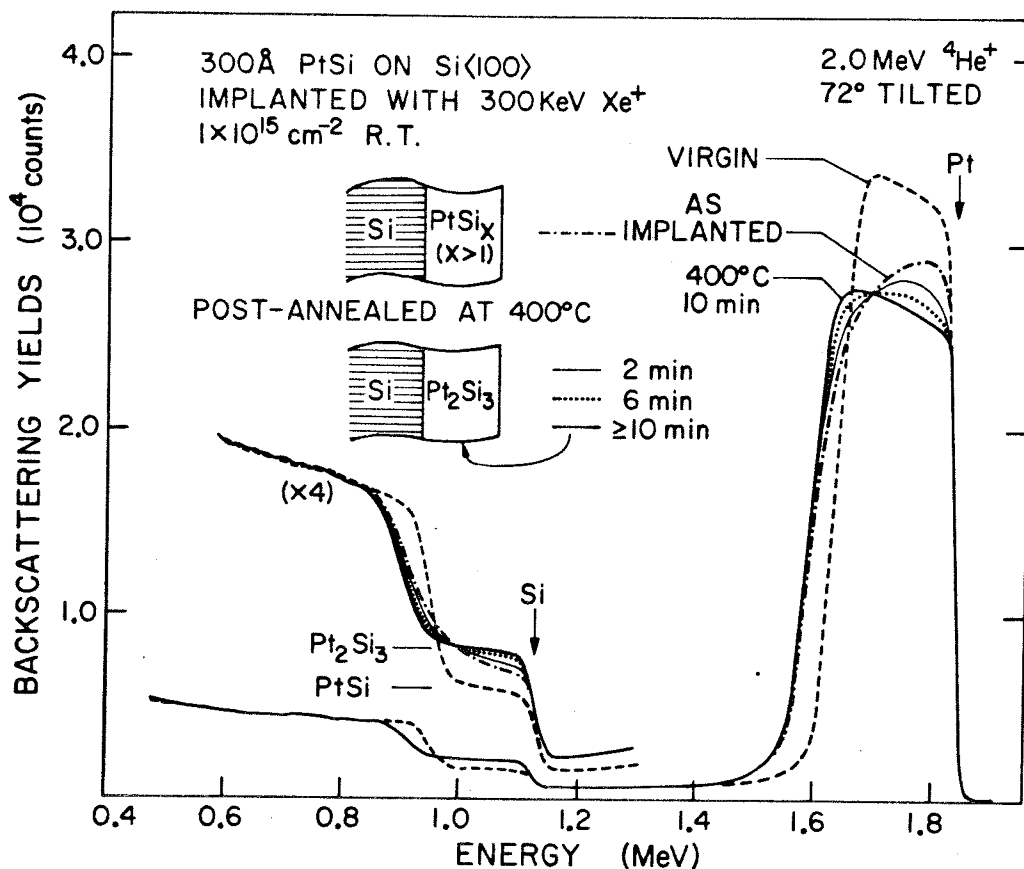

Fig. 3.1 Ion backscattering spectra which demonstrate the formation of the metastable Pt_2Si_3 phase by ion-beam mixing and post-annealing. A thin PtSi film 300 Å thick on a Si<100> substrate was first converted into an amorphous Pt-Si mixed layer by Xe ion bombardment. The layer then transformed into a metastable phase of Pt_2Si_3 composition upon post-annealing.

a new crystalline phase were detected. This ion-induced Pt-Si mixture is presumably amorphous and may contain a small amount of microcrystallites of small size ($\lesssim 100$ Å) whose total amount is beyond the detection limit of the present technique. Post annealing of the samples (2 and 6 min at 400°C in Fig. 3.1) results in a redistribution of Pt and Si atoms in the mixed layer. A uniform layer with a Si to Pt concentration ratio close to 1.5 is achieved after 10 min heat-treatment at 400°C. X-ray diffraction measurements indicated a weak appearance of crystalline diffraction lines. The composition then remained unchanged for longer annealings (up to 1 hr) and a set of crystalline reflections was clearly obtained; these reflections have been determined to belong to a metastable Pt_2Si_3 phase (described in Section 3.4). A similar transformation has also been observed at lower temperatures (350-400°C), but a longer annealing time is required for the complete formation of the new crystalline phase.

The stoichiometric composition of this crystalline phase measured by backscattering technique is determined to be Pt_2Si_3 with an uncertainty less than ±3%. This atomic ratio has been measured repeatedly in several samples with slightly different film thicknesses and Xe ion doses, and was found to be quite reproducible within experimental errors. The Pt_2Si_3 crystalline phase remained a uniform layered structure on Si upon annealings up to 500°C for 30 min. However, significant changes in both composition and structure were observed for a longer annealing time (500°C, $\gtrsim$ 2 hr) or at higher annealing temperatures ($\gtrsim 550^{o}$C). The thermal stability of this ion-induced metastable phase will be discussed in Section 3.5.

3.3 Effects of Bombardment with Different Ion Doses and Ion Species on the Interface Mixing and Compound Formation

A series of Xe implantations into PtSi/Si with doses ranging from 2×10^{14} to $1\times10^{16}cm^{-2}$ were performed to produce a different amount of intermixing at the PtSi-Si interface. The samples were then annealed subsequently at 400°C for 30 minutes. Fig. 3.2 shows the backscattering spectra for the virgin PtSi/Si, as-implanted (to a dose of $4\times10^{14}cm^{-2}$) and post-annealed (400°C, 30 min) samples. Ion bombardment at this dose level has induced a Si-rich Pt-Si mixed layer near the interface but the PtSi film near the surface remains undisturbed in composition. X-ray diffraction measurement showed a weakening in reflection intensity of the PtSi crystalline phase presumably due to the formation of the interfacial mixed layer by ion bombardment. However, a thin but uniform layer with Pt_2Si_3 composition between PtSi and Si was formed upon annealing as shown by a well-defined step in the Pt (or Si) signal in the spectrum. The presence of this Pt_2Si_3 crystalline phase was confirmed by x-ray measurement, which showed two sets of crystalline diffraction reflections; one belongs to PtSi and the other to the Pt_2Si_3 phase.

As can be seen in Fig. 3.1 and Fig. 3.2, some redistribution of Pt and Si atoms occurs within the mixed layer during the annealing. This effect is even more significant for samples implanted with higher doses. Figure 3.3 shows the backscattering spectra of two samples which have been bombarded to higher doses of $3\times10^{15}cm^{-2}$ (Fig. 3.3a) and $5\times10^{15}cm^{-2}$ (Fig. 3.3b), respectively, and then annealed at 400°C for

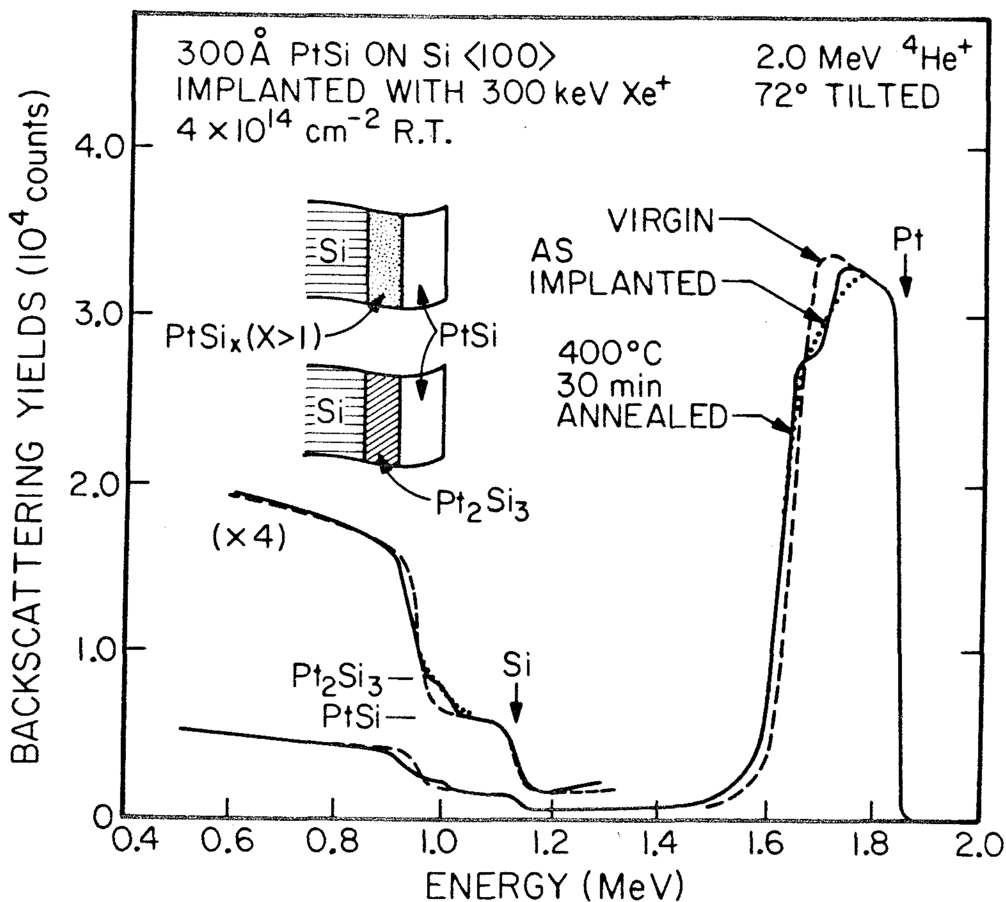

Figure 3.2 Backscattering spectra for a PtSi/Si <100> sample which has been bombarded with 300 keV Xe ions of $4 \times 10^{14} cm^{-2}$ dose and annealed subsequently at $400^{o}C$ for 30 min. A well-defined layer of composition close to Pt_2Si_3 was formed near the PtSi-Si interface.

30 min. As can be seen in the spectra, higher implantation doses resulted in further mixing between the Pt-Si layer and the Si substrate so that the composition of the mixed layer became progressively more Si-rich. After annealing, the surface layer has separated into

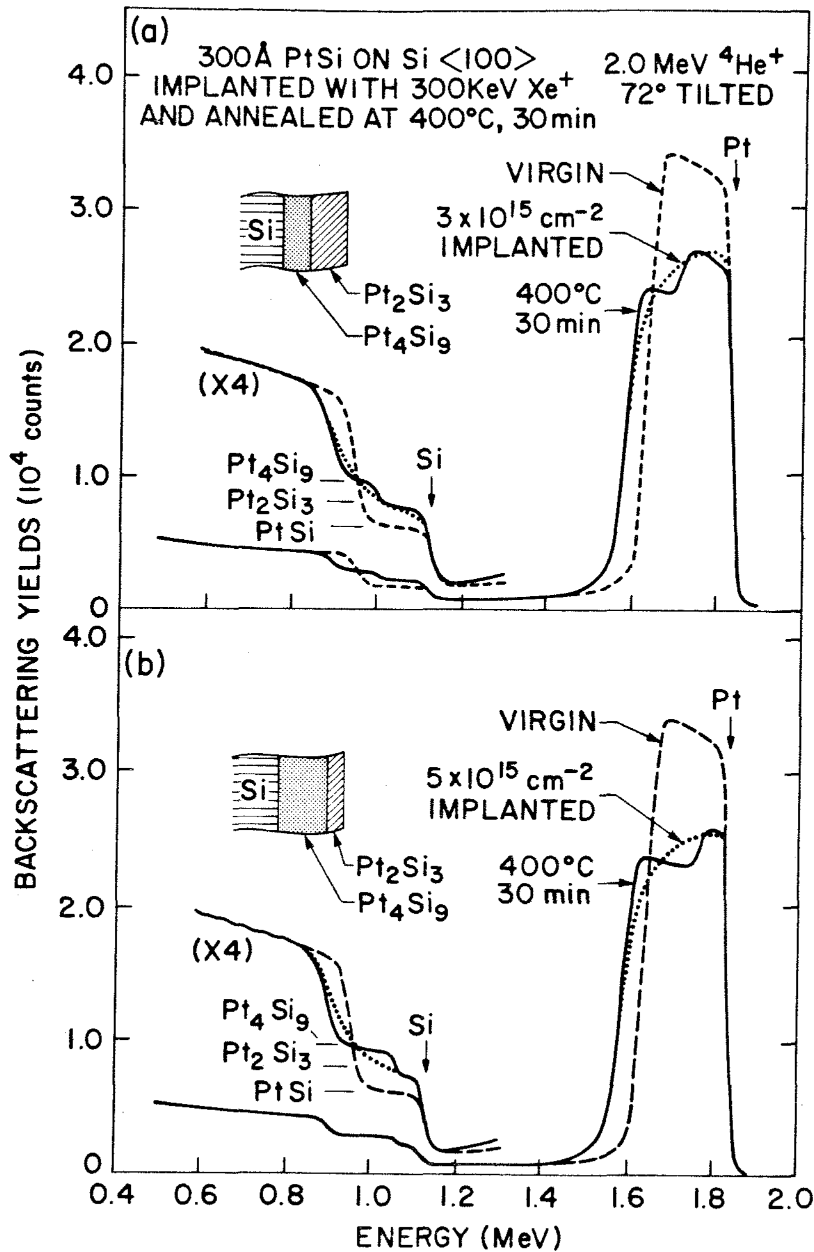

Fig. 3.3 Ion backscattering spectra for two PtSi/Si samples bombarded with 300 keV Xe ions of (a) $3x10^{15}$ cm^{-2} and (b) $5x10^{15}$ cm^{-2}, respectively, and annealed at $400^{0}C$ for 30 min. Two distint layers of compositions Pt_2Si_3 and Pt_4Si_9 have been formed. The thickness of the Pt_4Si_9 layer is thicker for sample implanted with higher Xe ion dose.

two distinct regions as indicated by the steps in the Pt and Si signals. The layer on the surface has a composition close to Pt_2Si_3, but the layer underneath it is even more Si-rich with a composition near $PtSi_{2.25}$ (or Pt_4Si_9). The interface between these two layers is well-defined and shifts progressively toward the surface with increasing ion dose. Eventually, a uniform layer with a composition near Pt_4Si_9 was established for Xe doses greater than $6x10^{15}cm^{-2}$ (up to $1x10^{16}cm^{-2}$). X-ray analysis of samples with Pt_4Si_9 composition also showed the presence of crystalline diffraction reflections and they are different from those of the Pt_2Si_3 phase. A comparison of x-ray diffraction patterns observed on different sample configurations will be summarized in the next section.

The selection of Xe as the bombarding ion species has been arbitrary. Xenon was used because it is chemically inert and requires only simple ion source. However, to eliminate the possible impurity effects on the formation of metastable compounds, experiments have been repeated using Si ions as the bombarding species. The same results as produced by Xe ion bombardment were obtained except that higher ion doses ($5x10^{15}$ - $2x10^{16}cm^{-2}$) were required to achieve the same amount of "intermixing" at the PtSi-Si interface. The difference in doses is because Xe (M=132) is much heavier than Si (M=28), and hence the former is more effective in achieving interfacial mixing [4,5].

In addition to initiating atomic mixing, ion bombardment has also produced an amorphous Si layer, which extended $\sim$1000 Å underneath the Pt-Si mixture as indicated by channeling measurements. The amorphous Si recrystallized at temperatures about 550°C. Some interdiffusion

between the Pt-Si layer and the crystallized Si was observed at temperatures above 550°C. This phenomenon will be described in Section 3.5.

A schematic summary of ion-beam-mixing of PtSi/Si with various Xe ion doses and phases obtained after post-annealing (400°C, 30 min) is shown in Fig. 3.4. Intermixing starts at the interface between PtSi and Si, gradually consumes all the PtSi, and then forms Pt-Si mixed layers with increasing Si concentration. Upon post-annealing (400°C, 30 min), redistribution of atoms within the mixed layer occurs along with formation of metastable phases. No significant interdiffusion between the Si substrate and the Pt-Si mixed layer is observed during the annealing. The resulting phases are strongly dependent on the initial composition of the mixed layer.

3.4 X-Ray Diffraction Analysis and Crystal Structure

The crystal structure of the metastable phases were analyzed by glancing incidence x-ray diffraction with CuKα radiation in a Read camera and a Seemann-Bohlin diffractometer. The highly sensitive Seemann-Bohlin technique was used in view of the small film thicknesses (≲500 Å) and the requirement for high accuracy in the determination of lattice spacings [6]. The wide film Read camera method can give information about textured structure of polycrystalline films. The preferred orientation can then be defined on the basis of sterographic projections.

Figure 3.5 shows the Seemann-Bohlin x-ray diffraction spectrum for a sample with Pt_2Si_3 composition. The total thickness of the layer is

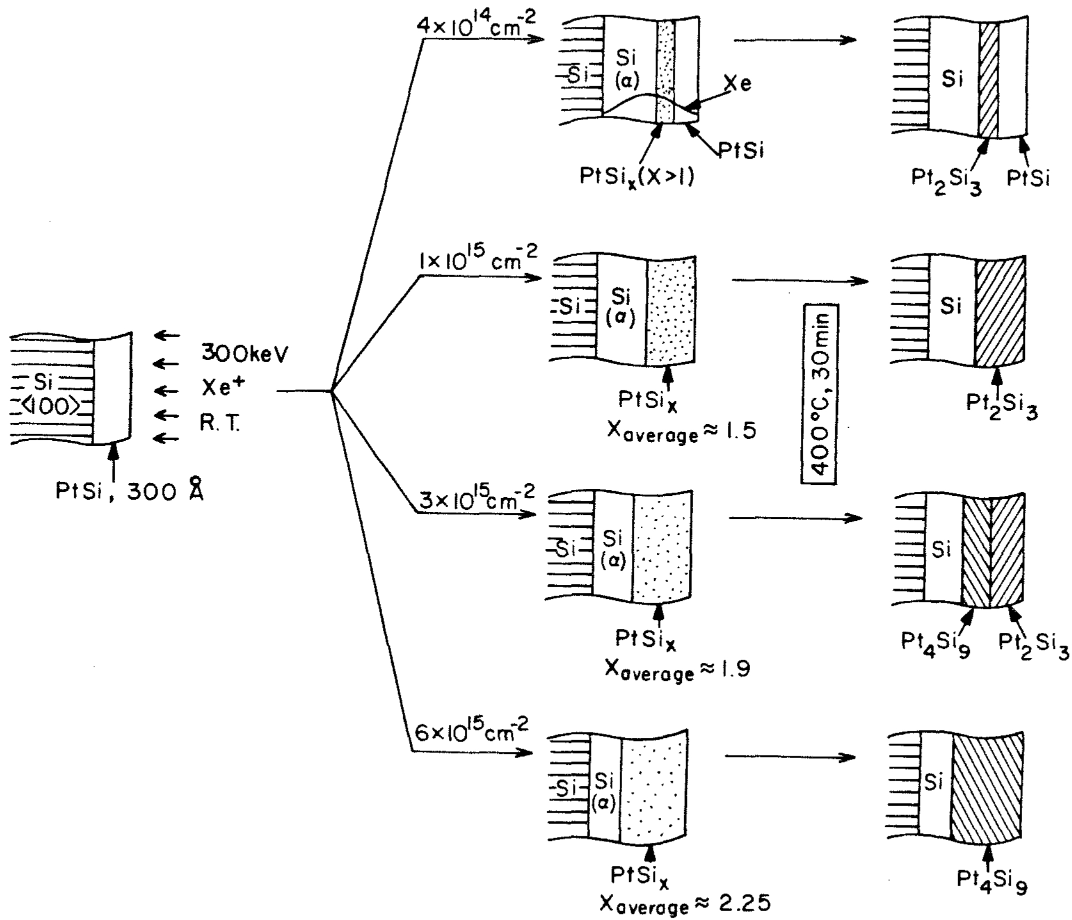

Fig. 3.4 Schematic diagram which shows the various Si-rich Pt-Si mixed layers produced by ion-beam mixing of a thin PtSi film on a Si substrate at different dose levels. Formation of the metastable phases Pt_2Si_3 and Pt_4Si_9 is achieved upon post-annealing.

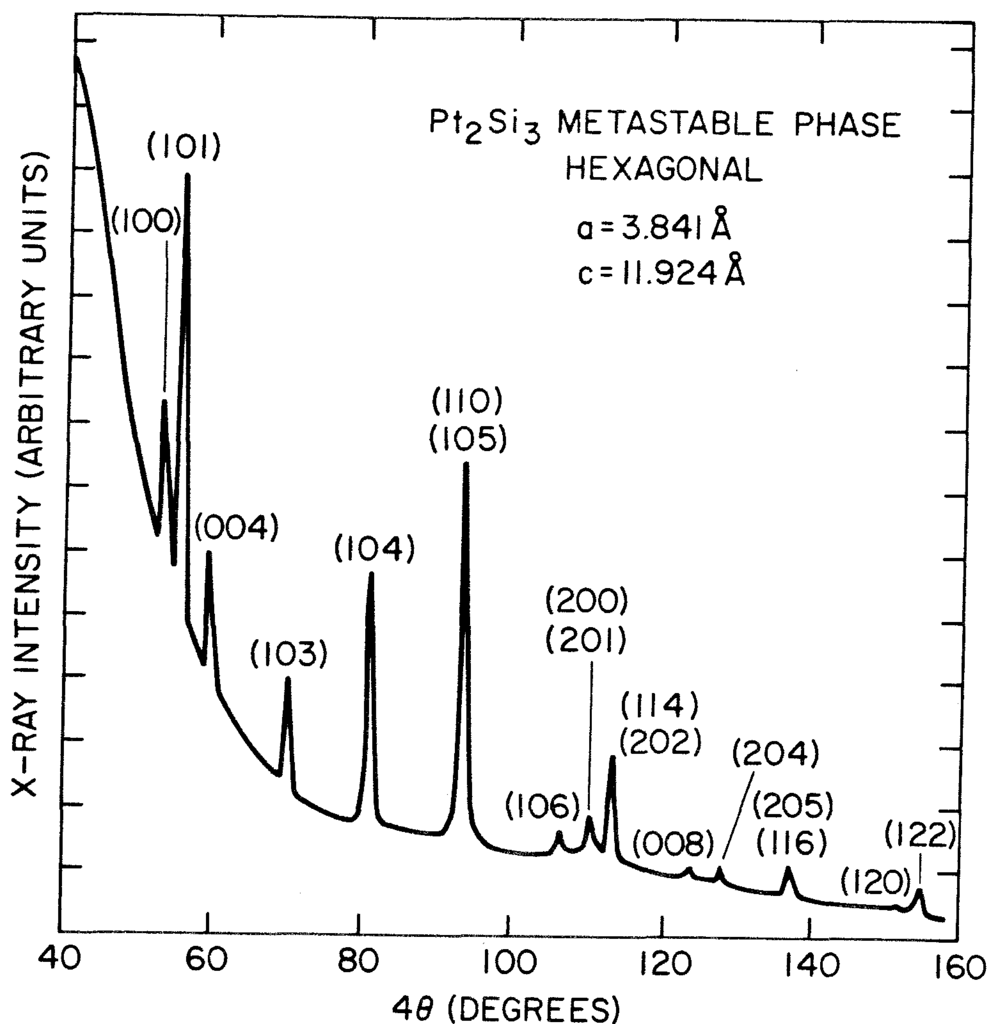

Fig. 3.5 Seemann-Bohlin x-ray diffraction spectrum for the metastable Pt_2Si_3 phase. The reflection peaks have been indexed on the base of a hexagonal unit cell with lattice parameters $a = 3.841 \pm 0.005$ Å, $c = 11.924 \pm 0.005$ Å.

only ~500 Å. This pattern has been compared to those of PtSi, Pt_2Si, Pt_3Si, Si and Pt as shown in Fig. 3.6 and no agreement with them was observed. Identification of crystal structure of Pt_2Si_3 was first performed by comparing the angular position of its diffraction lines with those of the seven crystal systems (Cubic, Tetragonal, Hexagonal, etc.). In some of the comparisons graphical methods [7] were used. The diffraction peaks can be very satisfactorily indexed on the base of a hexagonal unit cell with lattice parameters a=3.841±0.005 Å and c=11.924±0.005 Å; c/a = 3.104±0.005 (Fig. 3.5). Finally, positions of the atoms within the unit cell are deduced from the relative intensities of the diffraction lines and the forbidden reflections. Two possible atomic configurations have been attempted: (1) $D5_{13}(Ni_2Al_3)$ type with 5 atoms per unit cell, space group D_{3d}^3 - $c\bar{3}m$ [8], and (2) Pt_2Sn_3 type with 10 atoms per unit cell, space group D_{6h}^4 - P6/mmc [9]. The $D5_{13}$ type is a common structure for compounds such as Ni_2Al_3, Pt_2Al_3, Pt_2Ga_3, etc. The second structure is relatively uncommon and so far it has only been observed on an equilibrium compound Pt_2Si_3 and a ternary phase $Au_4In_3Sn_3$ [10]. The calculated and observed intensities for Pt_2Si_3 agreed surprisingly well with the latter structure (Pt_2Sn_3) as shown in Table III-I. This is not unexpected in view of the fact that Pt_2Si_3 has a c/a ratio of 3.104 which is very close to that of Pt_2Sn_3 (c/a = 2.991) but much greater than that of the $D5_{13}$ structure (c/a ≈ 1.2). The atomic coordinates within the unit cell determined from intensity calculation are:

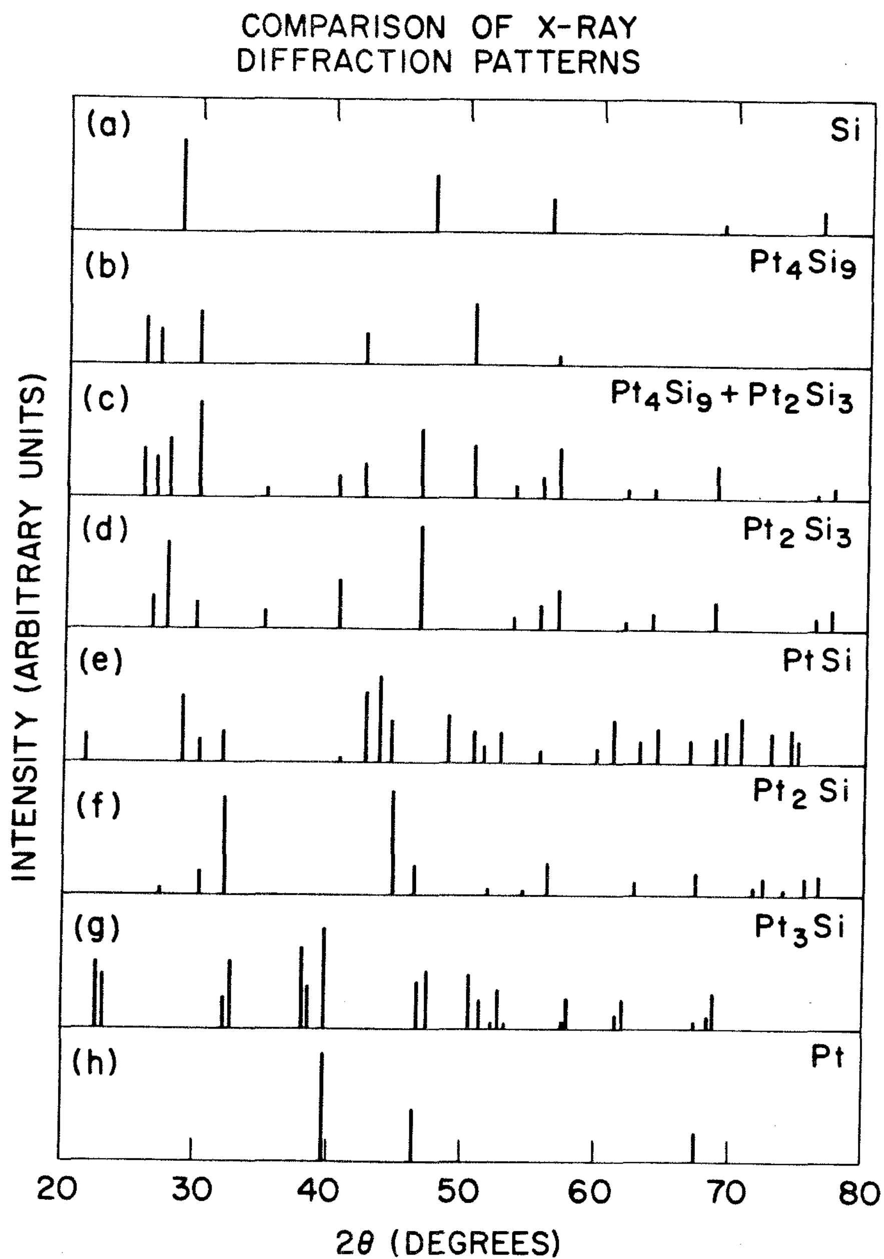

Fig. 3.6 Comparison of angular positions of x-ray reflections (CuKα) for elements Si and Pt, equilibrium compounds PtSi, Pt_2Si and Pt_3Si, and metastable phases Pt_2Si_3 and Pt_4Si_9.

TABLE III — 1

Lattice Spacings and Diffraction Peak Intensities for Pt_2Si_3

hkl	$d_{cal}^{(a)}$	d_{obs}	$I/I_{o\ obs}^{(b)}$	$I/I_{o\ cal}^{(c)}$
001	11.924	-	-	**
002	5.962	-	-	--
003	3.975	-	-	**
100	3.326	3.330	34	31
101	3.204	3.209	100	100
004	2.981	2.986	24	25
102	2.905	-	-	1
103	2.551	2.557	23	38
005	2.384	-	-	**
104	2.220	2.222	56	49
006	1.987	-	-	**
105	1.938	1.940*	83	20
110	1.921			61
111	1.896	-	-	**
112	1.828	-	-	--
113	1.729	-	-	**
106	1.706	1.710	3	5
007	1.703	-	-	**
200	1.663	1.653*	8	8
201	1.647			2
114	1.614	1.612*	23	21
202	1.602			4
203	1.534	-	-	--
107	1.516	-	-	--
115	1.496	-	-	**
008	1.491	1.491	2	2
204	1.452	1.455	4	6
116	1.381	1.366*	8	1
205	1.364			8
108	1.360	-	-	--
009	1.325	-	-	**
206	1.275	-	-	--
117	1.274	-	-	**
120	1.257	1.250*	2	1
121	1.250			2
109	1.231	1.233*	5	5
122	1.230			2
123	1.198	-	-	--
0010	1.192	-	-	--
207	1.190	-	-	--
118	1.177	1.180	2	1
124	1.158	1.160	1	2
1010	1.122	-	-	--
300	1.109	1.112	3	3

(a) Calculated from a=3.8406Å, c=11.9241Å, hexagonal structure.
(b) Experimental peak intensities, not integrated intensities, for a thin film (500A), not a powder sample with an infinite thickness.
(c) Calculated intensities for a powder pattern; structure factors are calculated by assuming a unit cell shown in Fig. 3.7.
* Two peaks overlapped.
** Forbidden reflections.
\- Not observed.
-- Not a forbidden peak but with a relative intensity smaller than 1.

4 Pt atoms: $\frac{1}{3}\frac{2}{3}z$; $\frac{2}{3}\frac{1}{3}\bar{z}$; $\frac{2}{3}\frac{1}{3}\frac{1}{2}+z$; $\frac{1}{3}\frac{2}{3}\frac{1}{2}-z$, Z_{Pt} = 0.125±0.005;

4 Si atoms: same as Pt with Z_{Si} = -0.060±0.005;

2 Si atoms: $00\frac{1}{4}$; $00\frac{3}{4}$

A three-dimensional hard sphere model for the unit cell is shown in Fig. 3.7. The atomic concentration of this structure is $6.565 \times 10^{22} cm^{-3}$ which is somewhat smaller than that of PtSi ($6.69 \times 10^{22} cm^{-3}$) [11] and greater than that of Si ($5.00 \times 10^{22} cm^{-3}$).

The thin film Pt_2Si_3 phase has also been analyzed using wide film Read camera to examine the texture structure or preferred orientation of the compound. Films produced by Xe bombardment were randomly oriented, while the samples implanted with Si ions were textured with <001> preferred orientation. It is known that the basal plane of a hexagonal structure has a low surface free energy and tends to orient preferentially parallel to the film surface. The presence of an impurity such as Xe may enhance the heterogeneous nucleation of randomly oriented nuclei and lead to a randomly oriented polycrystalline structure [12].

The x-ray diffraction spectrum for samples with the double layered (Fig. 3.3) structure is shown in Fig. 3.8. All the diffraction peaks can be identified to belong to either Pt_2Si_3 or Pt_4Si_9 as shown in Fig. 3.6. Identification of crystal structure for the compound with Pt_4Si_9 composition has not been attempted because of insufficient and rather diffused crystalline diffraction reflections in the x-ray data.

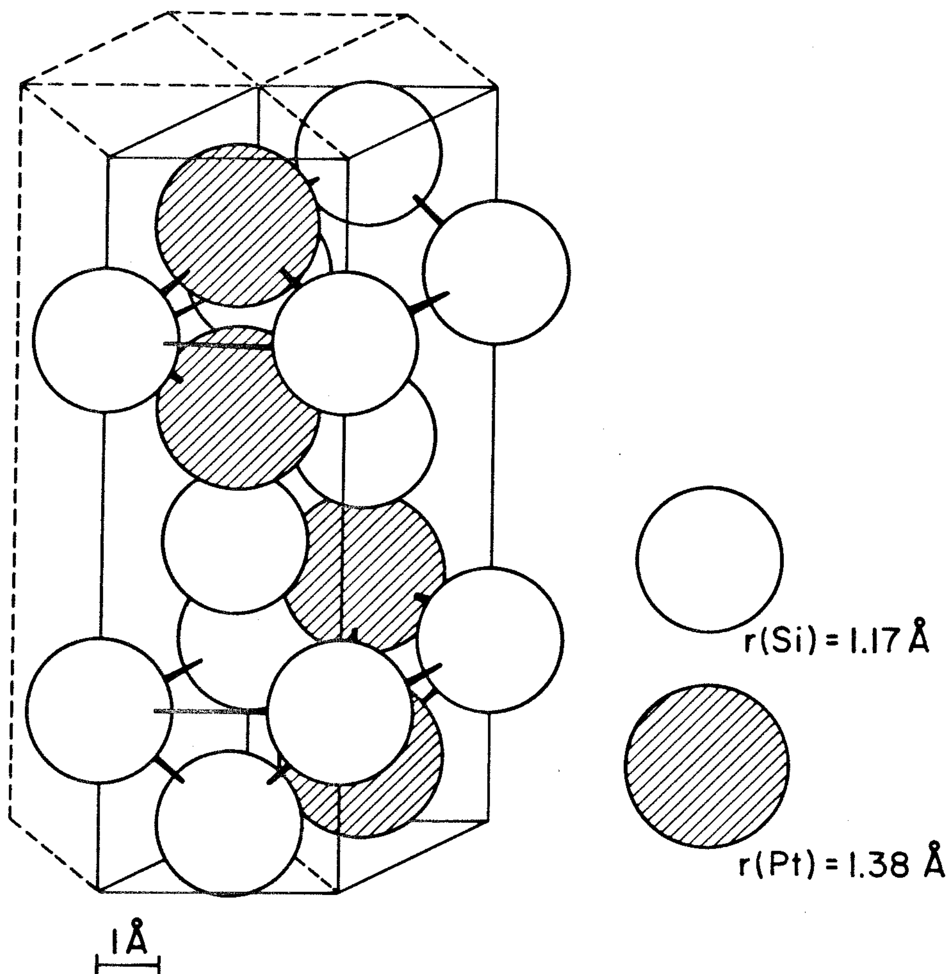

Fig. 3.7 Hard-sphere model for the unit cell of the metastable Pt_2Si_3 phase. The unit cell contains 10 atoms: 4 Pt and 6 Si atoms. Two Si atoms are on the edge and the other eight atoms lie along the central lines of the two trigonal prisms. The atomic coordinates within the unit cell are given in the text.

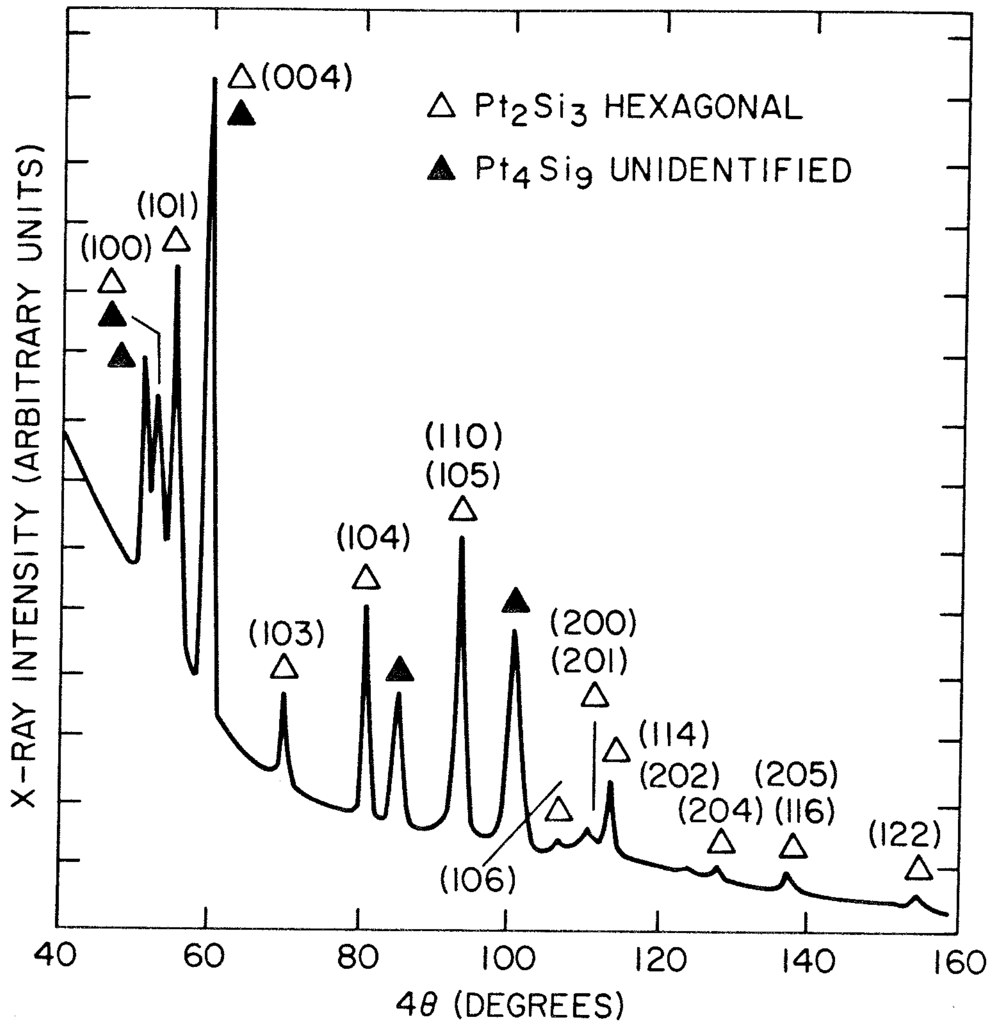

Fig. 3.8 X-ray diffraction spectra for a sample consisting of two metastable phases Pt_2Si_3 and Pt_4Si_9 (the sample with a back-scattering spectrum shown in Fig. 3.3). The structure of the Pt_4Si_9 phase has not been identified.

3.5 Properties of the Ion-Induced Pt_2Si_3 Phase

3.5.1 Metastability

The stability of the Pt_2Si_3 phase was studied by thermal treatment at evaluated temperatures (500-700^oC) and monitored by x-ray diffraction and ion backscattering. Fig. 3.9 shows the backscattering spectra of a Pt_2Si_3 film annealed at 550 and 600^oC, respectively for 20 min. The uniform layered structure was destroyed and x-ray analysis showed the presence of strong PtSi diffraction lines together with some residual lines belonging to the Pt_2Si_3 phase. The latter then disappeared completely for annealing temperatures above 600^oC and some polycrystalline Si diffraction lines were observed in addition to those of PtSi. Similar transformations have also been found at 500^oC for a longer annealing time ($\geq$ 2 hrs). These results suggest that the compound Pt_2Si_3 is metastable and tends to decompose into PtSi and Si at temperatures above 500^oC.

After decomposition the Pt distribution extends deeper into the Si substrate as shown by the tail of the Pt signals in the spectra (Fig. 3.9). The origin of such a deep penetration is not clear. One possible mechanism proposed here is that the effect may be due to crystallization of the amorphous Si layer underneath the Pt_2Si_3 film (as mentioned in Section 3.3). The amorphous Si transferred into a polycrystalline phase at temperature around 550^oC, which would result in a fast interdiffusion of Pt or PtSi along the Si grain boundaries and give rise to a nonuniform structure as shown in the inset of Fig. 3.9. The phenomenon of fast interdiffusion between a metal layer and an

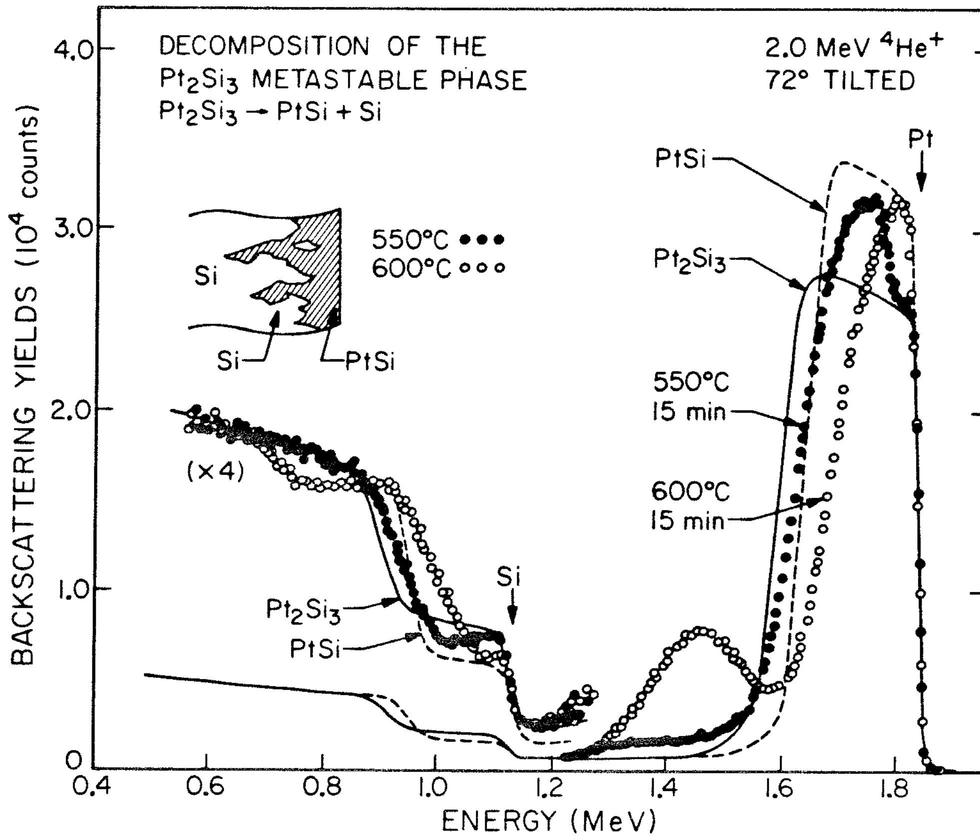

Figure 3.9 Backscattering spectra which demonstrate the decomposition of the metastable Pt_2Si_3 phase: Pt_2Si_3; → PtSi+Si. After decomposition, the Pt distribution extends deeper into the Si substrate and the interface becomes nonuniform.

amorphous Si layer at temperatures of 500 - 600°C has been observed in many systems [(13)] and is attributed to the crystallization of the amorphous Si.

3.5.2 Superconductivity

Low temperature resistivity measurements have been performed between 1.5K and 10K using standard four-probe techniques. The ion-

induced amorphous layer exhibited a nearly constant resistivity of the order of 350 μΩ-cm. However, a superconducting transition onset at about 4.2K was observed for the crystalline Pt_2Si_3 phase as shown in Fig. 3.10. A complete transition to superconductivity has been achieved at temperature below 3.6K. The T_c measurements have been repeated on several samples and the sharp transition behavior is quite reproducible.

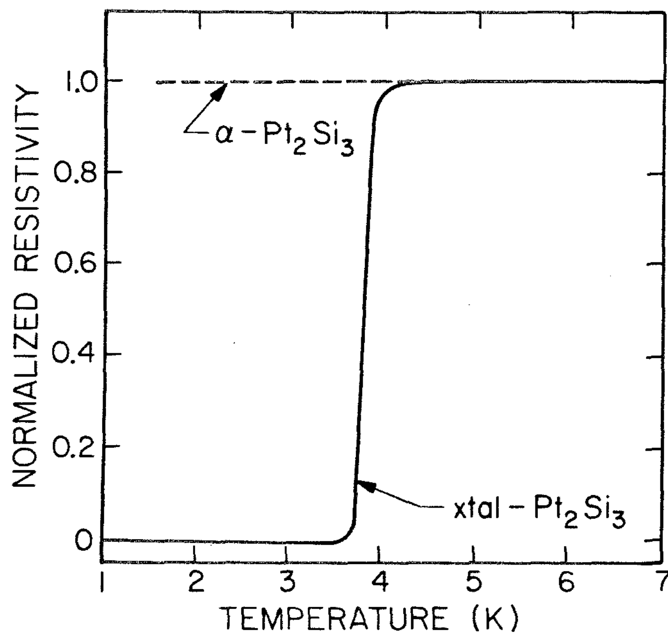

Figure 3.10 Superconducting transition temperature measurements for the ion-induced amorphous Pt-Si alloy and the crystalline metastable Pt_2Si_3 phase. The amorphous alloy is nonsuperconducting at temperature down to 1.5K, while the crystalline phase exhibits a superconductive transition at about 4K.

It is known that, for compound superconductors, the transition temperature T_c is strongly influenced by the crystal structure of the compound [14]. According to a recent survey of superconductive materials collected by Roberts [15], we found that this is the first time that a compound of this structure has been observed to be a superconductor. Moreover, the fact that both Pt and Si are nonsuperconductive elements but a relatively high T_c (∿4k) observed for Pt_2Si_3 suggests that the structure of Pt_2Si_3 is interesting from the viewpoint of investigations of high transition temperature superconductors.

3.6 Co-deposited Amorphous $Pt_{40}Si_{60}$ Films

Experiments using co-deposited Pt-Si films have been performed in an attempt to produce the metastable Pt_2Si_3 phase without using ion-beams. The results of such an experiment are summarized schematically in Fig. 3.11. Thin film $Pt_{40}Si_{60}$ alloys were prepared by simultaneous evaporation of Pt and Si onto single crystal Si substrates which were cooled down to LN_2 temperature during the deposition. X-ray diffraction measurement showed that the as-deposited films (after warming up to R.T.) were amorphous. Annealing of those samples directly at 400-500°C resulted in the formation of a mixture of PtSi and Pt_2Si_3. Faint traces of crystalline Si reflections were also detected in x-ray diffraction measurements. However, a homogeneous Pt_2Si_3 phase has been obtained by annealing a co-deposited sample after being bombarded with ions (Xe^+ or Si^+) to certain doses. In this case, the ion energy was adjusted so that the projected range was about half of the film thickness and the Si substrate remained roughly undisturbed. At higher temperatures

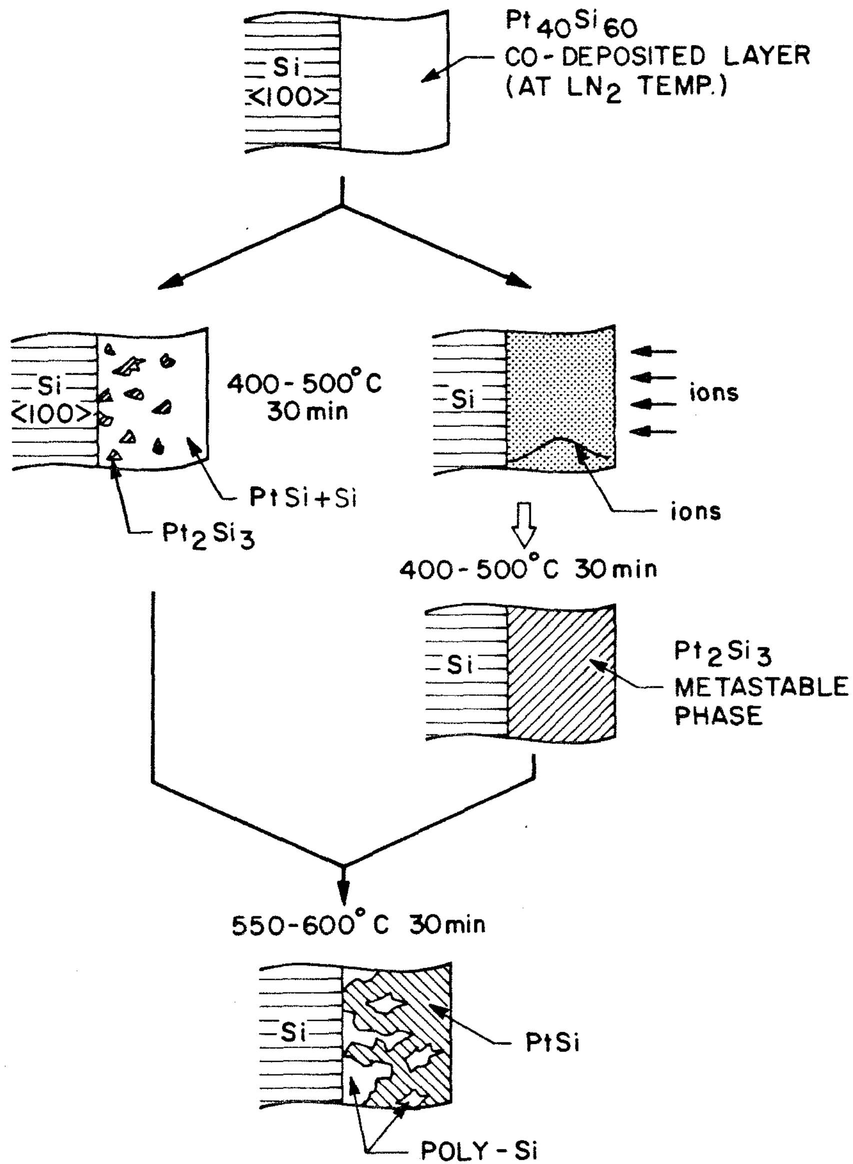

Fig. 3.11 Schematic picture which summarizes the experiments using co-deposited amorphous $Pt_{40}Si_{60}$ films. Homogeneous Pt_2Si_3 phase can only be obtained by annealing an ion-bombarded film.

(500-600°C) the layer again transformed into a mixture of PtSi and Si. In contrast to the results shown in Fig. 3.9, the interface between the PtSi layer and the Si substrate remained uniform since no amorphous layer was produced in the crystalline Si substrate in this case.

Superconducting T_c measurements of samples consisting of mixed phases of PtSi and Pt_2Si_3 have also been performed. The resistivity started to decrease at temperature about 4.2K but much less abruptly than that observed for the pure Pt_3Si_3 phase.

3.7 Discussions

Figure 3.12 summarizes schematically the formation of the metastable Pt_2Si_3 phase by using ion-beam-mixing techniques. Starting with a thin layer of PtSi on a single crystal Si substrate, ion-bombardments with energetic Xe or Si ions through the interface were first performed to induce intermixing between PtSi and Si. A Si-rich Pt-Si mixture was formed after the bombardment along with an amorphous Si layer underneath the mixture due to the bombardment damage. Subsequent thermal annealing at 400-500°C resulted in the formation of a well defined metastable phase with a stoichiometry of Pt_2Si_3 and a hexagonal crystal structure. Some Si crystallites might be present in the amorphous Si layer after the annealing but the amount was very small. At higher temperatures (550-600°C) the Pt_2Si_3 phase decomposed into a mixture of PtSi and Si along with a complete crystallization of the amorphous Si layer. The interface between PtSi and Si became nonuniform and a deep penetration of Pt (or PtSi) into the Si substrate was observed.

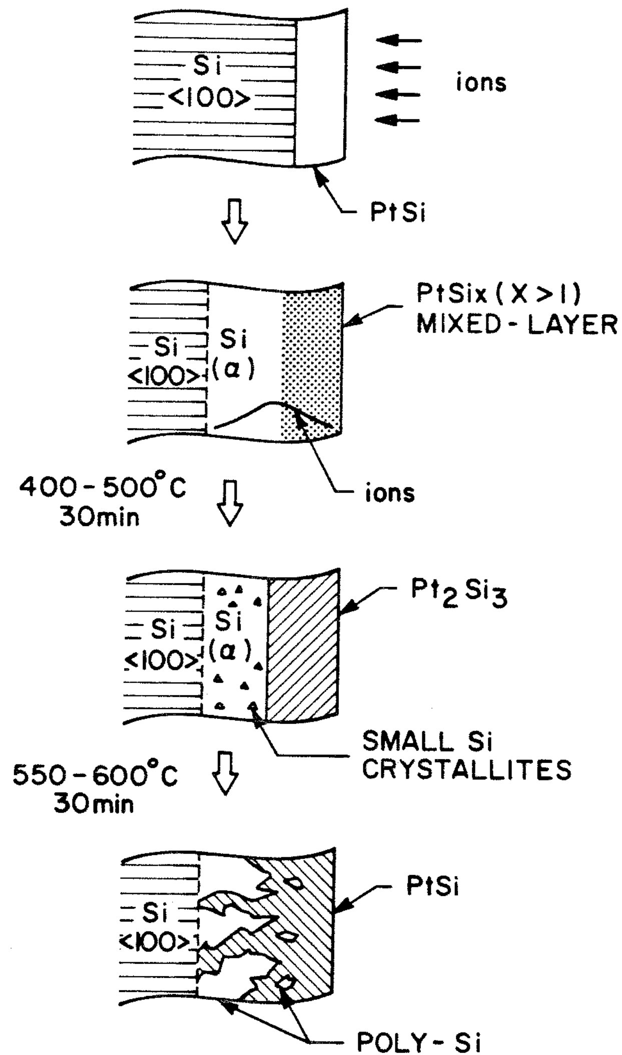

Fig. 3.12 Schematic picture which shows the formation of the metastable Pt_2Si_3 phase by ion-beam mixing and post-annealing, and the decomposition of this phase at higher temperature.

The existing equilibrium Pt-Si phase diagram is shown in Fig. 3.13 which does not indicate the presence of the metastable Pt_2Si_3 phase. Recently, Schubert and his co-workers [16] have reinvestigated the Pt-rich side of the diagram and reported several new stable compounds, yet the Si-rich side shown in the phase diagram (Hansen [1]) has not been modified. From the result of decomposition the existence of the Pt_2Si_3 phase can be regarded as metastable. However, the central question is, under what conditions can this metastable phase be formed, or what are the requisites for its formation.

Although the results shown in the schematic summaries of Fig. 3.11 and Fig. 3.12 indicate that formation of metastable phase seems to require ion bombardment, the effects of ion-beams on the metastable phase formation are not readily visualized. On the other hand, the result that the metastable phase can still be formed by annealing a co-deposited layer directly but with the presence of the equilibrium PtSi phase raises another question about the differences between a co-deposited amorphous layer and an ion-induced layer.

The compositional uniformity of the co-deposited $Pt_{40}Si_{60}$ films determined by backscattering measurement is with ±10% over the layer thickness. However, composition variation may be present in microscopic scale (10-50Å) which cannot be detected by backscattering techniques. If the composition in a local region of the layer is close to PtSi, nucleation and growth of the PtSi phase may occur during the annealing. It will presumably compete with the nucleation and growth of the metastable Pt_2Si_3 phase. Another possibility for the formation of PtSi is that the

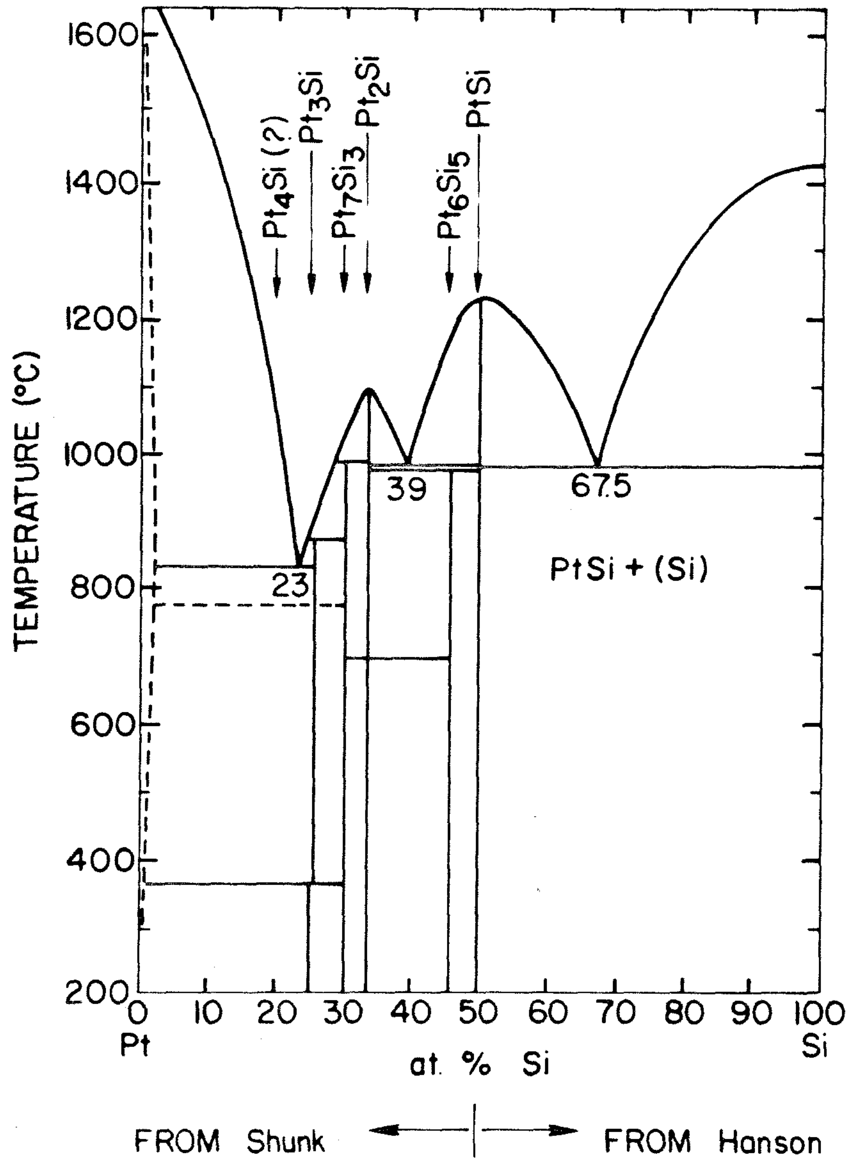

Fig. 3.13 Equilibrium Pt-Si phase diagram. The Pt-rich side has recently been modified (Ref. 16).but the Si-rich side remains unchanged.(Ref. 1).

co-deposited $Pt_{40}Si_{60}$ films may already contain PtSi microcrystallites in the as-deposited state, which will then favor its growth. In both

cases, the effects due to composition variation and presence of micro-crystallites can be eliminated by ion beam because of the so-called "mixing" effect.

It is known that formations of metastable phases are usually associated with transformation from an amorphous state [12]. Metastable phase can be achieved not only because crystalline structure is more stable than the amorphous structure (by the enthalpy difference), but because the kinetics for transformation from the amorphous to the metastable crystalline phase may be more rapid than for the transformation to the equilibrium structure. This amorphous to metastable crystalline transformation has, indeed, been observed in many binary systems. For example, supersaturated Ag-Cu solid solutions have been obtained by thermal annealing of amorphous Ag-Cu alloys produced by vapor depositions [17]. Similar transformation was found in other simple eutectic systems such as Au-Si, Au-Ge, etc., where nonequilibrium intermediate phases with well-defined crystalline structures have been produced[18,19]. Based on the experimental results observed for the ion-mixed and co-deposited layers, we suggest that the amorphous to metastable transformation may be required to form the metastable Pt_2Si_3 phase and, moreover, a composition sufficiently close to the stoichiometry of the compound seems also indispensable.

Finally, it is desirable to discuss the observation of transformation of ion-induced mixed layers into two phases of well-defined layered structure shown in Fig. 3.2 and Fig. 3.3. The results of ion bombardment is to induce intermixing between PtSi and Si such that an amorphous

layer enriched in Si is formed. The composition of this mixed layer varies in depth and is more Si-rich near the interfacial region as shown in Fig. 3.3. Since thermal annealing can initiate phase transformation from the amorphous to a metastable crystalline state, the resulting phases will be such that a minimum redistribution of atoms within the mixed layer has been required [20]. In other words, nucleation and growth of the phases will take place presumably near the regions where the local composition is close to the stoichiometry of a particular compound. Consequently, the presence of two phases (PtSi and Pt_2Si_3 in Fig. 3.2, Pt_2Si_3 and Pt_4Si_9 in Fig. 3.3) is possible due to the variation of the composition over the layer thickness. On the other hand, formation of the Pt_4Si_9 phase will be favored with increasing ion doses since the layer becomes progressively more Si-rich due to the mixing effect as shown in Fig. 3.3.

3.8 Conclusion

In conclusion, we summarize our important findings on ion-induced metastable Pt_2Si_3 phase as follows:

(1) By using ion bombardment, amorphous Pt-Si alloys rich in Si have been obtained as a result of ion-induced atomic mixing between a thin PtSi film and a Si substrate. Formation of a metastable phase with a stoichiometry Pt_2Si_3 was observed upon post annealing at 400-500°C. The phase does not exist in the equilibrium phase diagram and has not been reported before.

(2) The crystal structure of Pt_2Si_3 has been identified to be hexagonal with lattice parameters a = 3.841 Å and C = 11.924 Å. Intensity calculations showed that the structure was isomorphous to that of Pt_2Sn_3 and there are 10 atoms per unit cell.

(3) The metastable Pt_2Si_3 was found to exhibit a superconducting transition onset at about 4.2 K and became completely superconductive at temperatures below 3.6K. For the first time, a compound of this structure is observed to be a superconductor.

(4) Based on the experimental results observed for the ion-mixed and co-deposited alloys, we suggest that an amorphous to crystalline transformation may be required to form the metastable Pt_2Si_3 phase and moreover, a composition sufficiently close to the stoichiometry of the compound seems also necessary.

The present results strongly suggest that the technique of implanting through an "equilibrium interface" and the associated atomic mixing may promise to be a new method of producing unusual metastable phases, whose physical properties could be of significant interest.

References

1. P. Hansen, Constitution of Binary Alloys, page 1140.

2. See for example, K. N. Tu and J. W. Mayer in "Thin Films - Interdiffusions and Reactions", J. M. Poate, K. N. Tu and J. W. Mayer, Eds., (Wiley, New York, 1978). Chap. 10.

3. A. K. Shinha, R. B. Marcus, T. T. Sheng and S. E. Haszko, J. Appl. Phys. 43, 3637 (1972).

4. B. Y. Tsaur, Z. L. Lian and J. W. Mayer, Appl. Phys. Lett. 34 168 (1979).

5. B. Y. Tsaur, Electrochemical Society Meeting, Oct. 1979, Los Angeles, paper to be published in the Proceedings of Thin Film Symposium.

6. K. N. Tu and B. S. Berry, J. Appl. Phys. 43, 3283 (1972).

7. B. D. Cullity, Elements of X-Ray Diffraction, (Addison-Wesley Publishing Co., 1967), Chap. 10.

8. A. J. Bradley and A. Taylor, Philos. Mag. S.7, 23, 1049 (1937).

9. K. Schubert and H. Pfisterer, Z. Metallkunde, 40, 146 (1959).

10. K. Schubert, H. Breimer and R. Gohle, Z. Metallkunde 50, 146 (1959).

11. H. J. Goldschmidt, Interstitial Alloys (Plenum Press, New York, 1967), Chap. 7.

12. J. W. Christian, The Theory of Transformation in Metal and Alloys (Pergamon Press, Oxford, 1965).

13. K. Nakamura, M. A. Nicolet, J. W. Mayer, R. J. Blattner, C. A. Evans, Jr., J. Appl. Phys. 46, 4678 (1975).

14. B. T.Matthias, T. H. Geballe and V. B. Compton, Rev. Modern Physics 35, 1 (1963).

15. B. W. Roberts, Survey of Superconductive Materials and Critical Evaluation of Selected Properties, J. Phys. Chem. Ref. Data, Vol. 5, No. 3 (1976).

16. R. Gohle and K. Schubert, Z. Metallkunde 55, 503 (1964).

17. S. Mader, A. S. Nowick and H. Widmer, Acta Metall 15, 203 (1967).

18. T. R. Anantharaman, H. L. Luo and W. Klement, Jr., Nature 210, 1040 (1966).

19. P. Predecki, B. C. Giessen and N. J. Grant, Trans. AIME 233, 1438 (1965).

20. Phase Transformations, H. J. Aaronson ed. American Society for Metals, October 1968.

Chapter 4

ION-BEAM-INDUCED METASTABLE Pt_2Si_3 PHASE - KINETICS AND MORPHOLOGY

4.1 Introduction

The previous chapter has dealt with the occurrence of the metastable Pt_2Si_3 phase in the ion-induced amorphous Pt-Si alloys, and with the crystalline structure of the phase and its properties (metastability and superconducting transition behavior). Of special interest is the formation of amorphous Pt_2Si_3 alloys by ion-beam-mixing and the transformation of this structure in two stages of annealing. In the first of these stages the amorphous phase transformed into a metastable crystalline Pt_2Si_3 phase, while in the second stage the equilibrium two-phase structure of PtSi and Si was formed (Fig. 3.12 of Chapter 3).

The kinetics of amorphous to crystalline transformation for bulk alloys such as these produced by splat-cooling techniques [(1)] have, in the past, been extensively studied by use of calorimetry [(2)] and resistivity measurements [(3)]. For thin film alloys , the calorimetrical measurement is difficult due to the limited amount of materials but the resistivity measurement has been shown to be convenient and exhibited good sensitivity. For examples, Mader and Nowick [(4)] have studied the crystallization kinetics of vapor-deposited amorphous Cu-Ag and Co-Au thin film alloys by using resisitivity measurement upon isothermal and constant heating-rate annealings. The results were analyzed in terms of a classical model for nucleation and growth transformation. More recently, resisitivity measurements have been utilized to study the structural relaxation phenomenon in amorphous alloys [(5)].

In this chapter, the transformation behavior of the ion-induced amorphous Pt_2Si_3 alloys and the structure of the alloys at various stages of transformation studied by a combination of resisitivity measurements and transmission electron microscopy and diffraction will be described in detail. The kinetics of amorphous to crystalline transformation has been determined by isothermal treatment in the temperature interval 376-392°C. The attempt of this work is to utilize classical kinetics analysis for the study of annealing process (or transformation behavior) in amorphous thin films.

4.2 Sample Preparations and Analytical Techniques

Amorphous Pt_2Si_3 alloys were prepared by simultaneous evaporation (so-called the vapor quenching method [6]) of the two components in a double e-gun evaporation system. The deposition rate of each of the components was controlled individually by a system with a thickness monitor and feedback control unit to adjust the gun power and hence the evaporated vapor flux. The films were deposited on substrate clamped onto a copper block which was cooled down to ~80K by liquid nitrogen cooling. Two types of substrates have been used: (1) sapphire (Al_2O_3) substrates for resisitivity measurement because of good adhesion of the evaporated film at high temperatures, and (2) Si substrates for transmission electron microscopic study due to easy preparation of thin foils. Typical deposition rates were from 5 to 10 Å/sec measured at a distance of about 50 cm above the source where the samples were mounted. The back-

ground pressure was maintained at or below $8x10^{-7}$ Torr during the deposition.

The compositions and thicknesses of the deposited films were measured by backscattering techniques with 2.0 MeV ^4He ions at glancing incidence ($70-80^o$). The average composition of the alloys was measured to be Pt_2Si_3 but with a $\sim$10% variation of composition in depth over the layer thickness. The depth resolution of backscattering techniques at glancing incidence (76°) was about 50 Å so that composition fluctuation in scale less that 50 Å cannot be detected. The thickness of the deposited films was in the range of 500-800 Å.

Some of the samples were bombarded with 250 keV Xe^+ to a dose of $1x10^{15}cm^{-2}$ or 150 keV Si^+ to a dose of $3x10^{15}cm^{-2}$. The projected range of ions was about half of the total film thickness. The peak concentration of the implanted species was estimated to be less than 1 at.%. Backscattering measurements indicated that the composition of the alloyed layer was quite uniform after ion bombardment and no significant intermixing was found between the Al_2O_3 substrates and the Pt-Si layers.

The resistivity of the alloys upon annealing was measured in situ using standard four-probe technique in a furnace with purified flowing He gas. The samples were placed on a quartz holder with four molybdenum electrical leads pressed gently on the film surface. The specimen was connected in series with a constant current source of 100 μA and the potential drop was recorded between the two central electrodes. The resistivity value was then determined from the resistance of the films and their dimensions. The absolute error of resistivity

measurement is estimated to be less than 5%. The temperature was monitored simultaneously with the resistance by means of a platinum-rhodium thermocouple which was placed adjacent to the specimen. The measurements have been performed at constant rate of heating of approximately 2-3°C/min (isochronal annealing) or at constant temperatures (isothermal annealing).

The structures of the alloys were examined using glancing incidence x-ray diffraction and transmission electron microscopy and diffraction. Samples for TEM studies were given the desired annealing treatment in the flowing He gas furnace. They were then sectioned into disks of 3.0 mm in diameter and jet-etched from the back (i.e., from the Si substrate) using a solution of $HF:HNO_3 \simeq 1:4$ until a thin section approximately 300-500 Å was obtained. The samples were examined in an AEI-802 electron microscope operated at 80 keV using bright and dark electron microscopy and scanning electron diffraction. The microscope is fitted with an attachment for scanning, velocity analysis and direct measurement of the diffracted electron intensity. The experimental procedure as well as the electron optical description of the attachment can be found in reference 7.

4.3 Results

4.3.1 Resistivity Measurements

As mentioned in Section 3.6 of Chapter 3 (Fig. 3.11), direct annealing of a co-deposited $Pt_{40}Si_{60}$ film resulted in the formation of a mixture of Pt_2Si_3, PtSi and Si. However, a homogeneous Pt_2Si_3 phase

can be obtained by annealing a co-deposited film after being bombarded with ions to certain doses. The effect of ion bombardment is to induce "atomic mixing" such that composition variation within the layer can be eliminated and an atomically uniform Pt_2Si_3 layer is formed. We found that selection of bombarding ion species was arbitrary to achieve the mixing and no differences in the results were observed by using inert gas ions (Xe^+) or self-ion Si^+ (Section 3.3 of Chapter 3). In this section, we first give a detailed description of annealing behavior of electrical resistivities of co-deposited $Pt_{40}Si_{60}$ films with and without ion bombardment. Since resistivity is dependent on the structure state of the material, we shall find it useful as an indication of the state of an alloy. The correlation of the resistivity with the film structure as seen by transmission electron microscopy and diffraction will be given in the next section (Section 4.3.2).

The resistivity of an as-deposited alloy was quite high, in the range of 360-380 $\mu\Omega$-cm. After ion bombardment, the change of resistivity was found to be less than 2% (which is within our experimental error) and hence was negligible. In Fig. 4.1, a typical resistivity annealing curve of a co-deposited, ion-mixed Pt_2Si_3 alloy is shown during heating with a constant rate of temperature rise of about 2-3°C/min. The resistivity has been normalized to the room temperature value. In the early stage of annealing (25-100°C), there is a slight decrease (about 4%) in resistivity, the resistivity then increases gradually upon annealing between 100 and 350°C, with a small temperature coefficient of the order of $1\times10^{-4}/^\circ$C. At temperatures near 350°C a small increase of

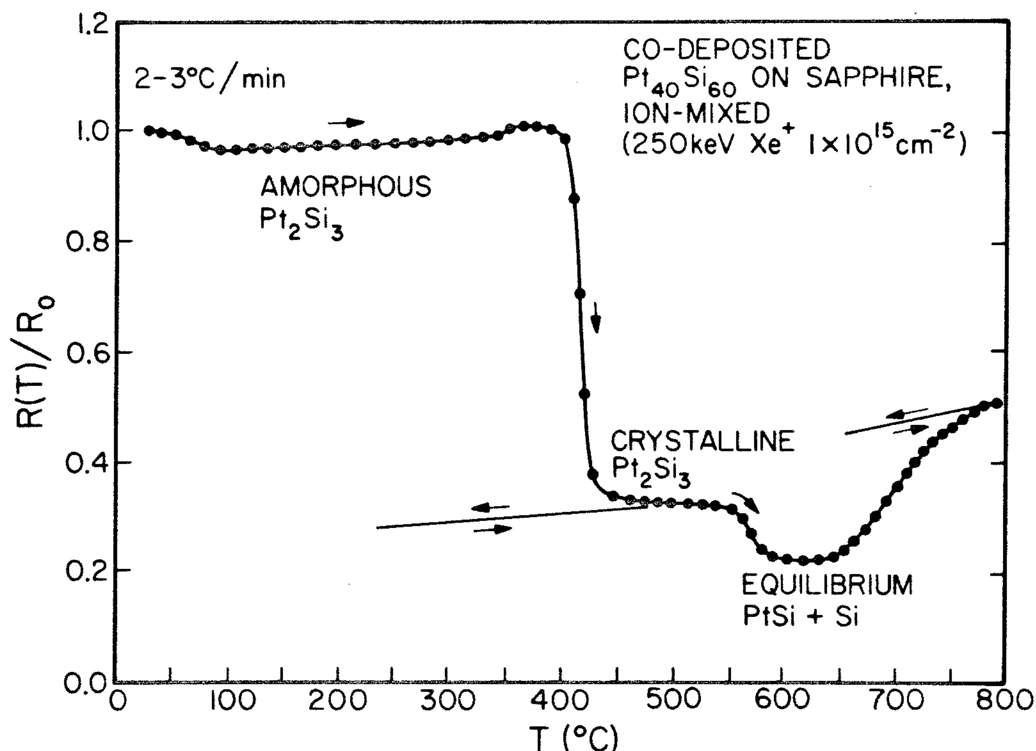

Fig. 4.1. Resistivity annealing curve for the co-deposited, ion-mixed amorphous Pt_2Si_3 alloy upon heating at about 2-3^{0}C/min. Two distinct stages of transformation: (i) from the amorphous to a metastable crystalline and (ii) from the metastable crystalline to the equilibrium two-phase structure, are observed as revealed by a rapid change of resistivity at temperatures around 400 and 550^{0}C, respectively.

resistivity appears and the resisitivity drops at about 400^{0}C in a precipitous annealing step. X-ray and electron diffraction measurements showed that before this annealing step the structure was amorphous; afterwards it was found to be a single metastable phase Pt_2Si_3. After crystallization, a reversible behavior of resistivity is observed, with

a positive temperature coefficient of $\sim 3\times10^{-4}/^{o}C$.

Upon further heating, the resisitivity maintains roughly a constant value until a second annealing stage occurs which appears as a somewhat broader transition near $550^{o}C$. This corresponds to the transformation of the metastable Pt_2Si_3 phase into the equilibrium two-phase (PtSi and Si) structure as indicated by x-ray and electron diffraction measurements. At higher temperatures ($>650^{o}C$) the resisitivity increases rapidly and levels off near $800^{o}C$. A reversible cooling curve is obtained with a positive temperature coefficient of $\sim 1.2\times10^{-3}/^{o}C$. Examination of the film surface (after being cooled down to room temperature) with SEM showed large Si precipitates(of $\sim$5-10 μm in size) which are formed during the annealing. This may cause the large increase in resistivity.

The annealing curve for a co-deposited $Pt_{40}Si_{60}$ alloy film (without ion bombardment) is shown in Fig. 4.2. The resisitivity decreases gradually in contrast to the slight increase of resisitivity for the ion-mixed samples shown in Fig. 4.1. This continuous annealing behavior extends up to about $310^{o}C$, where the annealing rate accelerates and a definite step develops showing a maximum annealing rate at about $350^{o}C$. After completion of this annealing step, the resisitivity decreases slowly upon further annealing. The annealing curve at temperatures above $600^{o}C$ is almost the same as that shown in Fig. 4.1. X-ray and electron diffraction analysis showed the presence of weak crystalline diffractions corresponding to PtSi superimposed to the amorphous background for films annealed up to $300^{o}C$. After a rapid annealing near $350^{o}C$, a mixed phase consisting of Pt_2Si_3, PtSi and Si was found.

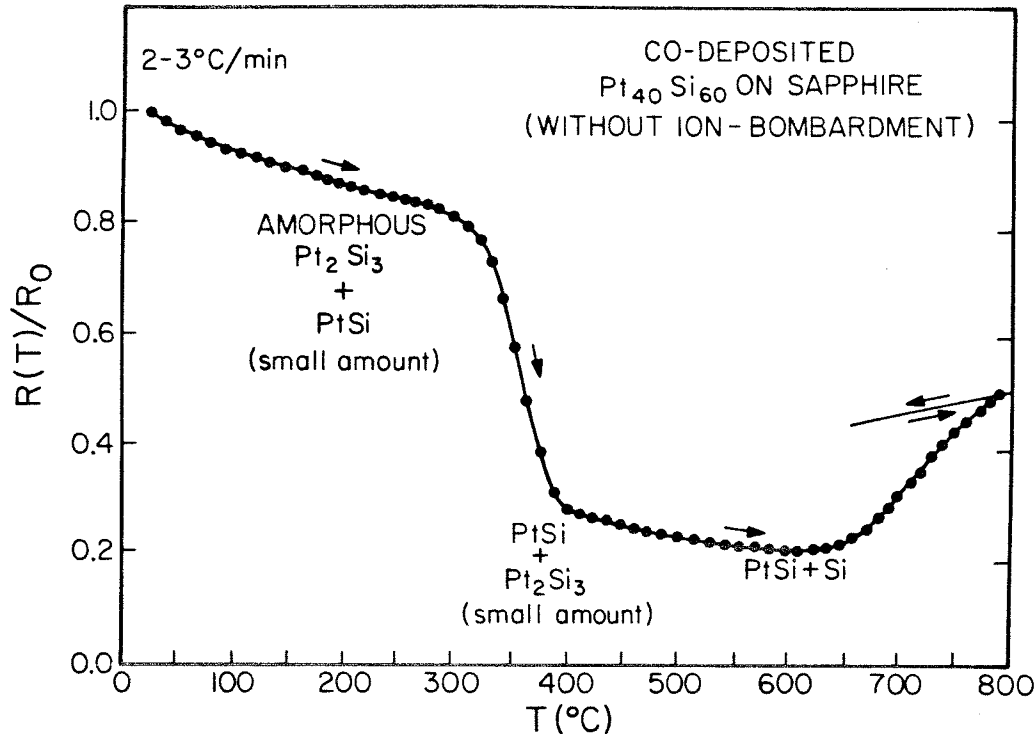

Fig. 4.2. Resistivity annealing curve for the co-deposited Pt_2Si_3 alloy (without ion-bombardment) upon heating at about 2-3^oC/ min. Equilibrium PtSi phase was observed at temperatures below 300^oC.

The Pt_2Si_3 phase disappeared at temperatures above 550^oC along with the appearance of strong polycrystalline Si diffractions in addition to those of PtSi. A similar reversible cooling curve of resistivity is observed after annealing up to high temperature.

Isothermal annealings for the co-deposited, ion-mixed $Pt_{40}Si_{60}$ alloy films were performed over the temperature interval 376-392^oC to study the kinetics of amorphous to crystalline transformation. A set of such annealing curves are shown in Fig. 4.3. All the curves exhibit a

similar shape; the resistivity decreases in the beginning (inset of Fig. 4.3), reaching a maximum shortly and then gradually falls as crystallization proceeds. This behavior, similar to that observed in the isochronal annealing between R.T. and 400°C (Fig. 4.1), is believed

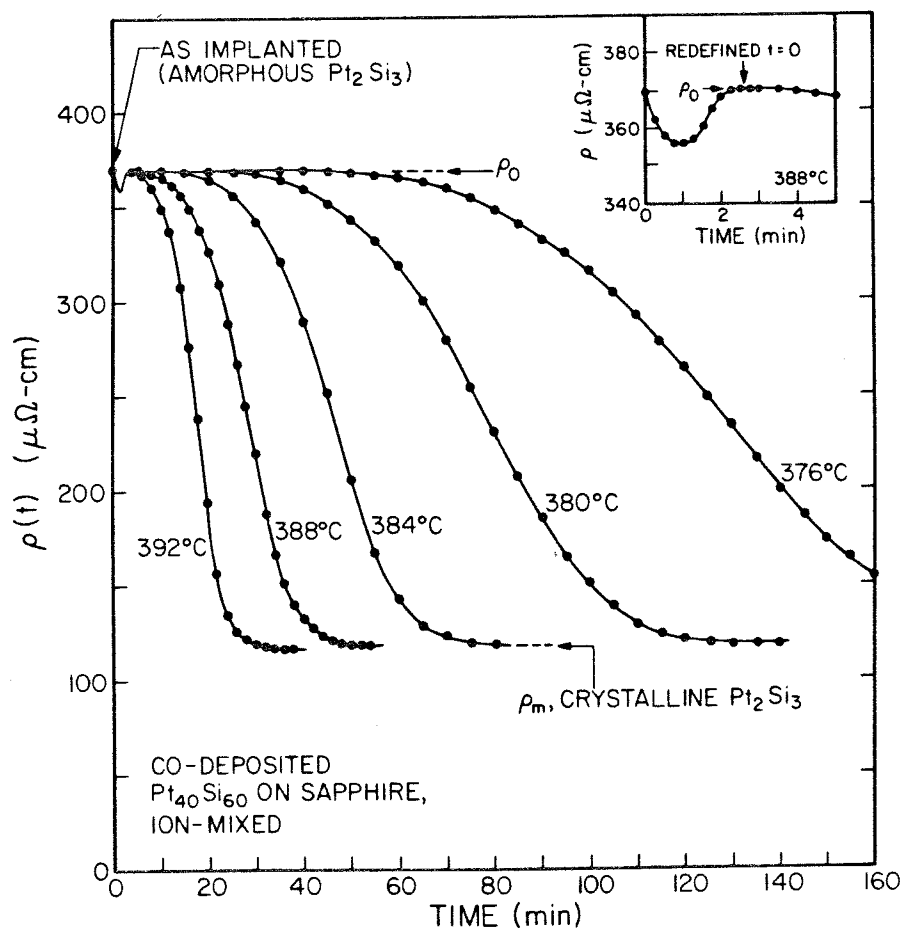

Fig. 4.3. Isothermal annealing curves of the co-deposited, ion-mixed Pt_2Si_3 alloy in the temperature interval 376-392°C. The curves exhibit an initial transient shown in the inset (see text).

due to a transient phenomenon in the isothermal annealing. Generally, a time delay (2-5 min) was present before the sample reached the furnace temperature due to the finite thermal mass of the specimen holder. Consequently, this initial annealing behavior simply represents the annealing between R.T. and the isothermal annealing temperature but at a very fast rate of temperature rise (∿100-150°C/min).

4.3.2 Microstructure

We now turn to a more detailed discussion of the structure of the Pt-Si alloys in their various states, as determined by transmission electron microscopy and diffraction. Fig. 4.4 shows typical electron micrographs (bright field) and diffraction pictures of co-deposited, ion-mixed Pt_2Si_3 alloy films. The diffraction pattern for the as implanted film (Fig. 4.4a) reveals a series of diffused halos, indicating an amorphous-like structure. The first intense halo has a high angle shoulder and the second halo splits into two low-intensity peaks. Bright field image shows some density fluctuations in the material. Dark field techniques revealed a similar density fluctuation and the absence of micro crystallites at the resolution of approximately 10-12 Å.

Fig. 4.4b shows the same film in the metastable crystalline state after passing through the first annealing stage (450°C, 30 min). Crystalline diffraction lines and arcing dots (due to the large crystals) can be seen in the diffraction pattern which has been identified to belong to the metastable Pt_2Si_3 phase. The micrograph shows average

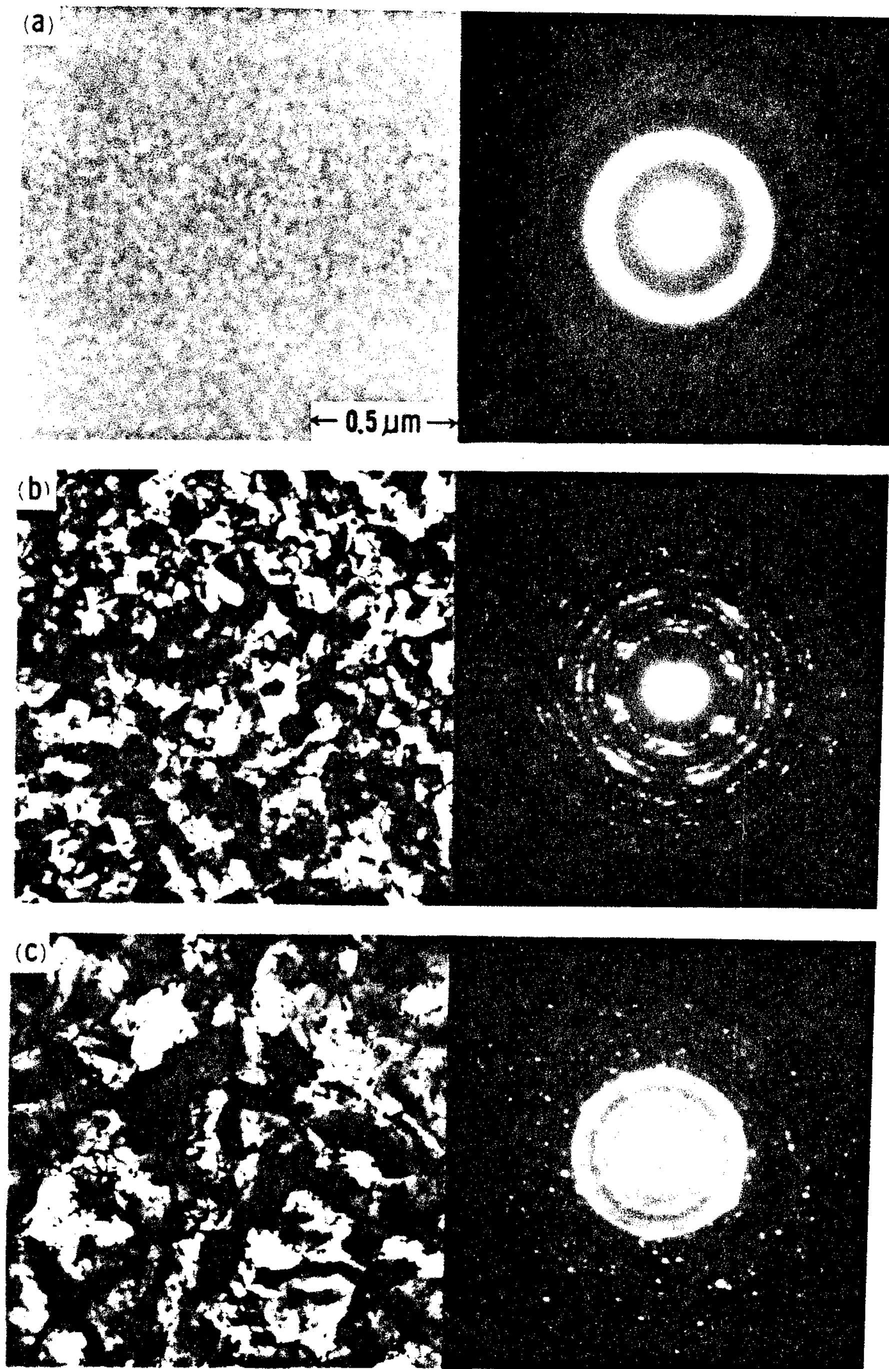

Fig. 4.4 Transmission electron micrographs and diffraction patterns for the co-deposited, ion-mixed Pt_2Si_3 alloys: (a) as implanted, (b) annealed at 450^oC for 30 min, (c) annealed up to 600^oC.

grain size of the order of 1000 Å. Finally, Fig. 4.4c shows the equilibrium structure after continuous annealing up to $600^{o}C$. The diffraction pattern reveals strong dots and continuous lines due to the large PtSi crystallites and randomly oriented Si precipitates, respectively. The Si precipitates, appearing as irregular white spots in the bright-field image, are formed predominantly near the PtSi grain boundaries. Detailed inspection of the micrograph shows numerous small circular white dots of 50-100 Å in diameter. These are presumably due to the Xe gas bubbles formed during the annealing.

As mentioned in Section 3.2 of Chapter 3, an amorphous Pt_2Si_3 alloy can also be formed by ion-beam mixing of thin PtSi films on Si, but with a slight concentration gradient across the film (Fig. 3.1 of Chapter 3). TEM examination of those ion-induced Pt-Si alloys showed similar amorphous diffraction pattern and similar contrast in the bright field image. We compare in Fig. 4.5 the elastically scattered electron intensity in arbitrary units versus the momentum transfer vector $|\vec{s}|$ (where $|\vec{s}|=4\pi\sin\theta/\lambda$ in $(\text{Å})^{-1}$) for the (a) ion-induced α-Pt_2Si_3 alloy, and (b) co-deposited, ion-mixed α- $Pt_{40}Si_{60}$ alloy. Intensity maxima are observed at $|\vec{s}|$= 2.80, 3.20, 4.41, 5.12 and 6.95 $(\text{Å})^{-1}$ as indicated by the arrows in the figure. These two diffraction patterns are qualitatively very similar. The intensity of the first halo at $|\vec{s}|$ = 2.80 $(\text{Å})^{-1}$ is higher for the co-deposited, ion-mixed α-$Pt_{40}Si_{60}$ alloy, while the splitting of the second amorphous halo at $|\vec{s}|$ = 4.41 and 5.12 $(\text{Å})^{-1}$ is higher for the ion-induced α-Pt_2Si_3 alloy. Because of multiple scattering in these samples the intensity modulations for $|\vec{s}|$ > 10 were not observable.

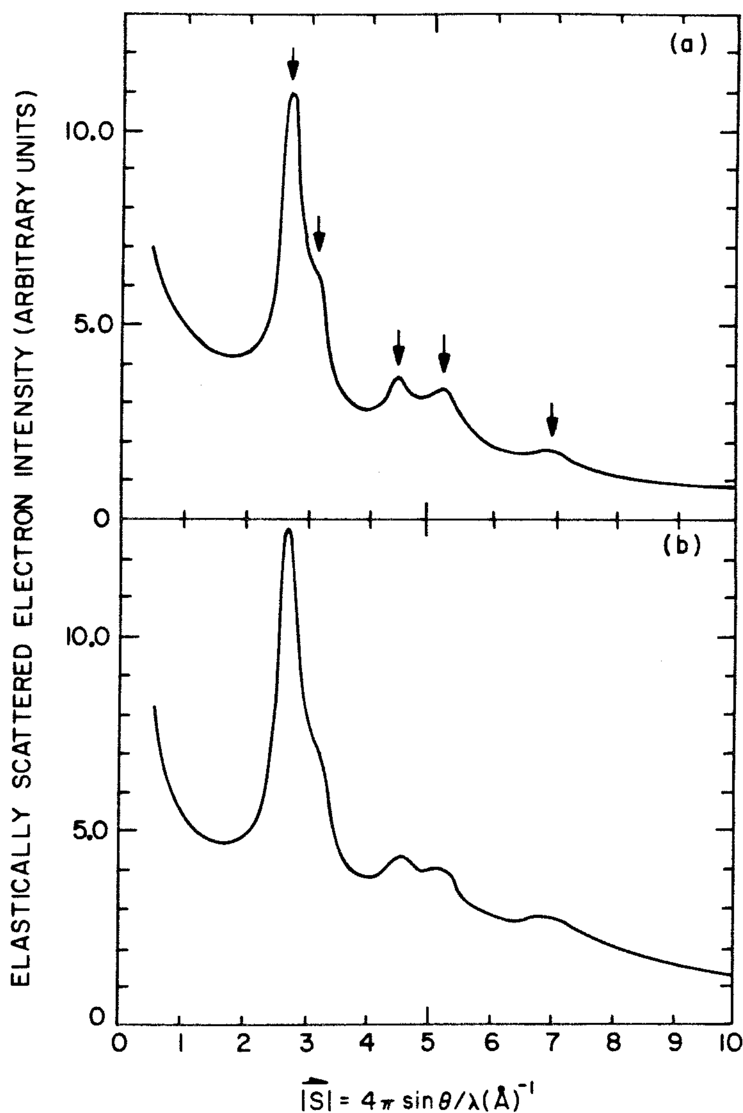

Fig. 4.5 Elastically scattered electron intensity versus scattering vector $|\vec{s}|$ for the: (a) ion-induced α-Pt_2Si_3 alloy and (b) co-deposited, ion-mixed α-$Pt_{40}Si_{60}$ alloy. Intensity maxima are observed at $|\vec{s}|$ =2.80, 3.20, 4.41, 5.12 and 6.95 $(\text{Å})^{-1}$ as indicated by the arrows.

It was not possible to obtain stable thin sections of samples in order to obtain data for $|\vec{s}|>10$. This also prevents us from obtaining reliable radial distribution functions for these samples and therefore the analysis of the electron intensity tracing is qualitative.

The microstructures of the alloys during the transformation from the amorphous to metastable crystalline state has also been studied. Film for such measurement was annealed isothermally for a constant annealing time. Resistivity and x-ray diffraction measurements were then performed to ensure the partial transformation of the originally amorphous phase. Fig. 4.6a and b show the electron micrographs (dark field) and diffraction pictures for samples annealed for 60 min. at 380 and 384°C, respectively. As shown in the diffraction pattern of Fig. 4.6a, weak crystalline reflections were found superimposed to the amorphous halos. Dark field techniques reveal coherently diffracting particles of about 100 Å in diameter due to the Pt_2Si_3 nuclei which appear as white rounded spots in the micrograph. The resistivity of this sample was measured to be 320 μΩ-cm which is about 15% lower than that of the pure amorphous phase (see Fig. 4.3). The samples annealed at higher temperature (384°) showed stronger crystalline reflections (Fig. 4.6b). The size of the Pt_2Si_3 crystallites remains roughly the same but the number increases drastically compared to that shown in Fig. 4.6a. The resistivity of this film is 145 μΩ-cm which is about 15% higher than that of the metastable Pt_2Si_3 phase (Fig. 4.3).

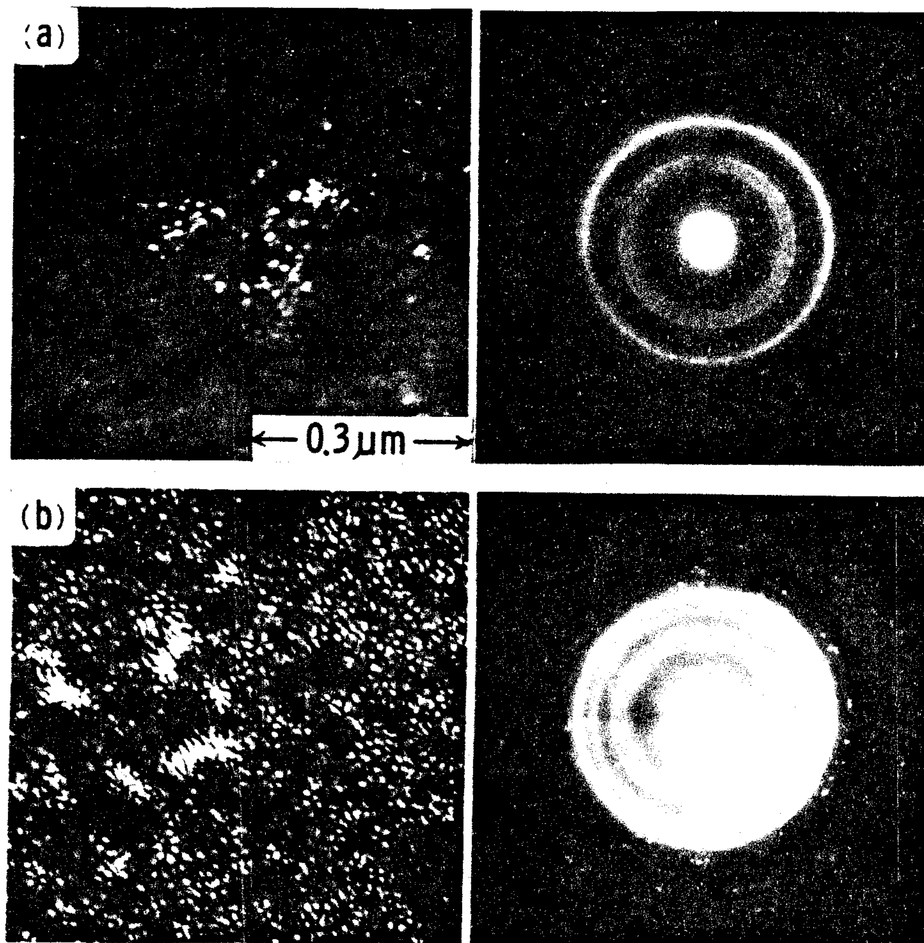

Fig. 4.6 Transmission electron micrographs (dark field) and diffraction patterns for the co-deposited, ion-mixed Pt_2Si_3 alloy: (a) annealed at 380^oC for 30 min, (b) annealed at 384^oC for 30 min. The number of the Pt_2Si_3 crystallites increases drastically with annealing temperature but the size remains roughly the same.

4.3.3 Kinetics Analysis

The first distinct stage in the annealing curve of Fig. 4.1 represents the transformation from the amorphous to the metastable crystalline structure. The significant differences in resistivities between the amorphous and crystalline phases allows us to use isothermal annealing to study the transformation kinetics in some detail. The sigmoidal shape of the isothermal annealing curves (shown in Fig. 4.3) and the microstructures of the alloys during crystallization suggest that the transformation from the amorphous to metastable crystalline state follows a nucleation and growth mechanism. In this section, we present results of a kinetics study based on a classical analysis for the nucleation and growth transformation using resistivity annealing data of Fig. 4.3.

The generalized relation for nucleation and growth transformation is given by [8,9]:

$$X_T(t) = 1 - \exp(-kt^n) \quad (4.1)$$

where X_T is the fraction volume transformed, k a kinetic constant, t the time, and the exponent n is determined by the transformation mode. It was shown [9] that n ranges from 3 to $4\frac{1}{2}$ for interface controlled growth processes, and from $1\frac{1}{2}$ to $2\frac{1}{2}$ for diffusion controlled growth processes. The exact value of n is dependent on the nucleation rate (i.e., increasing, constant, decreasing or zero nucleation rate).

In order to convert the above kinetic equation into an equation in the resistivity, $\rho(t)$, the relation between ρ and X_T must be known.

We postulate a linear relationship [4], although we recognize that such an assumption may amount to an oversimplification. Thus

$$X_T(t) = \frac{\rho_o - \rho(t)}{\rho_o - \rho_m} \tag{4.2}$$

where ρ_o is the resistivity at the start of the crystallization, ρ_m the value at the end of the stage, and $\rho(t)$ the instantaneous value. In the isothermal annealing curves shown in Fig. 4.3, we take the maximum resistivity as ρ_o, and the time corresponding to this maximum as the time origin (see inset of Fig. 4.3). The time origin is defined this way to account for the initial time delay of temperature rise, but the corrections (2-5 min) are very small.

Fig. 4.7 shows the $X_T(t)$, the fraction of material crystallized after time t at annealing temperature T, converted from the isothermal annealing curves of resistivity (Fig. 4.3) for the codeposited, ion-mixed Pt_2Si_3 alloy films using Eq. 4.2. The temperature dependence of the crystallization rate can be obtained by defining a time constant, τ, at which half of the total materials have been transformed, i.e., $X_T(\tau) = \frac{1}{2}$. In Fig. 4.8, τ is plotted against 1/T and is described over the narrow temperature interval by an equation of the Arrhenius form:

$$\tau = \tau_o \, e^{\Delta E/RT} \tag{4.3}$$

The apparent activation energy $\Delta E(=RT \ln \tau/\tau_o)$ was found to be 4.69 eV (108 kcal/mole).

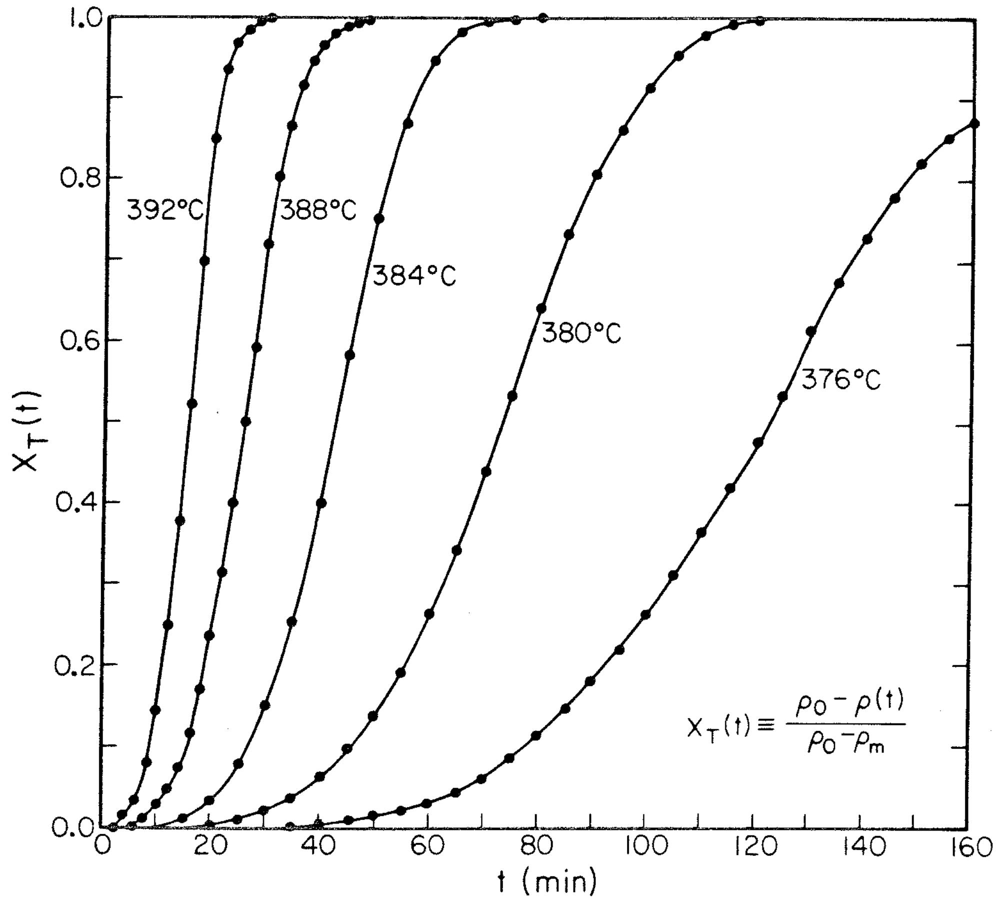

Fig. 4.7 The transformed volume, $X_T(t)$, of crystallization of the amorphous Pt_2Si_3 alloy as a function of annealing time at different temperatures. The curves are converted from the isothermal annealing curves of Fig. 4.3 using Eq. 4.2.

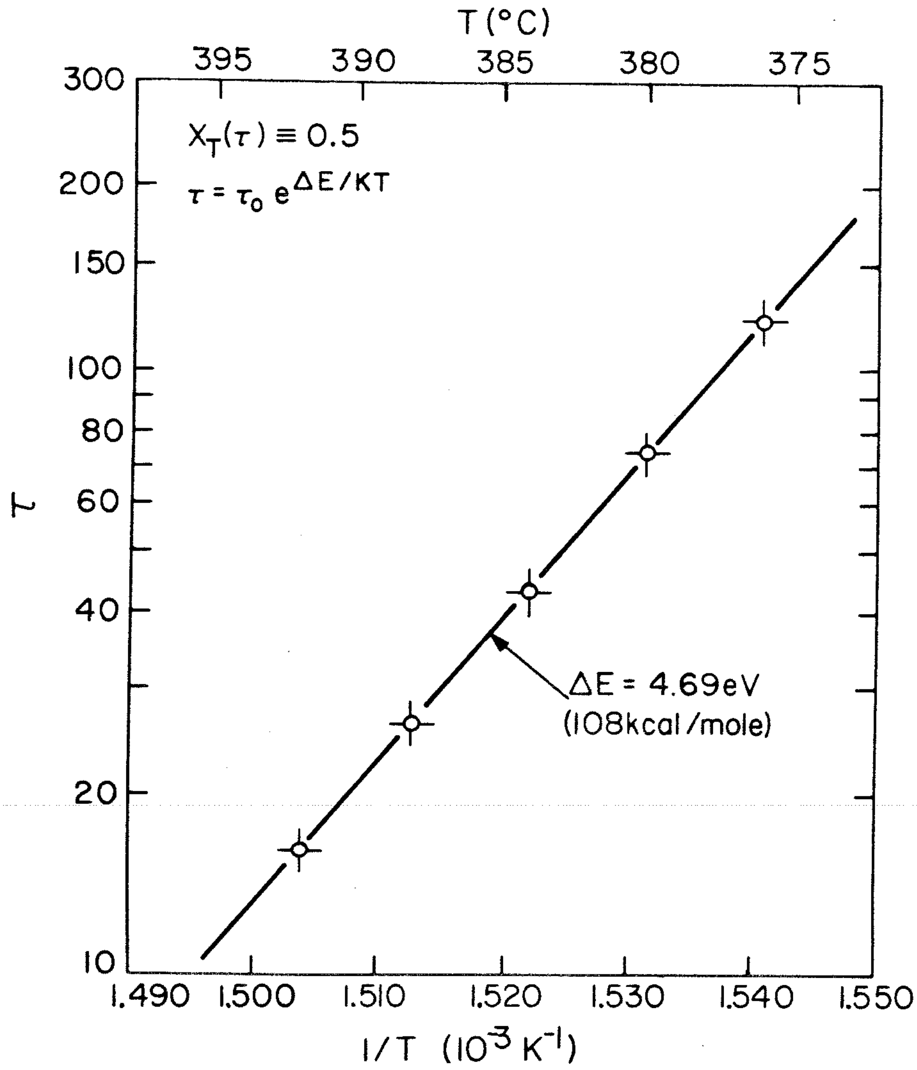

Fig. 4.8 The logarithms of characteristic crystallization time constant, τ, of the amorphous Pt_2Si_3 alloy versus 1/T. The apparent activation energy is 4.69 eV (108 kcal/mole).

On the other hand, the time dependences of the extended volume of the growing phase can be obtained by plotting the reduced $X_T(t/\tau)$ $(= - \ell n\ \{1-X_T(t)\}/\ell n2)$ versus t/τ for different temperatures since it should have the same form for the same kind of transformation. The reduced $X_T(t/\tau)$ is derived in the following: by definition,

$$X_T(\tau) = \frac{1}{2} = 1 - \exp(-k\tau^n) \tag{4.4}$$

eliminating k between Eqs. 4.1 and 4.4, we have

$$\frac{-\ell n\{1-X_T(t)\}}{\ell n2} = (\frac{t}{\tau})^n$$

The exponent n can then be obtained by fitting the reduced plot of $X_T(t/\tau)$ versus t/τ with a cure $y = x^n$ and the result is shown in Fig. 4.9. The data points agree well with $y = x^n$ with n=4.

4.4 Discussion

As mentioned before, the attempt to produce a homogeneous metastable Pt_2Si_3 phase by direct annealing of a co-deposited amorphous $Pt_{40}Si_{60}$ alloy film was unsuccessful. This has been attributed to the non-uniformity of the original alloy as suggested by the experimental observation that a homogeneous Pt_2Si_3 phase can be obtained from a co-deposited film after ion-beam mixing. The resistivity annealing curves for the co-deposited alloys with or without ion bombardment (shown in Fig. 4.1 and 4.2, respectively) provide further support for this argument. The continuous decrease of resistivity for the co-deposited

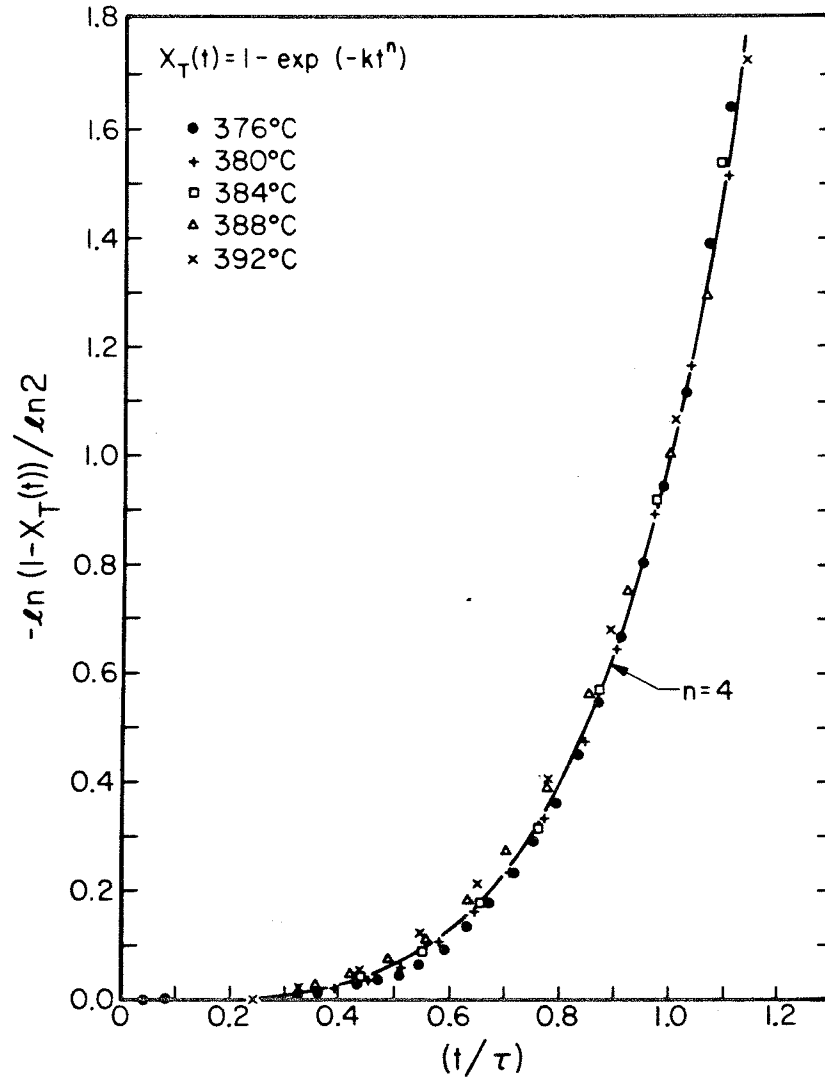

Fig. 4.9 The reduced transformation volumes, $-\ell n\ \{1-X_T(t)\}/\ell n2$, versus t/τ of the amorphous Pt_2Si_3 alloy annealed at various temperatures. The solid curve is the plot of $(t/\tau)^n$ with n=4.

alloy in the early stage of annealing (Fig. 4.2) is believed due to nucleation and growth of the equilibrium PtSi phase. This reaction can take place at temperatures below 300°C in the region where the local composition of the alloy film is close to PtSi. Consequently, nucleation of the metastable Pt_2Si_3 phase is overshadowed because it requires higher temperatures($\sim$400°C). On the other hand, the transformation behavior observed for the ion-mixed alloys (Fig. 4.1) indicates that the PtSi phase does not form before crystallization. This is because the composition of the ion-mixed Pt_2Si_3 alloy is quite uniform (probably in atomic scale) and hence nucleation of the PtSi phase is suppressed.

The resistivity annealing curve of Fig. 4.1 shows a small initial drop below 100°C and a slight increase in the temperature range of 350-380°C. The origin of this initial drop of resistivity is not clear and may be related to the "relaxation" of the amorphous structure [10]. The small increase of resistivity before crystallization is presumably due to formation of very small crystallites embedded in the amorphous matrix. Such microcrystallites could act as additional scattering centers for electrons during the earliest stage of their development when they are still far apart [11,12]. The amorphous Pt_2Si_3 alloy exhibits a positive but rather small temperature coefficient of resistivity ($1\times10^{-4}/^{o}C$) between 100 and 350°C. Evidently, the electrical resistivity of the amorphous alloy is mainly governed by scattering resulting from a random structure and the phonon contribution is of secondary importance [13].

The bright field micrograph shown in Fig. 4.4a has a slight white-dark contrast. This white-dark contrast on the scale of 100 Å is suggestive of compositional fluctuations in these amorphous films. The existence of compositional fluctuations which lead to isotropic clusters of high and low Pt concentration is further supported by the small angle scattering profiles of Fig. 4.5. We observe that these intensity profiles rise at low angles. Such rising intensity profiles are presumably produced by compositional fluctuations and porosity of the material [14,15].

Finally, it is desirable to discuss the kinetics of the amorphous to metastable crystalline transformation based on the analysis discussed in Section 4.3.3. The order of transformation determined from the reduced plot of $X_T(t/\tau)$ versus t/τ (Fig. 4.9) is equal to 4 in the present case. According to the classical theory for nucleation and growth transformation, a t^4 time dependence is consistent with an interface controlled growth process with a constant nucleation rate [9].

The apparent activation energy (ΔH = 108 kcal/mole) observed for the crystallization of amorphous Pt_2Si_3 alloys is quite high. Such high activation energy has been observed in the crystallization of liquisol quenched amorphous Pd-Si based alloys such as $Pd_{0.8}Au_{0.035}Si_{0.165}$ glossy alloy (ΔH = 103 kcal/mole) by Chou and Turnbull [2] and $Pd_{0.775}Cu_{0.06}Si_{0.165}$ alloy (ΔH = 95 kcal/mole) by Bagley and Vogel [16]. The magnitude of activation energy was found to agree well with that of viscosity in those glasses over the temperature interval of their studies. It was therefore proposed that the crystal growth rate in

those systems (Pd-Si based alloy glasses) is viscosity limited. The viscosity data for amorphous Pt_2Si_3 alloys are not available so that no comparisons can be made in our case. However, the high activation energy can also be associated with a large free energy barrier for nucleation. According to classical nucleation and growth theory, the t^4 time dependence arises from a "3-dimensional" interface-controlled nucleation growth process [9]. By applying dark field and tilting techniques in TEM analysis, we concluded that the Pt_2Si_3 crystallites were roughly spherical in shape. On the other hand, the observation that the number of crystallites increase drastically with temperature but the size remains the same (Fig. 4.6) also suggest that the activation energy for nucleation seems to be the rate limiting factor.

4.5 Conclusion

In conclusion, the transformation behaviors of the ion-beam-induced amorphous Pt_2Si_3 alloys has been studied by using resistivity measurement. Two distinct stages of transformation were observed as revealed by a rapid change of resistivity with increasing annealing temperature. In the first stage, a transformation from amorphous to metastable crystalline Pt_2Si_3 phase occurred in a narrow temperature range around 400^oC. The second stage, which appeared broader near 550^oC, involved the transformation to the equilibrium two-phase state of PtSi and Si. The kinetics of amorphous to metastable crystalline transformation has been determined by isothermal treatment over the temperature interval

376-392°C. The results are interpreted in terms of a classical nucleation and growth mechanisms with a t^4 dependence and an apparent activation enthalpy of 108±5 kcal/mole. The structures of the alloys at various stages of transformation were studied by transmission electron microscopy and diffraction. It was suggested from the kinetics analysis and TEM observations that the crystal growth rate in the amorphous Pt_2Si_3 alloys is nucleation limited.

References

1. P. Duwez, Transactions of the ASM, 60, 607 (1967).
2. See for example, C.-P.P. Chou and D. Turnbull, J. Non-cryst. Solids 17, 169 (1974).
3. See for example, A. C. Damask and G. J. Dienes, Point Defects in Metals (Gordon and Breack, New York 1963) Chap. 3.
4. S. Mader and A. S. Nowick, Acta. Metall. 15, 215 (1967).
5. C. H. Lin, Harvard University, private communication, 1979.
6. S. Mader, J. Vac. Sci. Technol. 2, 35 (1965).
7. J. F. Graczyk and P. Chaudhari, Phys. Stat. Sol.(b) 58, 163 and 501 (1973).
8. D. Turnbull, in Solid State Physics, F. Seitz and D. Turnbull, Eds., Vol. 3 (Academic Press, New York, 1950), p. 225.
9. J. W. Christian, The Theory of Transformation in Metals and Alloys, (Pergamon Press, Oxford, 1965) Chap. 12.
10. U. N. Tu, private communication, 1979.
11. H. S. Chen and D. Turnbull, J. Chem. Phys. 48, 2560 (1968).
12. P. Maitrepierre, J. Appl. Phys. 41, 498 (1970).
13. P. Duwez, R. Willens and R. Crewdson, J. Appl. Phys. 36, 2267 (1965).
14. A. Guinier, X-Ray Diffraction (W. H. Freeman and Co., San Francisco, 1963).
15. C. G. Shull and L. C. Roess, J. Appl. Phys. 18, 295 (1947).
16. B. G. Bagley and E. M. Vogel, J. Non-cryst. Solids 18, 29 (1975).

Chapter 5

METASTABLE Au-Si ALLOYS FORMATION INDUCED BY ION-BEAM-MIXING

5.1 Introduction

It has been shown that ion-bombardment through a thin metal film or a compound layer on a Si substrate can induce atomic mixing between the film and the substrate. Formation of equilibrium phases such as metal-silicides (Chapter 2) as well as nonequilibrium phases such as amorphous metal-Si alloys have been observed under various implantation conditions. In the latter case, metastable phases can be produced upon past-annealing in the Pt-Si system (Chapters 3 and 4).

The observation of new metastable phases in the Pt-Si system is encouraging and leads to further investigations of metastable alloy formation in other systems. In this chapter, a study of ion-induced interactions between Au and Si by implanting energetic ions through the Au-Si interface is reported. It is known that under equilibrium conditions, the Au-Si system is a simple eutectic (∿18 at.% Si at 370°C) with negligible solid solubility and no intermediate phases [1]. However, by rapid quenching of Au-Si liquid [2] or vapor [3] near eutectic composition or by use of Q-switch laser melt-quench techniques[4], amorphous alloys can be formed. The amorphous phase is unstable at room temperature and transforms into a metastable crystalline phase, which then gradually decomposes into an equilibrium Au and Si mixture. Both amorphous and metastable phases exhibit characteristics similar to those

in the liquid state but are significantly different from those of the equilibrium mixture. Some general features of Au-Si phases near eutectic composition are listed in Table V-I.

TABLE V-1. Selected Properties of Au-Si Binary Phases Near Eutectic Composition

	Liquid	Amorphous	Metastable Crystalline	Au and Si Equilibrium Mixture
Color [(a)]	Silver	Silver	Silver	Gold
Density [(a)]	High	High	High	Low
Si-Bonding [(b)]	Metallic	Metallic	Metallic	Covalent

(a) From Ref. 5

(b) From Ref. 3

The purposes of the present work are to study ion-induced atomic mixing in a non-compound forming system and to investigate the possibility of producing metastable Au-Si alloys by ion-beam-mixing techniques.

5.2 Formation of Amorphous Au-Si Alloys

Figure 5.1 shows the backscattering spectra of 400 Å Au/Si <111> samples that have been bombarded with 300 keV Xe^+ at R.T. to doses of 2, 5 and $9 \times 10^{14} cm^{-2}$, respectively. A well-defined layer of Au-Si mixture

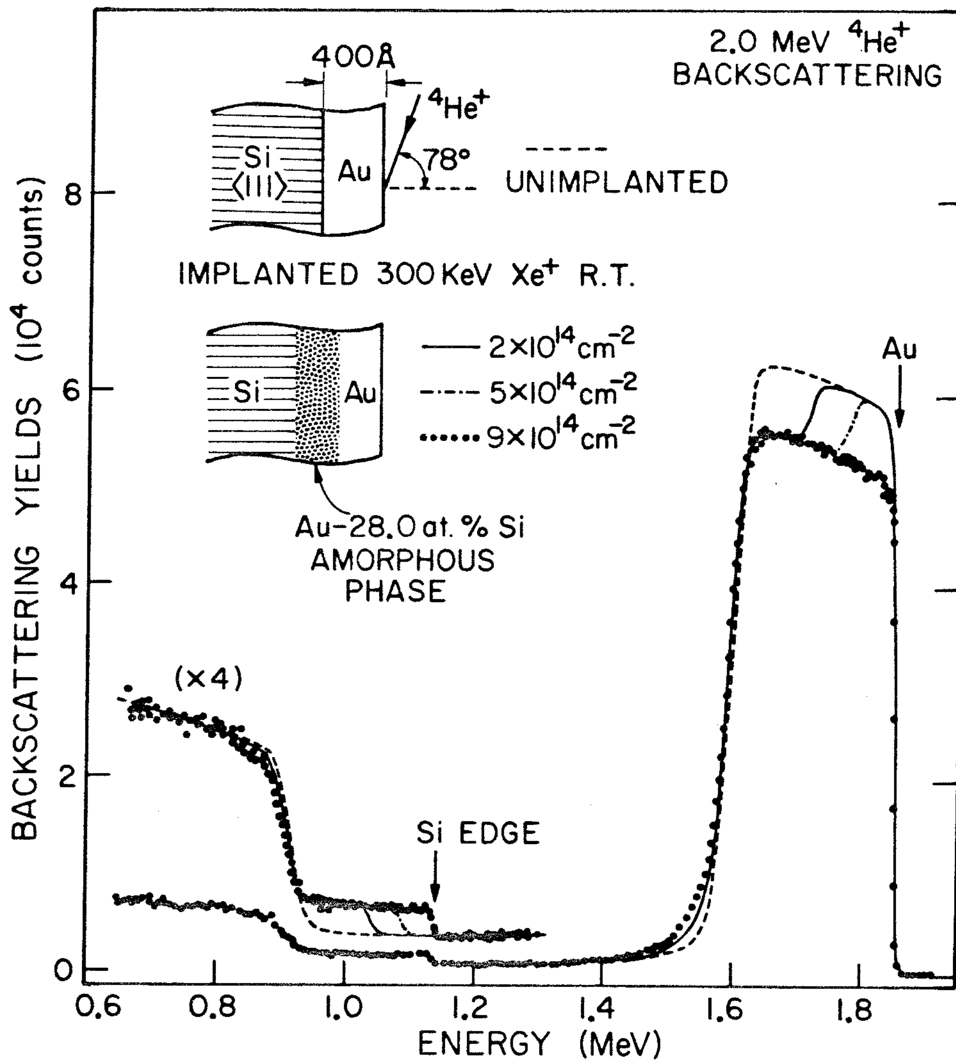

Fig. 5.1 Ion backscattering spectra which show the "layered growth" of a uniform Au-Si mixture induced by implanting energetic Xe ions through a thin Au film deposited on a Si substrate. The structure of this ion-induced mixed layer is amorphous as indicated by x-ray diffraction measurements.

with a composition close to Au-28.5 at.% Si ($\sim Au_5Si_2$) has been formed near the interface. The thickness of the layer increased with ion dose and the 400 Å Au film was completely mixed with Si at a dose of $9\times10^{14} cm^{-2}$. Inspection of this sample with an optical microscope showed the surface to be quite smooth, but with a significant color change from golden to silverlike. X-ray diffraction analysis indicated the appearance of an intense diffused halo centered around $2\theta \approx 41°$ ($|\vec{S}| = 2.85$ Å^{-1}), which suggested a non-crystalline (glasslike) structure similar to that of liquisol-quenched amorphous Au-Si alloys [6]. No traces of the original Au reflections were observed.

Bombardment with lighter ion species (Ar^+ and Ne^+) produced a similar Au-Si mixture of Au_5Si_2 composition except that higher ion doses were required to achieve the same amount of intermixing obtained with Xe ions. Fig. 5.2 shows that the thicknesses of the Au-Si mixed layers increase approximately with the square root of ion doses. In all cases, ions penetrate the Au-Si interface and the projected range of the lighter ions is deeper due to smaller energy loss. For a given dose, the thickness is greater for bombardment with heavier mass ions.

To further investigate the effect of ion bombardment on interface mixing, implantations have been performed at reduced substrate temperatures. Fig. 5.3 shows the backscattering spectra of a series of Ar-implanted samples at various temperatures but under otherwise identical implantation conditions. A slight reduction in the amount of reaction was observed at lower temperatures and the mixed layers were found to be progressively less uniform as the implantation temperature decreased.

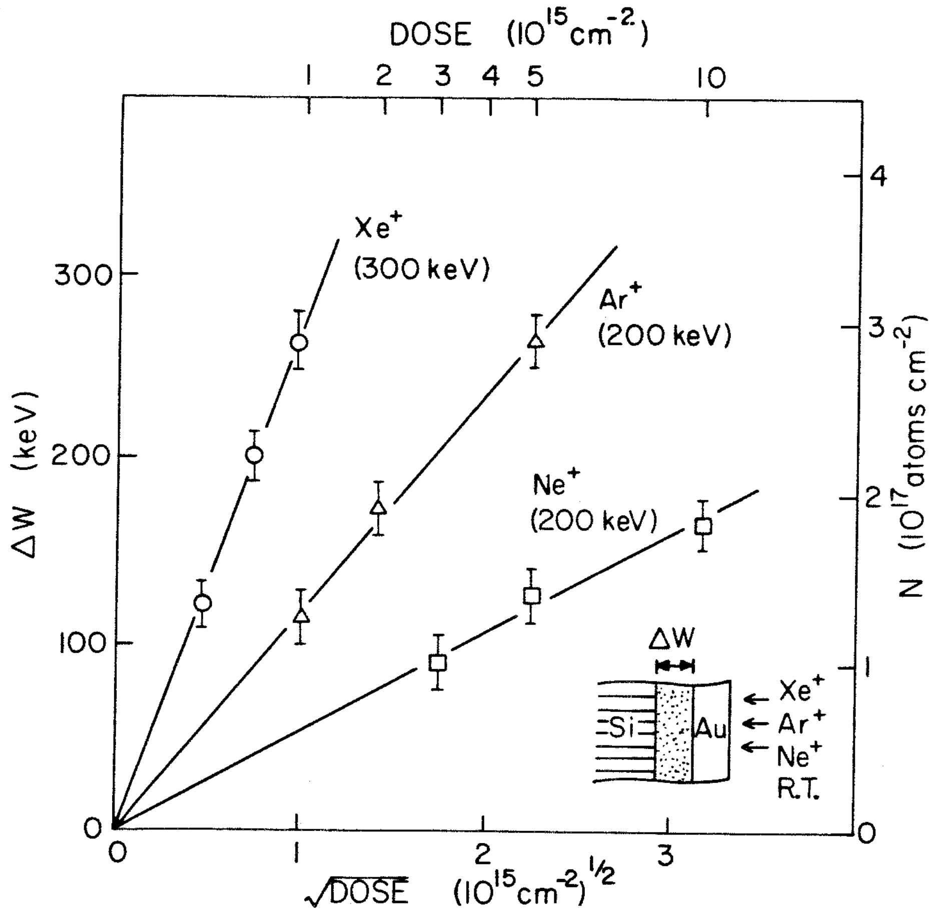

Fig. 5.2 The thicknesses of the ion-induced Au-Si mixed layers as a function of the square root of ion doses. The original Au film thickness is 400 Å. N is the number of atoms per cm^2 contained in the mixed layer as determined by backscattering measurements.

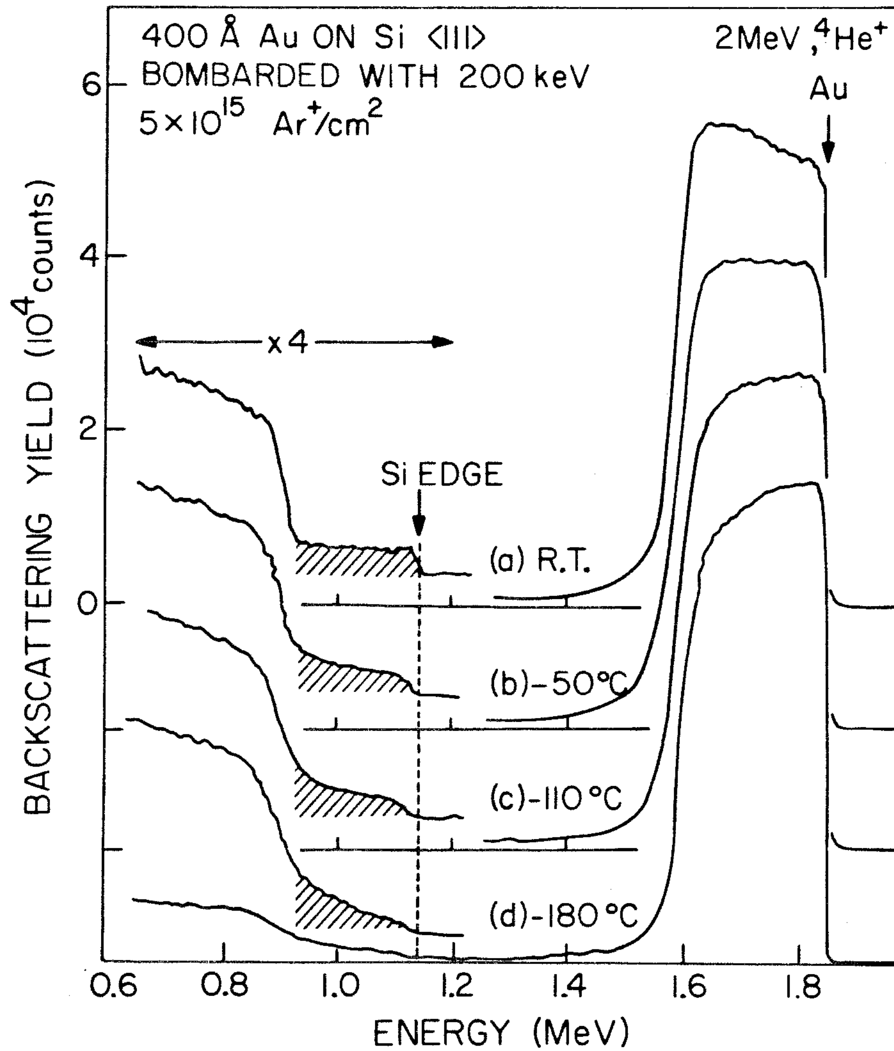

Fig. 5.3 Ion backscattering spectra for Au/Si samples bombarded with 200 keV 5 x 10^{15} Ar ions/cm^2 at various substrate temperature. The interfacial mixed layers become progressively less uniform as the implantation temperature decreases.

X-ray diffraction analysis of those ion-induced layers showed similar amorphous diffraction pattern. Faint traces of the original Au reflections were found in the sample implanted at LN_2 temperature presumably due to the residual Au near the film surface which has not been completely mixed with Si.

Upon post-annealing at 120^oC for 30 min, the nonuniform Au-Si mixture (obtained by low temperature implantation) transformed into a layer of uniform composition ($\sim Au_5Si_2$) next to the Si substrate together with a thin layer of Au on the surface. This is illustrated in Fig. 5.4 where backscattering spectra of unimplanted, as-implanted (at LN_2 temperature) and post-annealed (120^oC, 30 min) samples are shown superimposed upon one another. X-ray diffraction measurements revealed polycrystalline diffraction pattern consisting of Au (f.c.c.) reflections and over 40 additional crystalline reflection peaks, which have been identified to belong to a hexagonal metastable phase (described in Section 5.4). This result shows that redistribution (interdiffusion) of atoms within the mixed layer occurred during the annealing similar to that observed in the formation of metastable Pt_2Si_3 phase (Figs. 3.1 and 3.2), and that excess Au was ejected from the metastable phase to precipitate out near the surface.

5.3 Transformation Behavior of the Ion-Induced Au-Si Alloys

To monitor the transformation behavior of the ion-induced amorphous Au-Si alloys, we have performed measurements of electrical resistivity under a constant temperature rise (isochronal annealing)

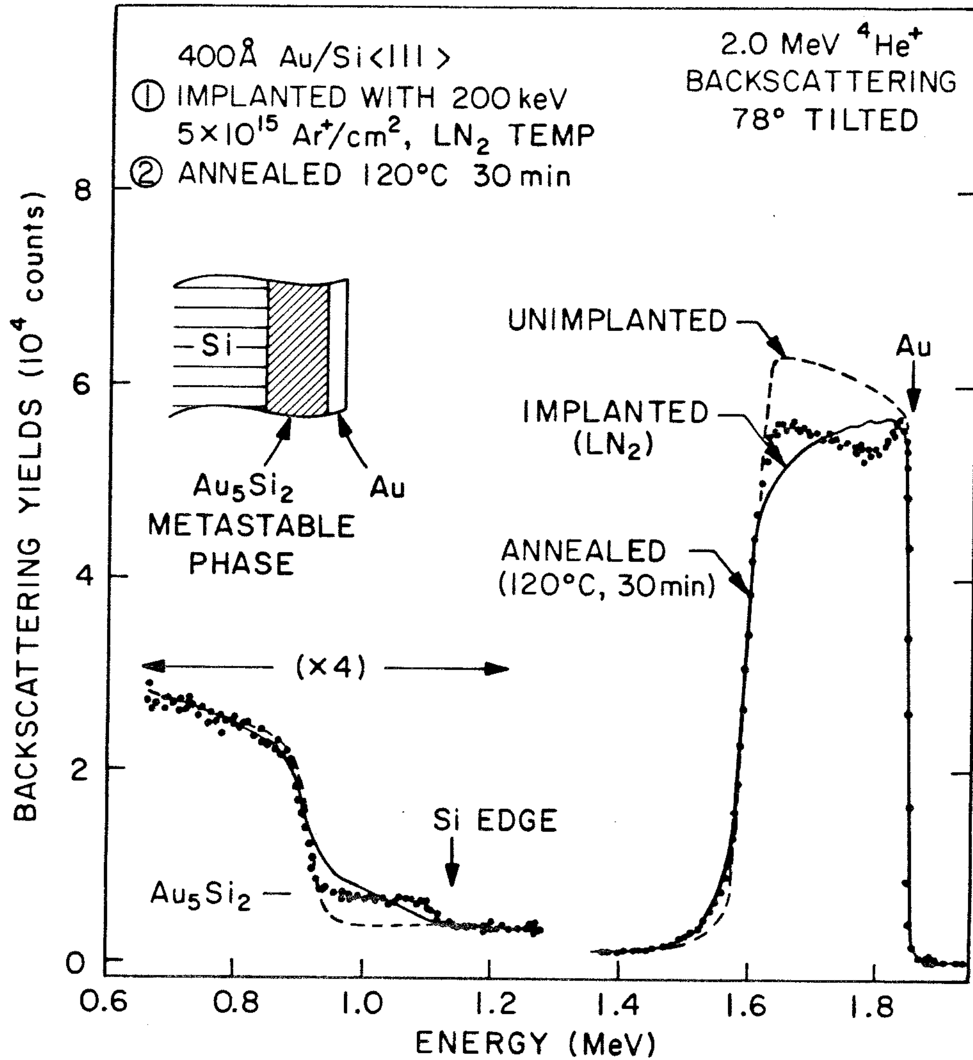

Fig. 5.4 Ion backscattering spectra for a Au/Si sample bombarded with 200 KeV 5×10^{15} Ar ions/cm^2 at LN_2 temperature and annealed subsequently at 120°C for 30 min. The nonuniform Au-Si mixture transforms into a layer of uniform composition (Au_5Si_2) next to the Si substrate together with a thin layer of Au on the surface.

or at a constant temperature (isothermal annealing) using four-point probe techniques. The apparatus and experimental procedures were similar to those described in Section 4.2 except that tungsten electrodes were used in the present measurements.

To eliminate contribution of conductivity from the Si substrates, samples for such measurements were multiple-layers [7] of Au and Si vacuum-deposited on insulating SiO_2 or Al_2O_3 substrates (inset of Fig. 5.5). The relative thicknesses of the alternative layers were adjusted such that the average film composition was Au_5Si_2. The individual layer thickness was not more than 100 Å with a total layer thickness of about 700 Å. Implantation was then carried out to promote atomic mixing. In this case, the projected range of the incident ions was about half of the total layer thickness. Uniformly mixed Au-Si layers have been achieved under low-dose ion bombardment and the SiO_2 substrate remained roughly undisturbed as shown in Fig. 5.5. The structure of those intermixed layers after ion bombardment was amorphous as confirmed by x-ray diffraction measurement.

Typical isochronal annealing curve of the ion-induced amorphous Au_5Si_2 alloys is shown in Fig. 5.6. The resistivity decreases slightly in the early stage of annealing (R.T. to 40°) and then increases gradually upon annealing between 40 and 90°C, with a positive temperature coefficient of the order of 2×10^{-4}/°C. After reaching a maximum at about 100°C, the resistivity drops in a sharp annealing step. X-ray diffraction measurements showed that before this annealing step the structure was amorphous; afterwards it was found to be a single metastable crystalline

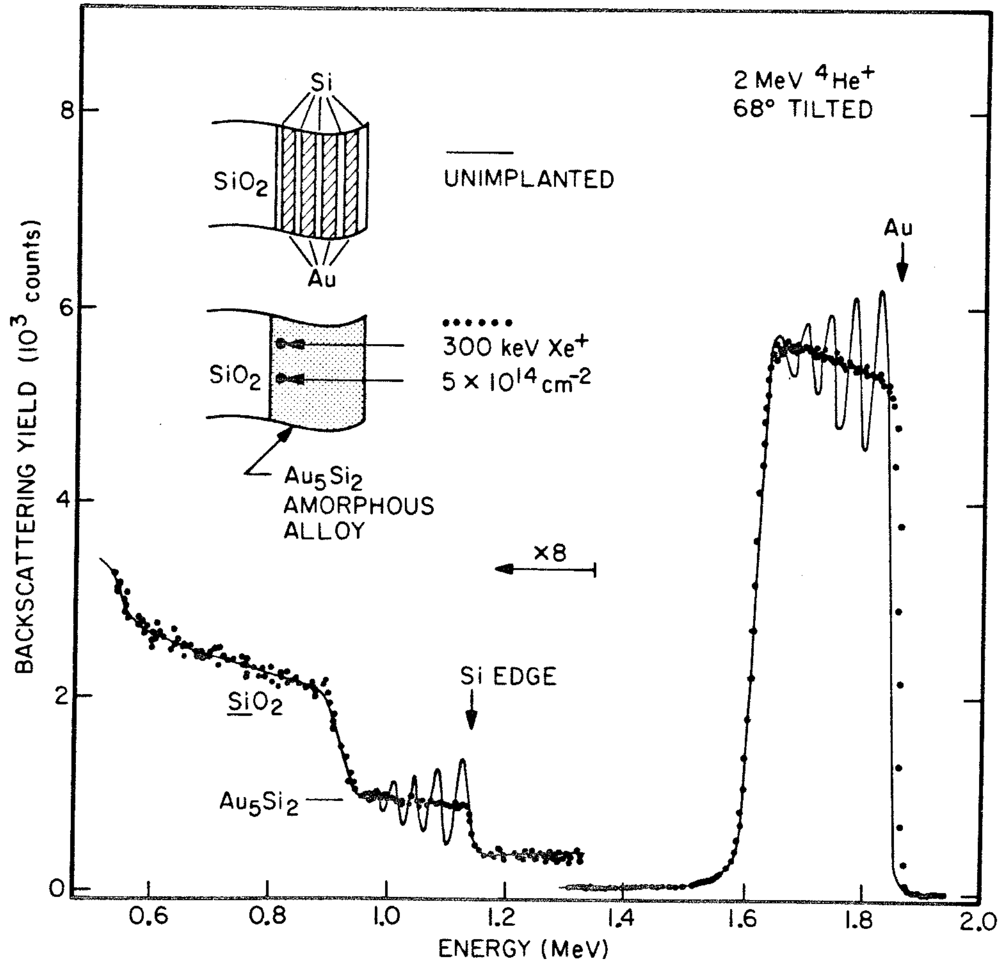

Fig. 5.5 Ion backscattering spectra which show the formation of an amorphous Au_5Si_2 alloy on a SiO_2 substrate by ion- beam-mixing of thin deposited Au and Si layers (see text).

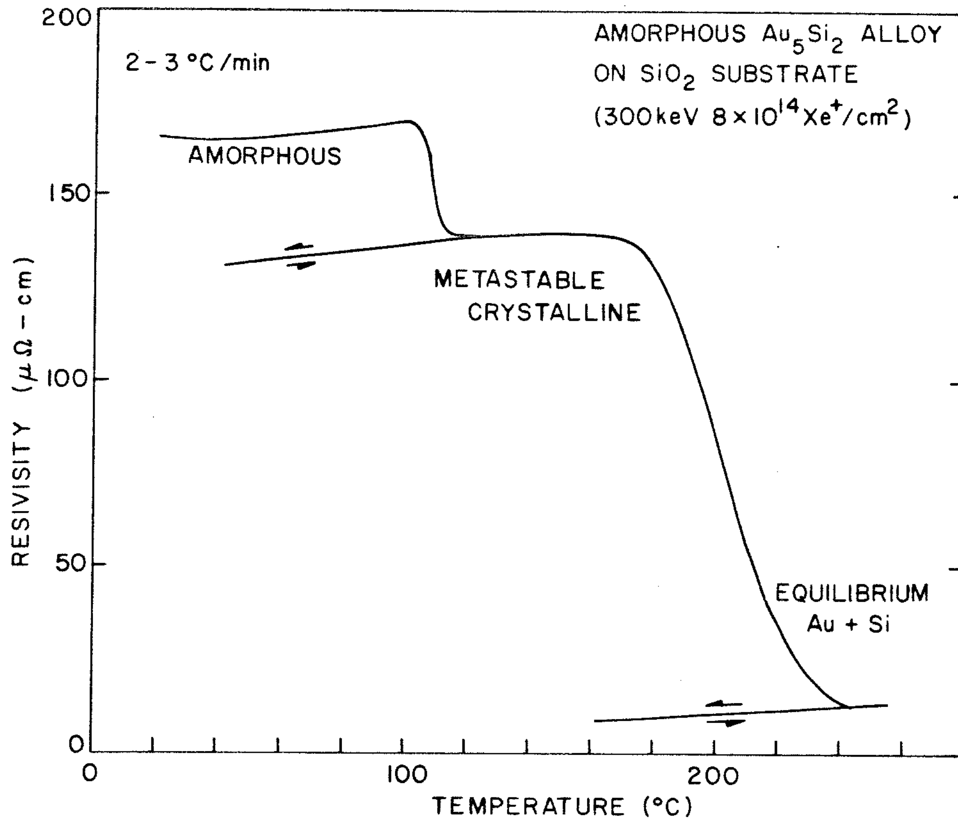

Fig. 5.6 Resistivity annealing curve for the ion-induced amorphous Au_5Si_2 alloy under heating at about 2 - 3°C/min. The amorphous alloy transforms into a metastable crystalline phase at about 100°C, which then gradually decomposes into an equilibrium two-phase Au and Si mixture at temperatures above 180°C.

phase. A reversible behavior of resistivity with changing temperatures (indicated by $\rightleftarrows$ in Fig. 5.6) is observed for the metastable phase with a positive temperature coefficient of $\sim 6\times10^{-4}/°C$. Upon further heating, the resistivity maintains roughly a constant value until a second annealing stage occurs which appears as a somewhat broader transition near 180°C. This corresponds to the transformation of the metastable phase into the two-phase (Au and Si) equilibrium structure as indicated by x-ray diffraction measurement. The resistivities of the amorphous, metastable crystalline and equilibrium phases are 165, 140 and 15 μΩ-cm, respectively.

Similar annealing characteristic have been found for amorphous Au_5Si_2 alloys produced by using Si ions or Xe ions of various doses ($3 - 8\times10^{15} cm^{-2}$), but with a slight difference in the transformation temperature (i.e., the temperature at which amorphous to metastable crystalline transformation occurs). The transformation temperature, ranging between 80 and 105°C, is lower for samples bombarded with Si ions and shifts to higher value with increasing Xe ion dose.

Isothermal annealing of the ion-induced amorphous Au-Si alloys has been performed over the temperature interval 85 - 101°C to study the kinetics of amorphous to crystalline transformation. A set of such annealing curves are shown in Fig. 5.7 where the percentage changes of resistances (or resisitivity) of the films are plotted against annealing time for four different temperatures. All the curves exhibit a similar shape: the resistivity increases slightly in the beginning, reaching a maximum and gradually falls as the crystallization proceeds. The iso-

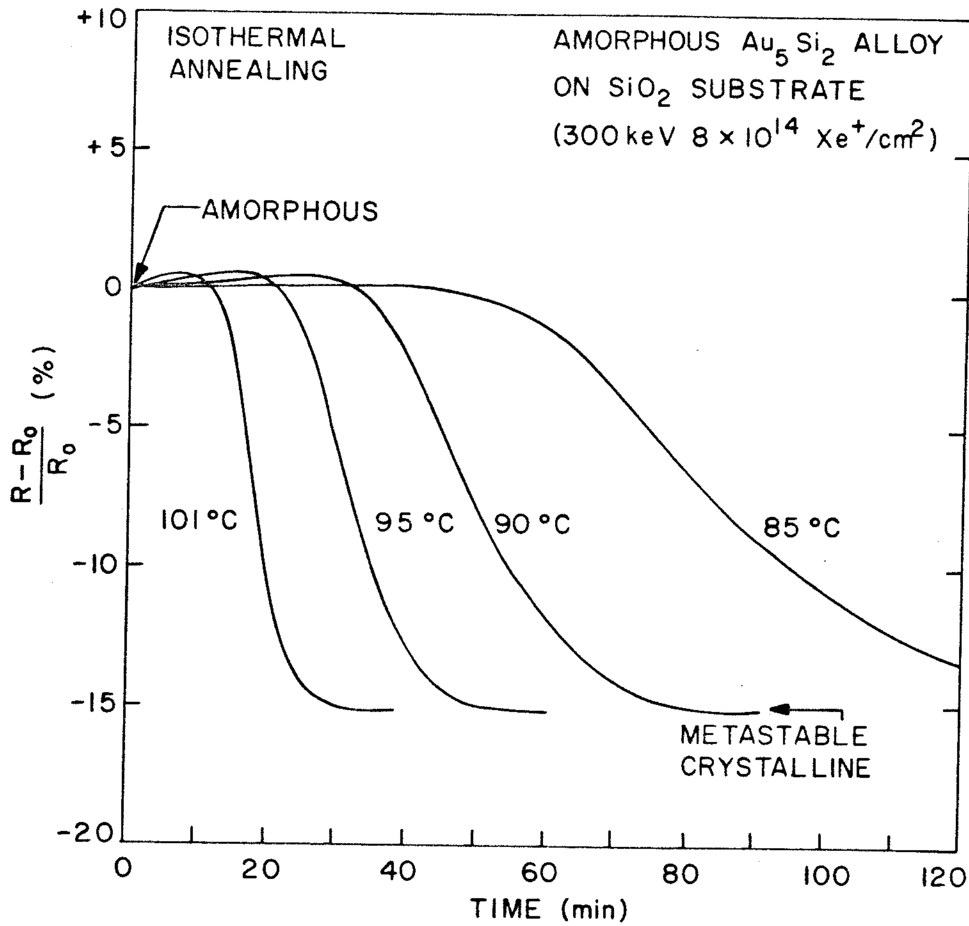

Fig. 5.7 Isothermal annealing curves for the ion-induced amorphous Au_5Si_2 alloys in the temperature interval 85 - 101°C. R_o is the resistivity (or resistance) of the film before annealing and R is the instantaneous value.

thermal curves shown in Fig. 5.7 appear to differ only by a time scale.

To obtain the temperature dependence of the transformation rate, we define a time constant, τ, at which the change of resistivity is about half of the total change, i.e., $(R-R_o)/R_o \simeq -7.5\%$. For example, $\tau \simeq 50$ min for the 90°C isothermal annealing curve. In Fig. 5.8, τ is plotted against $\frac{1}{T}$ and is described over the narrow temperature interval by an equation of the Arrhenius form: $\tau = \tau_o e^{\Delta E/RT}$. The apparent activation energy ΔE (= $RT \ell n\ \tau/\tau_o$) was found to be 1.1 eV (25 kcal/mole).

5.4 Microstructure

The microstructures of the alloyed layer at various stages of transformation were examined by transmission electron microscopy. Samples for such studies were single layer Au (400 Å) films on Si, bombarded with 300 keV Xe ions at R.T. to form uniform Au_5Si_2 mixed layers and then given the desired annealing treatment in the furnace. The thin foils for TEM observation were prepared by etching away the Si from the back. Fig. 5.9 shows the bright field micrographs and the corresponding electron diffraction patterns for a series of samples studied. The as-evaporated polycrystalline Au film (Fig. 5.9a) had a fine-grained structure and exhibited a strong <111> fiber texture. The ion-induced Au-Si mixed layers in the as-implanted samples were amorphous as indicated by the diffused halos in the diffraction pattern of Fig. 5.9b. These amorphous layers were found to be highly stressed and tended to curl up during the etching. Significant density or

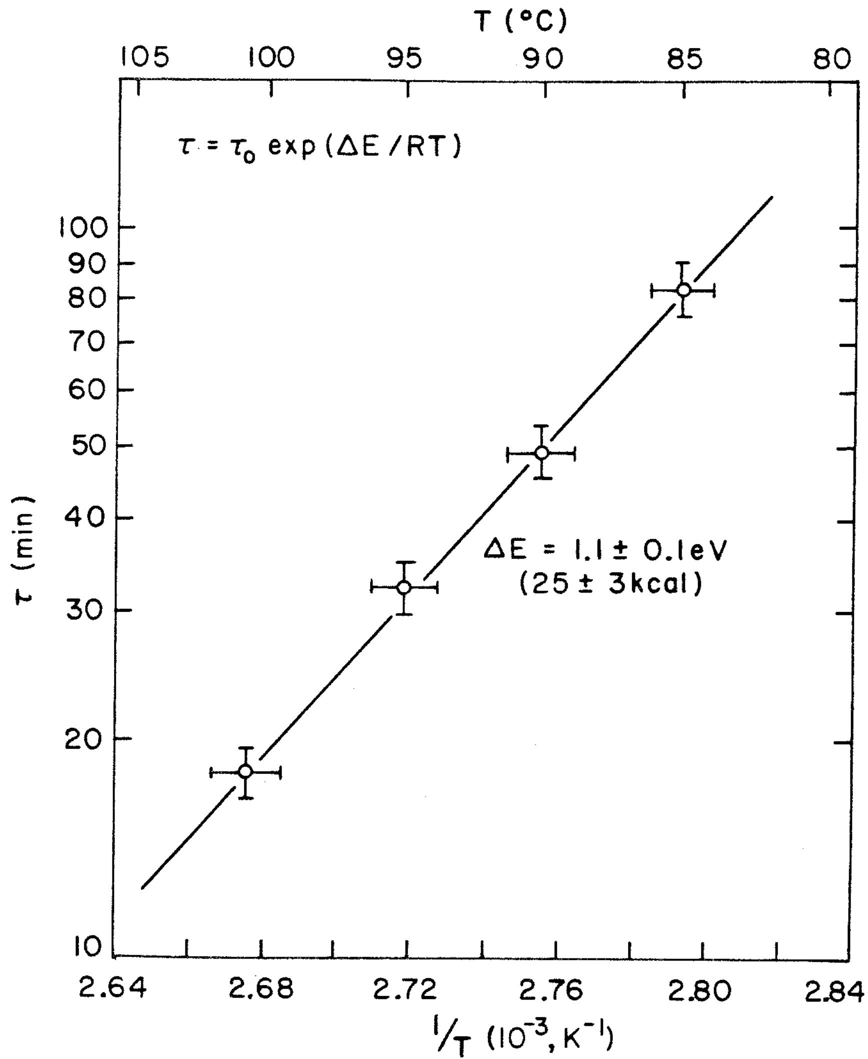

Fig. 5.8 The logarithms of charateristic crystallization time constant, τ (see text), of the amorphous Au_5Si_2 alloys versus 1/T. The apparent activation energy for crystallization is 1.1 eV (25 kcal/mole) in this temperature interval.

Fig. 5.9 Transmission electron micrographs and diffraction patterns for Au-Si samples: (a) as-deposited Au film, (b) as-implanted film, an amorphous Au-Si alloy was formed, (c) implanted and annealed at 100°C for 30 min, the amorphous film transformed into a metastable crystalline phase, (d) implanted and annealed at 180°C for 30 min, the metastable phase decomposed into an equilibrium Au and Si mixture.

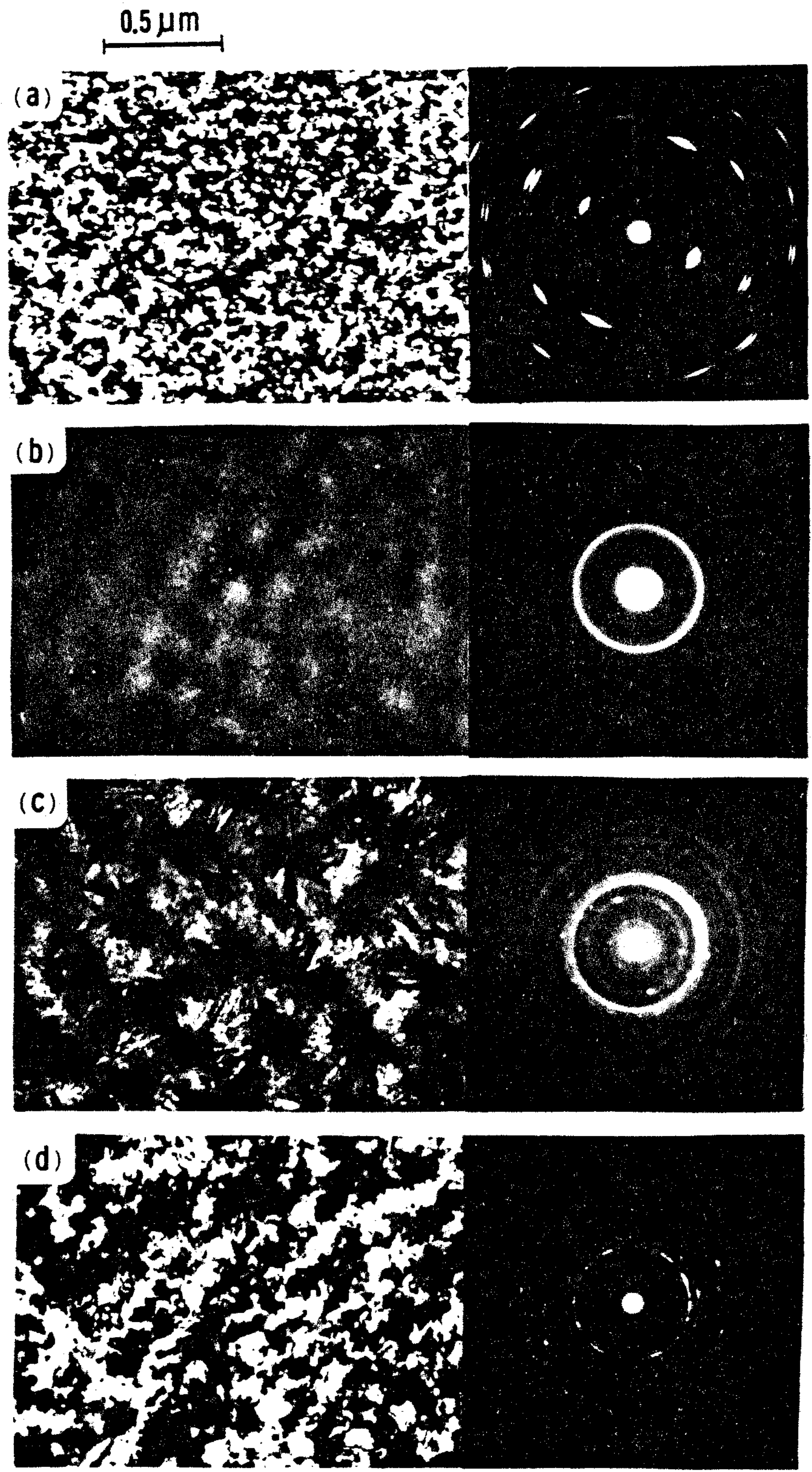
0.5 μm
(a)
(b)
(c)
(d)

thickness variation was found in those layers as shown by the black and white contrast in the micrograph. Fig. 5.9c shows that a drastic change of structure occurred in these amorphous Au-Si alloy layers after being annealed at temperature of ∿100°C, 30 min. The amorphous layer transformed into a metastable crystalline phase with a lamellar morphology, although no compositional change was observed from back-scattering measurement and the sample surface remained silverlike. The film was again under a high stress and the density or thickness variation was still present within the layer. Preliminary identification of crystal structure showed that the reflections of the metastable crystalline Au-Si phase agreed well with those of a hexagonal phase with lattice parameters a = 9.38 ± 0.02 Å and c = 15.46 ± 0.02 Å. The observed and calculated lattice spacings are listed in Table V-2.

Annealing at higher temperatures (>180°C) resulted in the decomposition of the metastable Au-Si phase into an equilibrium Au and Si mixture with a notable change of surface color from silver to gold. The micrograph and diffraction pattern are shown in Fig. 5.9d. The stress on this Au-Si mixed layer was found to be significantly reduced and the contrast variation as observed in the amorphous and metastable phases was no longer present. The transformation behavior of the ion-induced amorphous Au-Si alloys described in the above was also observed at room temperature, but during a longer annealing period (several weeks).

5.5 Discussion

5.5.1 Formation Mechanisms of the Amorphous Au_5Si_2 Phase

The observation of a rather uniform layered growth of Au-Si

TABLE V - 2. Observed and Calculated Lattice Spacing For the Ion-Induced Metastable Au_5Si_2 Phase

hkl	d_{cal}* (Å)	d_{obs} (Å)	I_{obs}
110	4.700	4.750	m
112	4.010	4.005	w
004	3.864	3.834	m
202	3.600	3.620	w
203	3.190	3.199	ms
120	3.071	3.080	m
114	2.983	2.989	m
122	2.854	2.841	w
300	2.708	2.700	m
123	2.638	2.645	ms
302	2.556	2.550	w
124	2.404	2.400	m
220	2.345	2.341	m
116	2.258 }	2.260	vs
130	2.253 }		
007	2.208	2.207	m
132	2.163	2.161	s
107	2.131	2 132	m
224	2.005 }	2.006	w
117	1.998 }		
134	1.946	1.953	w
108	1.880	1.903	m
127	1.793	1.798	m
226	1.734	1.725	w
136	1.696	1.693	w
109	1.680	1.673	w
128	1.635	1.642	vw
119	1.613	1.611	m
2o9	1.582	1.580	w

* Calculated from a = 9.382 Å, c = 15.459 Å, hexagonal structure.

amorphous alloy (Fig. 5.1) and a growth rate proportional to the square root of ion dose (Fig. 2) are intriguing. They are quite different from thermal annealing of Au films on Si near or above the eutectic temperature where no amorphous phases were observed and the interface reaction was not uniform [8-10]. So far, amorphous alloys of Au-Si have only been formed by rapid quenching from the melt (including laser melt quenching) or by vapor deposition.

One possible mechanism for the formation of amorphous phase is that a local melting may occur near the Au-Si interface caused by the energetic ions and the melt is quenched instantaneously into the amorphous. This postulation seems consistent with the thermal spike model [11], which predicts a high local lattice temperature (maybe above the Au-Si eutectic temperature 370°C) and a very short lifetime (10^{-10} - 10^{-12}sec) so that a quenching rate of about 10^{12} K/sec can be achieved.

However, the melting (or thermal spike) model cannot satisfactorily explain some experimental results. First, the composition of the ion-induced amorphous alloy, Au-28.5 at.% Si, is different from that of the eutectic point, ∿18 at.% Si. If melting actually occurs, the compositions of the melt and the consequential amorphous phase should be most likely related to the eutectic composition. Secondly, bombardment with light ions (Ar^+, Ne^+) produce qualitatively similar results (i.e., uniform mixture and amorphous phase) as obtained by using heavy ion (Xe^+) except for the difference in ion dose. This will be difficult to explain on the basis of the thermal spike model because the deposited energy density for Ne^+ is much smaller than that for Xe^+

(0.8 eV/atom for 300 keV Xe^+ in Au and 0.8×10^{-3} eV/atom for 200 keV Ne^+ in Au [12]). One would expect that melting (or spike) would not occur for the Ne^+ implant and the interface reaction will not be uniform. Moreover, by reducing the substrate temperature during bombardment one would expect a significant change in the amount of reaction due to the melting-nonmelting transition [13]. On the contrary, the results shown in Fig. 5.3 indicated only a slight reduction in the amount of reaction and a gradual change in the shape of the Au-Si mixture.

The mechanism we propose is that formation of uniform Au-Si mixture is due to a beam-enhanced interdiffusion mechanism as suggested by the square root dependence of reaction on ion dose shown in Fig. 5.2. With this mechanism, the formation of Au_5Si_2 is similar to the formation of Pt_2Si, Ni_2Si, etc. in the silicide forming systems (Chapter 2, Section 2.4.1). Initially, the Au-Si interface is disturbed as a result of dynamic collision cascades generated by the incident ions (cascade mixing) [14-15]. Further interdiffusion of atomic species within the cascade volume can be promoted due to the presence of bombardment induced defects. This will result in the formation of the Au_5Si_2 phase because the results shown in Fig. 5.4 indicate that it is the favorable compound to form. In other words, formation of the metastable crystalline Au_5Si_2 phase is energetically favorable compared to a mixture consisting of randomly distributed Au and Si atoms (an amorphous phase) which is in a high energy state. However, the crystalline structure of

this Au_5Si_2 phase is destroyed under successive ion bombardment, resulting in the formation of an amorphous phase. We have found that the crystalline Au_5Si_2 phase was very sensitive to radiation damage [16]. Recovery of crystalline structure can be achieved by thermal annealing so that no compositional change was observed before and after heat treatment for samples implanted at room temperature.

Based on this model, the slight decrease in the reaction and the less uniform mixtures observed for the lower temperature implants (Fig. 5.3) can be expected because the atomic mobility (or diffusivity) is lower at low temperature. The interface mixing observed at low temperature is predominantly dominated by dynamic cascade mixing. Phase formation is less likely due to the lack of long range atomic mobility at low temperature. Upon post-annealing, nucleation and growth of the crystalline Au_5Si_2 phase can take place along with some redistribution of atomic species within the mixed layer. A uniform layered structure is formed as shown in Fig. 5.4. On the other hand, light and heavy ions should produce similar results except that light ions deposit less energy in the interface region and, hence, the amount of reaction should be smaller (Fig. 5.2). Similar ion dose and ion mass dependences as shown in Fig. 5.2 have also been observed in our previous experiment on ion-induced formation of the Pt_2Si phase (an equilibrium phase) by bombarding through a thin Pt film on a Si substrate [17]. It is plausible that cascade mixing and beam-enhanced diffusion are the dominant mechanisms for the interface mixing in both Au/Si and Pt/Si systems and the different structures (amorphous Au_5Si_2

and crystalline Pt_2Si) observed are due to the differences in the stability of phase structures under ion bombardment.

5.5.2 Comparisons Between Ion-Induced and Liquisol-Quenched Au-Si Alloys

The ion-induced amorphous Au-Si alloy and metastable phase exhibit a silver color similar to that of alloy obtained by rapid quenching techniques. In addition to the color change, the alloyed layers may have a high density. This will presumably induce a high stress between the high density alloyed film and the low density Si substrate underneath, which can cause a density variation in the thin foils as shown in Figs. 5.9b and 5.9c. Release of stress can be accomplished by transformation into the equilibrium state (Au and Si mixture) which has a lower density (and hence larger volume). The early stage of this transformation was found to occur predominantly near the imperfections of the films, such as pinholes or scratches because those are the regions which can accommodate the large volume increase during the decomposition.

Despite the similarities mentioned above, there are, however, some differences between the ion-induced and quenched alloys. The most distinct difference is that the ion-induced amorphous Au-Si alloy is relatively stable (with T_c, transformation temperature, $\simeq$ 80 - 100^oC in comparison with the liquisol-quenched amorphous alloys which were found to transform spontaneously at room temperature [2,5,18]. The transformation temperature of the laser-melt quenched Au-Si alloys

is about 60^oC [4], slightly lower than that in the present case.

Chen and Turnbull (1968) have studied the thermal decomposition of the splat-cooled $Au_{0.77}Ge_{0.136}Si_{0.094}$ amorphous alloy and found that the rate of thermal transformation (from amorphous to crystalline) scaled roughly with the viscosity of the alloys near glass transition temperature [18]. The viscosity reported in their paper was described by a Fulcher-Vogel type equation, $\eta = A\exp[B/(T - T_0)]$, with an apparent activation energy ($\Delta H_\eta \equiv R[d\ \ln \eta/d(1/T)]$) decreasing with increasing temperature from 114 to 62 kcal/mole over the experimental range ($12^oC - 35^oC$). Extrapolation of their results to higher temperatures gives 25 - 21 kcal/mole of apparent activation energy in our experiments ($85 - 101^oC$). The qualitative agreement between the apparent activation energy of τ (25 kcal/mole, Fig. 5.8) and viscosity suggests that the crystal growth rate in our system is viscosity limited [19].

According to the free volume theory developed by Turnbull and Cohen[20], plastic flow in amorphous materials requires a cooperative motion involving local free volume. In the Fulcher-Vogel equation the temperature-dependent term $\exp[B/(T - T_0)]$ is inversely proportional to the free volume concentration and the prefactor A is inversely related to the jump frequency of free volume. We speculate that the presence of implanted species (less than 0.5 at.%) do not significantly change the concentration of free volume but may reduce the frequency of rearrangement. This will reduce the glass flow rate (or cause an increase of

viscosity), and hence, stabilize the glass [21]. If these assumptions are accepted, the extrapolation of activation energy (which depends only on the temperature-dependent term in the F-V equation) in our experiment will be valid. The impurity effects described in the above are consistent with the experimental observation that the transformation temperature is dependent on implanted ion species and ion doses (described in the Section 5.3). However, it is possible that the structure of the ion-induced amorphous Au-Si alloy may not be the same as those of alloys produced by rapid quenching techniques and the stability of amorphous alloy may be dependent on the detailed atomic arrangement (i.e., short-range order) of the amorphous structure.

The crystal structures of Au-Si silicides obtained by rapid quenching techniques or by thermal annealing of thin Au films on crystalline Si have been studied by many investigators. No general agreements were obtained and more than seven different structures have been assigned [1,9,10,22-25]. The composition and crystal structure of the Au-Si metastable phase we observed do not agree with those previously reported results. The selected crystallographic data of Au-silicides studied so far are summarized in Table V-3, which strongly suggests the existence of many structures according to the formation conditions. It is worthwhile to point out the electrons/atoms ratio for Au_5Si_2 is 1.86, a value that, according to Hume-Rothery's empirical rule, should correspond to an electronic compound with hexagonal crystal structure. Indeed, the x-ray reflection peaks for the Au_5Si_2 phase were found to agree well with those of a hexagonal unit cell. This seems

TABLE V - 3. Selected Crystallography Data of Au-Silicides

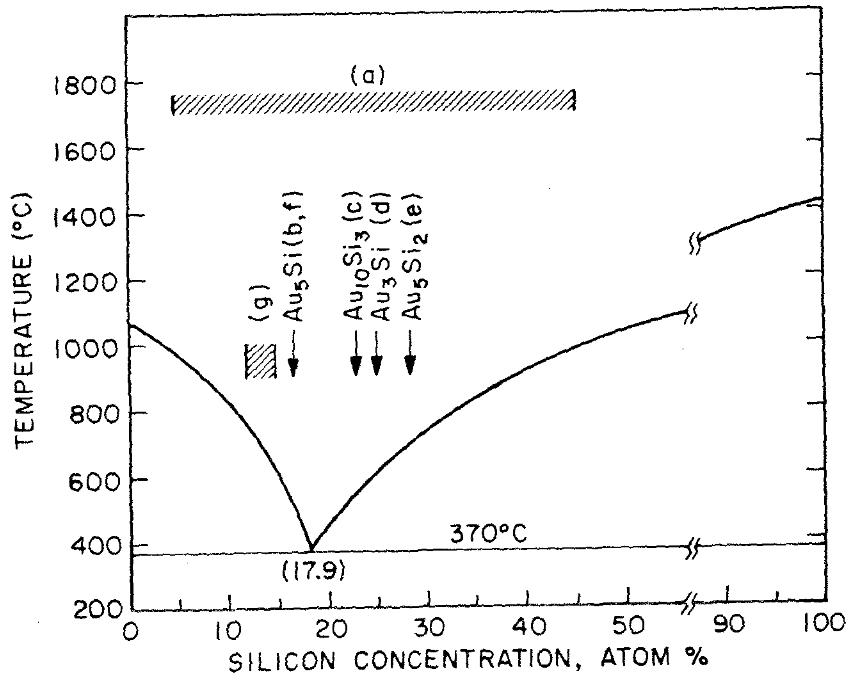

Specimen & author	Structure (type)	Lattice const. (Å)
Quenched film		
(a) Anantharaman et al.	fcc	a = 7.84
	fcc	a = 19.5
(b) Suryanarayana et al.	Cubic (β-Mn)	a = 6.750
(c) Predecki et al.	Cubic (r-brass)	a = 9.60
Krutenat et al.	Cubic (r-brass)	a = 9.60
(d) Anderson et al.	Orthorhombic	a = 7.82, b = 5.55
		c = 11.18
Ion-mixed film		
(e) Present work	Hexagonal	a = 9.38, c = 15.46
Au-Si <111>		
(f) Green and Bauer	Rectangular (LEED)	a = 7.35, b = 9.35
Au-Si<100>		
(g) Oura and Hanawa	Rectangular (LEED)	a = 8.1, b = 9.0
	Hexagonal Ring	a = 4.3

in line with what one would expect based on the fact that hexagonal metastable phases have been observed by rapid quenching from the liquid state in other simple eutectic systems such as Au-Ge, Ag-Ge and Ag-Si [22,24].

5.5.3. Comparisons of Metastable Alloy Formation in the Au-Si and Pt-Si Systems

Although the formation temperatures of the ion-induced metastable Au-Si and Pt-Si phases are quite different (∿100°C for Au_5Si_2, whereas ∿400°C for Pt_2Si_3), the processes involved in the metastable alloy formation, however, exhibit many similarities. In this section, comparisons of results observed in these two systems will be discussed with emphasis on the mechanisms of metastable phase formation. This might provide us some guide lines for further investigation of metastable alloy production in other systems by using ion-beam-mixing techniques.

As shown in Fig. 3.13, the silicon-rich side of the equilibrium Pt-Si phase diagram is a simple eutectic with a eutectic composition (Pt-67.5 at % Si) close to the congruent PtSi phase boundary. This is very similar to the equilibrium phase diagram of Au-Si and other simple eutectic systems such as Au-Ge and Ag-Si, except for a large difference in the eutectic temperature: 979°C for Pt-Si, whereas 370°C for Au-Si. Moreover, the compositions of the metastable Pt_2Si_3 (Pt-60 at.% Si) and Pt_4Si_9 (Pt-69 at.% Si) alloys are quite close to the eutectic composition and a similar correlation is found for the

case of Au-Si. Those similarities seem to suggest that formation of metastable phases may be likely associated with a composition near the eutectic point. It was pointed out by Turnbull and his co-workers [26] that alloys with compositions near deep (or low temperature) eutectic have a larger tendency for glass formation on rapid cooling due to (in part) the reduced melting temperature of eutectic alloys. This argument has been found to be consistent with many experimental observations [26,27]. Transformation of amorphous phase to a metastable crystalline phase might occur if the local atomic concentration is close to the stochiometry of the phase and if the kinetics of transformation to the metastable state is faster than that to the equilibrium structure. These two conditions are fulfilled in both Pt-Si and Au-Si systems as indicated by the transformation behavior shown in the backscattering spectra of Figs. 3.1, 3.2 and 5.4, and the resistivity annealing curves shown in Figs. 4.1 and 5.6.

The most distinct difference in the ion-induced metastable alloy formation between the Au-Si and Pt-Si system is that the Au-Si alloyed layers produced by room temperature ion bombardment are uniform (Fig. 5.1), while the ion-induced Pt-Si intermixed layers are not uniform (Fig. 3.2). We attribute the difference in uniformity to the larger atomic mobility (or diffusivity) of alloys in the Au-Si system than that in the Pt-Si system. This difference in atomic mobility is reflected by the large difference in the amorphous to metastable crystalline transformation temperature as mentioned before. It has been shown in Chapter 2 that the structure and uniformity of the ion-

induced silicide layers are strongly influenced by the implantation temperature. We believe that similar temperature dependences exist for the ion-induced metastable phases since the formation mechanisms are quite similar as discussed in Section 5.5.1. The Au-Si mixed layers produced by R. T. ion bombardment are uniform due to the large atomic mobility in this system. As the implantation temperature decreases, the layers become less uniform similar to the Pt-Si mixed layers produced by R. T. bombardment. Based on this argument, one would expect that uniformly mixed Pt-Si layers might be formed under ion irradiation at elevated substrate temperature. Indeed, we have found that ion-beam mixing of a 300 Å PtSi/Si sample at 250°C resulted in the formation of a uniform Pt-Si mixed layer between Si and PtSi. The average composition of this layer was measured to be close to Pt_2Si_3. X-ray diffraction measurements showed PtSi crystalline reflections (due to the unmixed PtSi) and one faint line which was consistent with the strongest diffraction peak of Pt_2Si_3. It should be pointed out that formation of metastable crystalline phase as a result of ion bombardment does not disagree with the conclusion we have drawn in Chapter 3 that amorphous to crystalline transformation is required to form the metastable phase. This is because formation of crystalline phase is a consequence of structural relaxation of ion-induced mixed layer. The initial structure of this layer is likely to be a mixture consisting of randomly distributed atoms (similar to the amorphous structure) due to the dynamic cascade mixing process. This relaxation process takes place after the dynamic collision

transient and is strongly dependent on the intrinsic atomic mobility of the system and the implantation temperature. A more detailed discussion of this process will be presented in the next chapter.

The comparisons between the Au-Si and Pt-Si system described in the above are mainly concentrated on the mechanisms of metastable phase formation by ion-beam mixing. There are also some differences in the kinetics of phase formation as well as microstructures of the metastable phases in these two systems. A summary of general properties of the Pt_2Si_3 and Au_5Si_2 phases is given in Table V-4.

5.6 Conclusion

In conclusion, an amorphous Au-Si alloy with a composition Au-28.5 at. % Si (Au_5Si_2) has been formed by implanting energetic Xe, Ar or Ne ions through a thin layer of Au deposited on a Si substrate. The ion-induced amorphous Au-Si alloy is uniform in composition and in thickness as indicated by $^4He^+$ backscattering measurement. The Au-Si alloys so obtained are studied by resistivity measurements and by transmission electron microscopy and diffraction. Two distinct stages of phase transformation are observed as revealed by a sudden change of resistivity with increasing annealing temperature. In the first stage, a transformation from amorphous to a metastable crystalline Au_5Si_2 phase occurs in a narrow temperature range around 100^oC. The second state, which appears broader near 180^oC, involves the transformation to the equilibrium two-phase state of Au and Si.

Properties of ion-induced amorphous alloy are quite similar to

TABLE V - 4. General Properties of the Metastable Pt_2Si_3 and Au_5Si_2 Phases

	Pt_2Si_3	Au_5Si_2
Composition and Temperature of the Nearest Eutectic Point	Pt-67.5at.%Si (979°C)	Au-18.0at.%Si (370°C)
Crystal Structure and Lattice Parameters	Hexagonal a = 3.841 Å c = 11.924 Å c/a = 3.104	Hexagonal a = 9.38 Å c = 15.46 Å c/a = 1.65
Space Group of Unit Cell	D^4_{6h}-p6/mmc 10 atoms/cell	-
Amorphous to Crystalline Trans. Temp.	~400°C	~100°C
Metastable to Equilibrium Trans. Temp.	~550°C	~180°C
Activation Energy of Transformation	4.69 eV (376-392°C)	1.1 eV (95-101°C)
Mode of Transformation	t^4	-
Rate Limiting Factor	Nucleation	Viscosity
Morphology	Irregular Crystallite	Lamellar Crystallite
Superconductivity	$T_c \simeq 4$ K	*

\- Not determined

* No evidence of superconductivity down to 1.5K

those formed by rapid quenching of Au-Si except that the ion-induced alloy exhibits a higher stability with respect to the thermal transformation to the metastable crystalline phase. The kinetics of amorphous to metastable transformation has been determined by isothermal treatment over the temperature interval 85 - 101°C. Qualitative agreement was found between the apparent activation energy (25 kcal/mole) of the isotherms and that extrapolated from viscosity previously measured by Chen and Turnbull at lower temperatures (12 - 35°C). It is proposed that the presence of implanted species may reduce the glass flow and, hence, the rate of transformation from the amorphous to crystalline state.

The uniform "layered growth" of the ion-induced Au-Si mixed layers is thought to be most likely due to a beam-enhanced diffusion mechanism, partly assisted by dynamic cascade mixing. The formation of amorphous phase is interpreted as a consequence of losing crystalline structure (of the Au_5Si_2 phase) due to the bombardment damage.

Qualitative comparisons of metastable phase formation in the Au-Si and Pt-Si systems are presented. Emphasis has been placed on the mechanisms of metastable phase formation in an attempt to obtain some insights for further investigation of metastable phase production in other systems. Establishment of ground rules for the production of metastable phases by ion-beam mixing techniques is not complete at the present stage. However, the indications from the Au-Si and Pt-Si systems suggest that metastable phases may be likely associated with compositions near eutectic point. Moreover, substrate temperature

during ion bombardment is important in determining whether metastable phase can be observed directly after ion-beam mixing or that post annealing is required to achieve the metastable state.

References

1. G. A. Anderson, J. L. Bestel, A. A. Johnson and B. Post, Mat. Sci. Eng. 1, 83 (1971).
2. W. K. Klement, Jr., R. H. Willens and P. Duwez, Nature 187, 869 (1960).
3. A. Hiraki, A. Shimizu, M. Iwami, T. Narasawa and S. Komiya, Appl. Phys. Lett. 26, 57 (1975).
4. M. von Allmen, S. S. Lau, M. Mäenpää and B. Y. Tsaur, Appl. Phys. Lett. 36, 205 (1980).
5. H. S. Chen and D. Turnbull, J. Appl. Phys. 38, 3646 (1967).
6. J. Dixmier and A. Guinier, Rev. Metallurgie, 64, 53 (1967).
7. A more detailed description of multiple-layered structure and its application will be presented in Chapter 6.
8. A. Hiraki, E. Lugujjo, and J. W. Mayer, J. Appl. Phys. 43, 3643 (1972).
9. A. K. Green and E. Bauer, J. Appl. Phys. 47, 1284 (1976).
10. K. Oura and T. Hanawa, Surface Sci. 82, 202 (1979).
11. R. S. Nelson, in Ion Implantation, G. Dearnaley, J. H. Freeman, R. S. Nelson and J. Stephen, Eds., (North-Holland, New York, 1973) p. 154.
12. P. Sigmund, Appl. Phys. Lett. 25, 169 (1974).
13. M. W. Thompson, Defects and Radiation Damage in Metals, (Cambridge University Press, Cambridge, England 1969), p. 247; the spike temperature $T_s \equiv T_o + E_o/\frac{3}{2}k$, where T_o is ambient temperature, E_o

the mean energy deposited per target atom and k is the Boltzmann's constant.

14. P. K. Haff and Z. E. Switkowski, J. Appl. Phys. 48, 3383 (1979).
15. H. H. Anderson, Appl. Phys. 18, 131 (1979).
16. Preliminary result showed that bombardment of a ~500 Å crystalline Au_5Si_2 film with a low-dose ($2x10^{14}cm^{-2}$) 300 keV Xe ions has resulted in the formation of an amorphous Au-Si layer. No detectable compositional change was observed by backscattering measurement.
17. B. Y. Tsaur, Z. L. Liau and J. W. Mayer, Appl. Phys. Lett. 34, 168 (1979).
18. H. S. Chen and D. Turnbull, J. Chem. Phys. 48, 2560 (1968).
19. F. Shaepen and D. Turnbull, in Metallic Glasses (A.S.M., Cleveland, Ohio, 1977), p. 114.
20. D. Turnbull and M. H. Cohen, J. Chem. Phys. 34, 120 (1961) and J. Chem. Phys. 52, 3038 (1970).
21. P. Duwez, Private communication, 1979.
22. T. R. Anantharaman, H. L. Luo, and W. Klement, Nature 210, 1040 (1966).
23. R. C. Krutenat, J. K. Tien and D. E. Fornwalt, Met. Trans. 2, 1479 (1971).
24. P. Predecki, B. Giessen and N. H. Grant, Trans. AIME 233, 1438 (1965).
25. C. Suryanarayana and T. R. Anantharaman, Mat. Sci. Eng. 13, 73 (1971).

26. M. H. Cohen and D. Turnbull, Nature 189, 131 (1961).

27. P. Duwez, R. H. Willens and R. C. Crewdson, J. Appl. Phys. 36, 2267 (1965).

28. R. C. Crewdson, Ph. D. Thesis, California Institute of Technology (1966).

Chapter 6
ION-BEAM-INDUCED MIXING OF THIN ALTERNATE LAYERS (MULTIPLE-LAYERS)

6.1 Introduction

Most of the ion-beam mixing experiments discussed in previous chapters were carried out primarily in systems consisting of a thin surface layer on a thick substrate. Those experiments can be considered as mixing with "unlimited supply" of materials in distinction from "limited supply" experiments where samples of thin alternate layers with a fixed composition and a limited amount of materials were used. This is demonstrated schematically in Fig. 6.1. In the unlimited supply experiments ion bombardment can initiate atomic mixing near the film-substrate interface, yet unreacted materials are present in the film and the substrate as shown in Fig. 6.1. The atomic mixing may result in the formation of a compound phase with a composition predominantly determined by the thermodynamic properties of the system. The thickness of the compound layer increases upon ion bombardment but the composition remains unchanged as long as the unreacted materials are still present. This ion-induced compound can be an equilibrium phase as well as a nonequilibrium phase. In both cases, the composition of the phase is "selected" by the system itself.

In the limited supply experiments, the samples are multiple-layers of two elements which are prepared by sequential vacuum deposition of the two components onto inert substrates such as SiO_2 and Al_2O_3. The individual layer thickness is very thin (thinner than that used in the

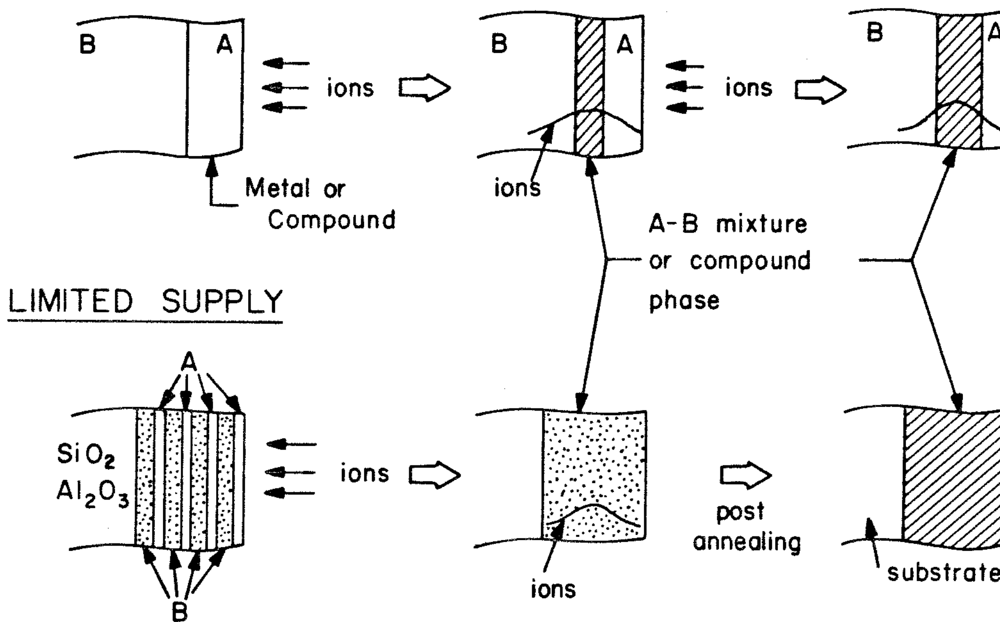

Fig. 6.1 Schematic diagram which demonstrates the ion-beam-mixing experiments with unlimited supply and limited supply of materials. In the unlimited supply experiments the composition of the mixture is "selected" by the system itself, while in the limited supply experiments the composition of the mixture is determined by the sample preparation conditions.

unlimited supply experiments) and the relative thicknesses of those layers are adjusted such that the average film composition is equal to a fixed, predetermined value. Atomic mixing of multiple layers is then initiated by ion bombardment. The discrete structure will be smeared out, resulting in the formation of a uniformly mixed layer with a composition presumably the same as the initial average film composition. In contrast to the unlimited supply experiments where ions penetrate the film-substrate interface, the ion energy used in the limited supply experiments are selected such that the ion penetration depth is approximately the same as the total layer thickness so that the substrate remains roughly undisturbed. In fact, the reason to choose SiO_2 and Al_2O_3 as substrate materials is to minimize film-substrate mixing since they are chemically inert to most of the elements. The substrate serves only as a supporting material for the multiple-layers.

The major difference between unlimited supply and limited supply experiments is that, in the former case, the composition of the mixture (normally a compound) is determined by the intrinsic thermodynamic properties of the system, whereas in the latter case, the composition is forced to a predetermined value. Consequently, the multiple-layered structure is more convenient in producing compounds or alloys of desirable compositions than the single-layered structure. Moreover, atomic mixing can be achieved at low ion doses by using multiple-layered structure because of small film thickness. A thick mixed layer of uniform composition can be produced this way more efficiently than by using single-layer structure.

In this chapter, an example with a V-Si multiple-layer will first be given to demonstrate the feasibility of this scheme in producing the superconducting V_3Si phase. Applications of multiple-layered structures in the Ag-Cu and Au-Co systems are shown next to demonstrate the production of metastable solid solutions over a wide range of composition. Finally, extension of alloy solubilities and formation of amorphous alloys will be shown in the almost completely immiscible systems of Ag-Ni and Cu-Ta, respectively.

6.2 Formation of Superconducting V_3Si Phase

Figure 6.2 shows the backscattering spectra of a V-Si multi-layer sample that has been bombarded with 300 keV Xe^+ to a dose of $4x10^{15}cm^{-2}$ and postannealed at 500^oC for 60 min. The cross sections of the samples have been examined by transmission electron microscopy (TEM) and the micrographs corresponding to the virgin, as-implanted and post-annealed samples are shown in the inset of the spectra. The ripple shape of V and Si signals in the spectrum of Fig. 6.2a represents the alternate V and Si thin layers. The total layer thickness is about 1000 Å. After ion bombardment, the discrete structure of V-Si multilayer is smoothed out, resulting in the formation of a rather uniform V-Si mixture with a composition close to V_3Si (Fig. 6.2b). The structure of this mixture is amorphous as shown by the electron micrography of Fig. 6.2b. Notice that the Xe ion distribution is roughly the same as the total thickness of the multiple-layers and the SiO_2 substrate remains undisturbed as indicated by the sharp signal edge of SiO_2 near channels 230 and 110.

Fig. 6.2 Ion backscattering spectra and cross sectional transmission electron micrographs for a V_3Si multiple-layered sample : (a) unimplanted, (b) implanted with 300 keV 4 x 10^{15} Xe^+ /cm^2 at R.T., (c) post-annealed at 500°C for 60 min. Formation of the superconducting A-15 V_3Si phase is obtained after the annealing with a maximum superconducting transition temperature (T_c) of about 15K.

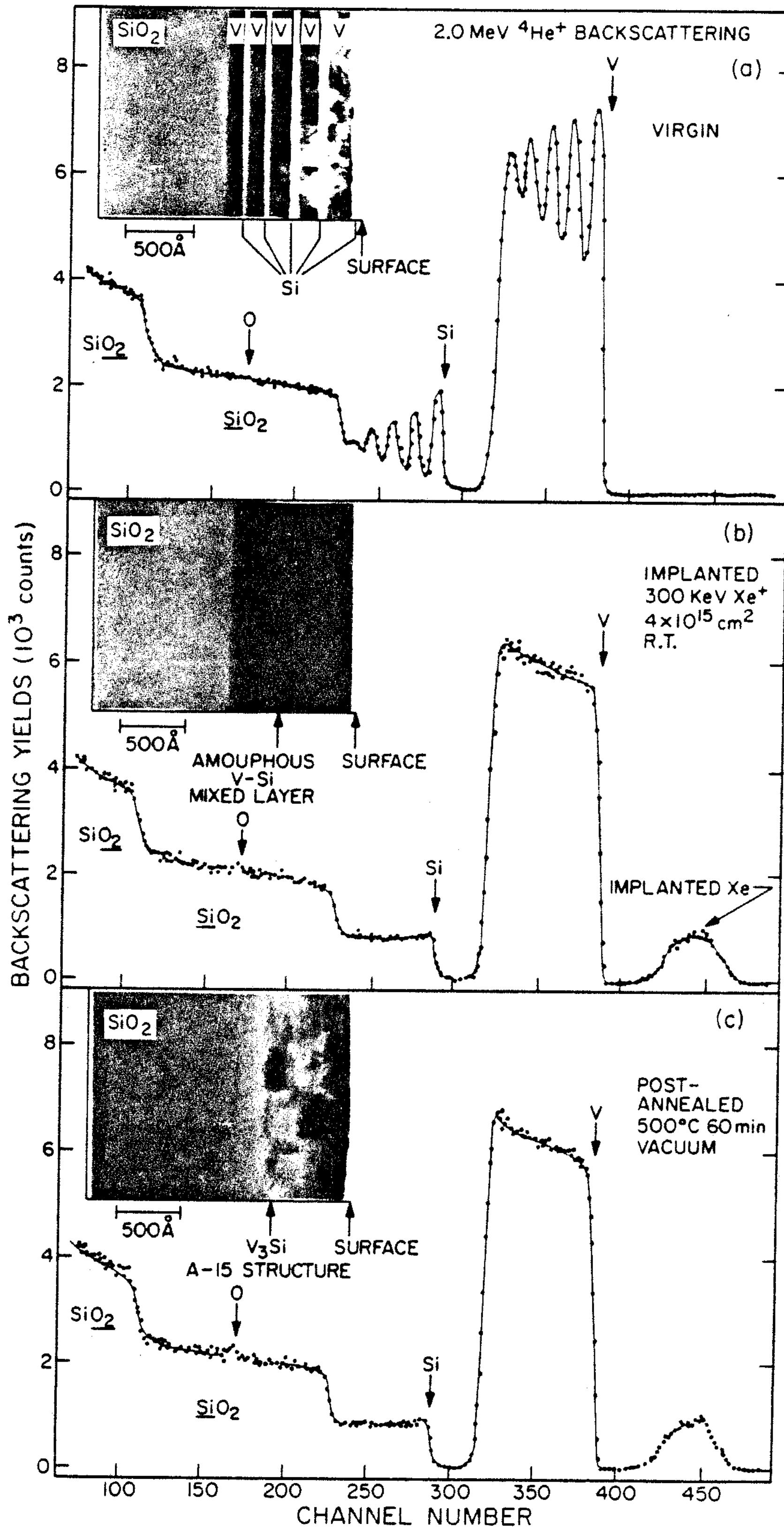

2.0 MeV $^4He^+$ BACKSCATTERING
(a)
VIRGIN
SiO_2
V V V V V
500Å
Si
SURFACE
O
Si
V
SiO_2
SiO_2
(b)
IMPLANTED
300 KeV Xe^+
4×10^{15} cm^2
R.T.
SiO_2
500Å
AMOUPHOUS
V-Si
MIXED LAYER
SURFACE
O
Si
V
IMPLANTED Xe
SiO_2
SiO_2
(c)
POST-
ANNEALED
500°C 60 min
VACUUM
SiO_2
500Å
V_3Si
A-15 STRUCTURE
SURFACE
O
Si
V
SiO_2
SiO_2
BACKSCATTERING YIELDS (10^3 counts)
CHANNEL NUMBER
0
2
4
6
8
100
150
200
250
300
350
400
450

Post-annealing of the implanted sample at $500^{o}C$ for 60 min resulted in a crystallization of the amorphous V-Si mixed layer. No significant compositional changes and redistribution of implanted Xe were observed as shown in the spectrum of Fig. 6.2C.

Identification of the phase structure was performed by using glancing incidence x-ray diffraction and transmission electron diffraction (TED). Both results indicated the presence of a single V_3Si phase with a cubic A-15 structure. Fig. 6.3 shows the bright field TEM image and selected area diffraction (SAD) pattern of the crystalline V_3Si layer. The grain size of polycrystalline V_3Si films is inhomogeneous, ranging from 400 to 2000 Å. Three strongest diffraction lines of the A-15 structure, corresponding to (200), (210) and (211) planes [1], respectively, can be seen clearly in the electron diffraction pattern. The diffuse background in the diffraction pattern may be due to some amorphous V_3Si not completely crystallized or due to a thin layer of amorphous SiO_2 substrate not fully etched away during the preparation of thin foils. The samples have been further heat-treated up to $700^{o}C$ for 2 hrs. No indication of appearance of other phases was observed.

Superconducting transition temperature of those ion-induced V_3Si thin films was measured by using standard four-point probe method. Transition temperature ranging from 11.2K to 15.0K have been obtained. In general, films annealed at higher temperatures exhibit higher T_c presumably due to the growth of polycrystalline V_3Si grains and reduction of defects contained in the materials.

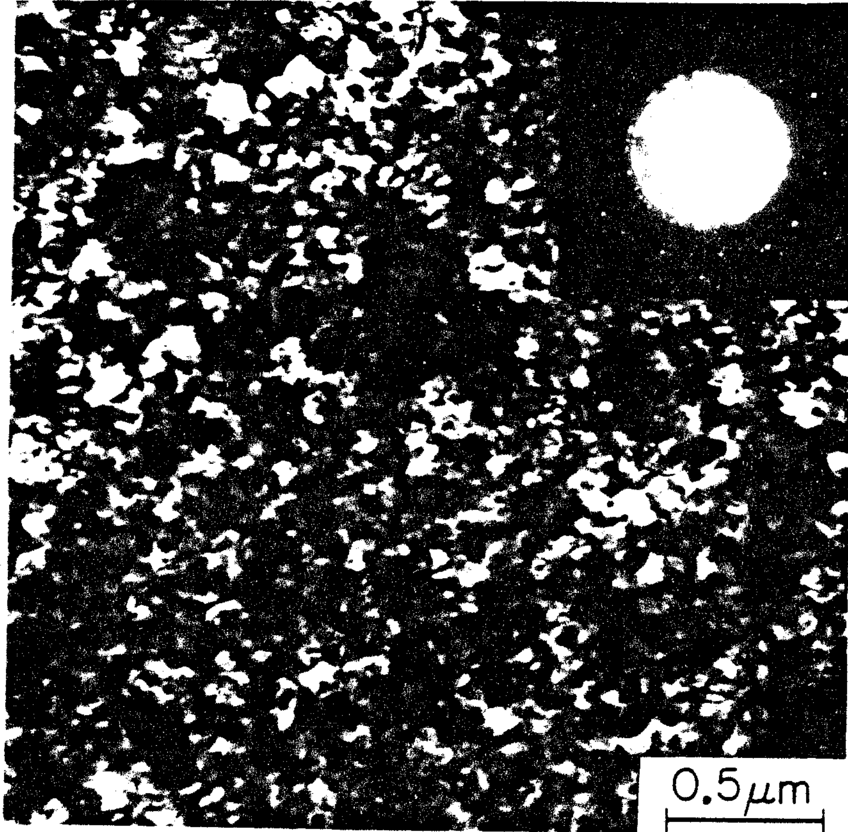

Fig. 6.3 Transmission electron bright field image and selected area diffraction (SAD) pattern for the V_3Si multiple-layered sample bombarded and annealed under the conditions shown in Fig. 6.2. The superconducting A-15 V_3Si phase was detected as indicated in the SAD pattern.

6.3 Formation of Complete Series of Metastable Ag-Cu and Au-Co Solid Solutions

The production of the A-15 V_3Si phase requires post-implantation annealing. Formation of an amorphous V_3Si phase in the as-implanted sample is presumably caused by the bombardment damage. To further study the influences of ion bombardment on the structural modifications of thin deposited layers, experiments with metal-metal couples have been carried out because metals are relatively insensitive to radiation damage. Attention has been directed primarily toward the production of metastable phases. In this section, results obtained with the Ag-Cu and Au-Co systems are presented. These are the two well-known systems where production of metastable phases have previously been studied by many investigators using various techniques. In the next two sections, results on the Ag-Ni and Cu-Ta systems, where less attention has been paid in the past, will be described.

Under equilibrium condition both Ag-Cu and Au-Co systems are simple eutectics (2) with a wide range of miscibility gap in the solid state and no intermediate phases. The noble metals Cu, Ag and Au have f.c.c. structures, while Co has a h.c.p. structure (ε phase) at low temperatures and the f.c.c. Co (α phase) is a high temperature ($\gtrsim 420^{o}C$) modification. According to Hume-Rothery rules of solid solubility (3), Au and Co will not form complete solid solutions because of the different crystal structures and the large differences in electronegativity and atomic radius. The Ag-Cu systems, although satisfying those criteria, is one of the most flagrant exceptions to the rules of solubility. However, it

has been shown that metastable Ag-Cu solid solutions over the entire range of composition can be produced by rapid quenching techniques such as splat cooling [4,5], laser melt quenching [6] and vapor deposition [7]. In the Au-Co system, metastable solid solutions in the range 0 to 49.0% Co-Au have been obtained by liquisol quenching techniques [8], but equilibrium phases (Au and Co rich alloys) were observed for alloys beyond this composition range. In this section, we report production of metastable solid solutions of Ag-Cu and Au-Co over a wide range of composition by using ion-beam-mixing techniques combined with multiple-layered structures.

Fig. 6.4 shows the backscattering spectra of four Ag-Cu multiple-layered samples with various Ag-Cu compositions which have been bombarded with 300 keV Xe ions to a dose of $2x10^{15}cm^{-2}$. The composition of the ion-mixed layer remained the same as the initial film composition. Inspection of those samples with an optical microscope showed the film surface to be quite smooth. No significant beam-induced mixing was found between the SiO_2 substrate and the surface layer as indicated by the sharp Si signal edge near 1.05 MeV.

X-ray diffraction analysis of the ion-irradiated films produced at either R.T. or LN_2 temperature revealed a single phase f.c.c. structure without any traces of the original Ag or Cu reflections. This indicates the formation of supersaturated Ag-Cu solid solutions in excess of the equilibrium solubility limit. In Fig. 6.5, the lattice parameters of the four metastable alloys deduced from angular positions of the f.c.c. reflections were plotted versus concentration. The data points fall

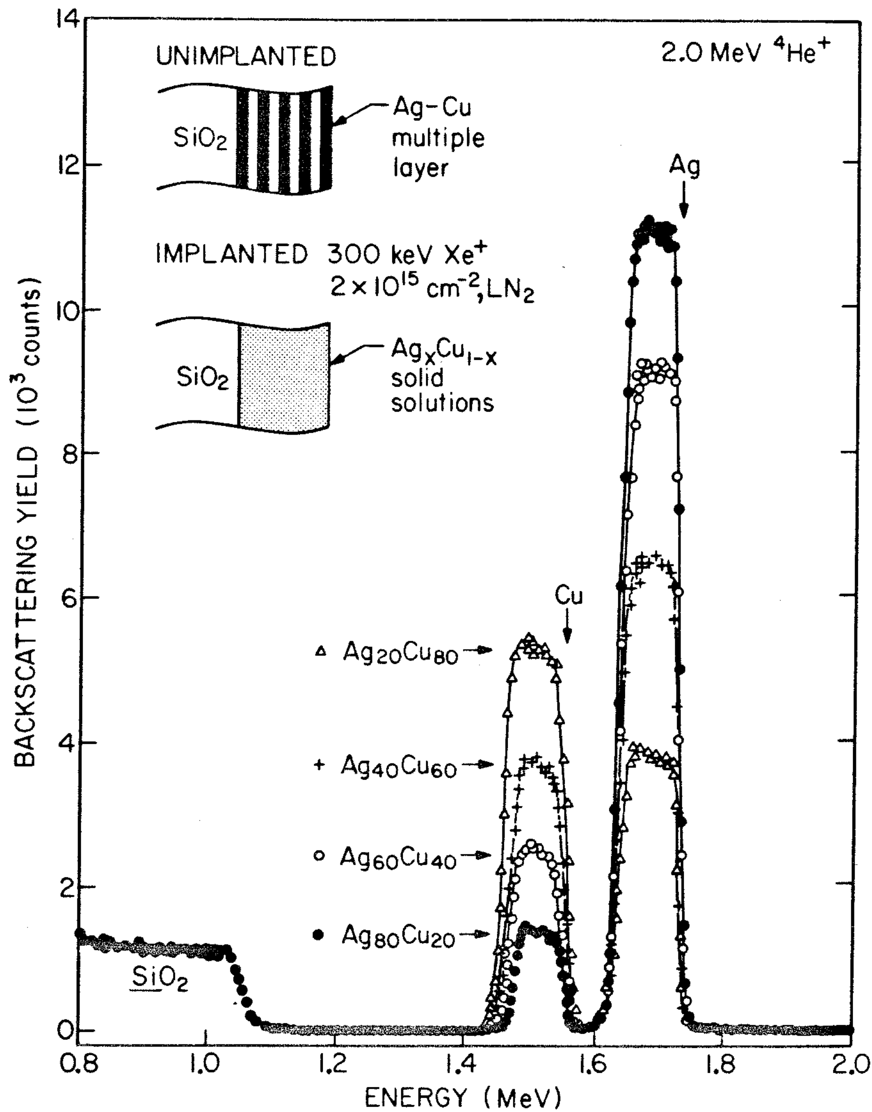

Fig. 6.4 Ion backscattering spectra of four ion-mixed Ag-Cu samples with various compositions. The virgin (unimplaned) samples were multiple-layers of Ag and Cu prepared by sequential vacuum deposition of the two elements onto SiO_2 substrates. The thicknesses of the layers were adjusted such that the average film composition varied between $Ag_{20}Cu_{80}$ and Ag_{80} Cu_{20}.

on a smooth curve connecting the boundary points for elemental Ag and Cu. The maximum deviation from linearity (the Vegard's law for ideal solid solutions) was less than 1% at bout 50 at.% Ag. These results agree well with those obtained previously by splat cooling [5,9] and laser melt quenching [6] techniques.

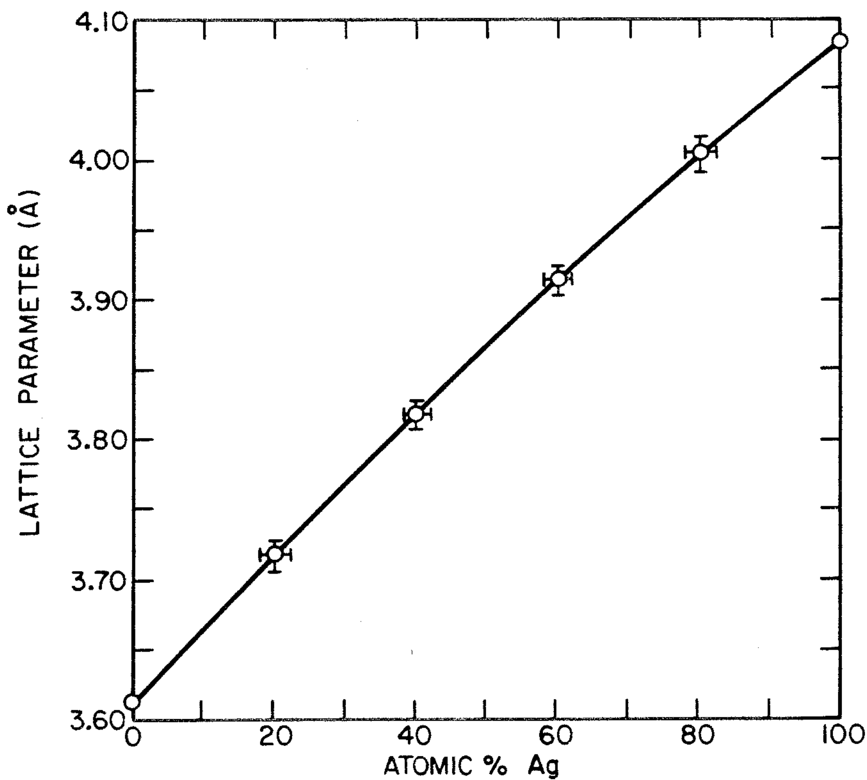

Figure 6.5 Lattice parameters of the ion-induced metastable Ag-Cu solid solutions versus alloy compositions. The maximum deviation from linearity (Vegard's law) is about 1%.

The thermal stability of the ion-induced metastable Ag-Cu alloys was studied by resistivity measurements between R.T. and 250°C under a constant temperature rise of about 2 - 3°C/min. The metastable phases transformed into an equilibrium two-phase mixture of Ag and Cu at temperatures between 160 and 180°C as indicated by a gradual decrease of resistivity. After decomposition, the resistivity increased linearly, showing a positive temperature coefficient of $\sim 4 \times 10^{-3}\ {}^{o}C^{-1}$ and a reversible behavior with changing temperature. This temperature coefficient is quite close to that for elemental Ag (or Cu) at 200°C [10].

The microstructures of the ion-induced alloyed layers before and after annealing were studied by transmission electron microscopy. Fig. 6.6 shows typical electron micrographs and diffraction pictures of Ag-40 at.% Cu alloy films. The diffraction pattern for the ion-irradiated film (Fig. 6.6a) reveals a single-phase f.c.c. structure with a strong preferred orientation where most Ag-Cu crystals have a (111) plane parallel to the film surface. Average grain size is about 1000 Å. Higher magnification image revealed a high density of point defects in the grains, which may cause the broadening of rings in the diffraction pattern of Fig. 6.6a. Fig. 6.6b represents the films after a complete annealing cycle (up to 250°C). A sequence of lines due to both Ag and Cu appear in the diffraction pattern. The lines show a slight arcing due to the (111) preferred orientation of the Ag and Cu crystals, but the texture is much less pronounced than that of the single-phase solid solution. The micrograph shows grains of the two components which are about equal in size (∼2000 Å).

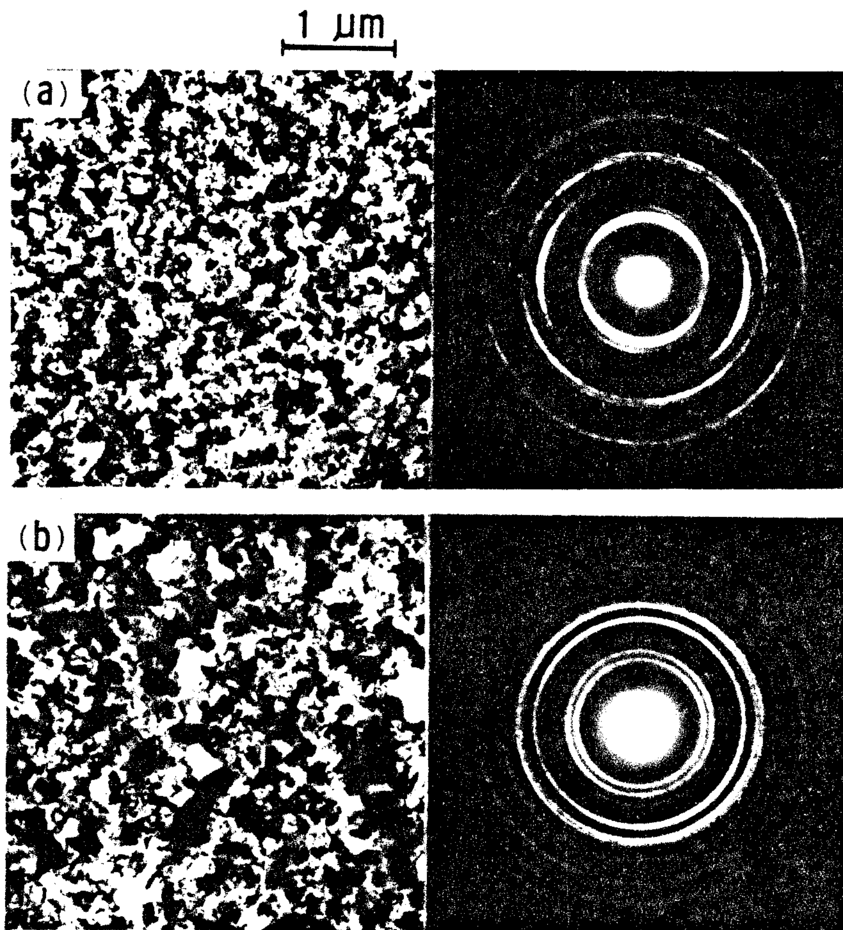

Fig. 6.6 Transmission electron micrographs and diffraction patterns from a film of Ag-40 at.% Cu : (a) after ion bombardment at LN_2 temperature and warmup to room temperature, metastable f.c.c. solution, (b) after heating to 250°C, equilibrium two-phase Ag and Cu mixture.

In the Au-Co system, the structure of the ion-induced alloys was found to vary with composition and implantation temperature. Table VI-1 summarizes the results of x-ray diffraction analysis for three Au-Co multiple-layered samples which have been bombarded with 300 keV $3x10^{15}$ Xe^+/cm^2. All the samples irradiated at R.T. and exhibited a single phase f.c.c. structure with strong (111) preferred orientation. For samples irradiated at LN_2 temperature, the structure of the alloy depends on the composition. For Au-25 at.% Co alloy, the structure is the same as that of the alloy formed by R.T. implantation, but with a slightly weaker (111) preferred orientation. As the Co concentration increases, the structure becomes increasingly more random. The Au-5 at.% Co alloy shows no special preferred orientation and an amorphous structure was found for the Co-rich alloy. In Fig. 6.7, the lattice parameters of the ion-induced Au-Co alloys (obtained by R.T. ion implantation) are plotted versus alloy composition. Again, a slight positive deviation from Vegard's law is observed.

The annealing behavior of the amorphous Au-75 at.% Co alloy have been studied by resistivity measurements under a constant temperature rise of 2-3 $^oC/min$. The result is shown in Fig. 6.8. Two distinct states of transformation were observed as revealed by a sudden change of resistivity with increasing annealing temperature. In the first stage, a transformation from the amorphous to a metastable crystalline f.c.c. solid-solution occurs in a narrow temperature range around 200^oC. The lattice parameter of this metastable f.c.c. solution was measured to be the same as that of the Au-75 at.% Co alloy produced by R.T. ion

TABLE VI - 1. Results of X-ray Diffraction Analysis for the Au-Co Multiple-Layered Films Bombarded at Various Temperatures.

Implantation Temperature	$Au_{75}Co_{25}$	$Au_{50}Co_{50}$	$Au_{25}Co_{75}$
R.T.	f.c.c. a = 3.96 Å Strong (111) Texture	f.c.c. a = 3.84 Å Strong (111) Texture	f.c.c. a = 3.70 Å Strong (111) Texture
LN_2	f.c.c. a = 3.96 Å Medium (111) Texture	f.c.c. a = 3.84 Å No Special Preferred Orientation	Amorphous

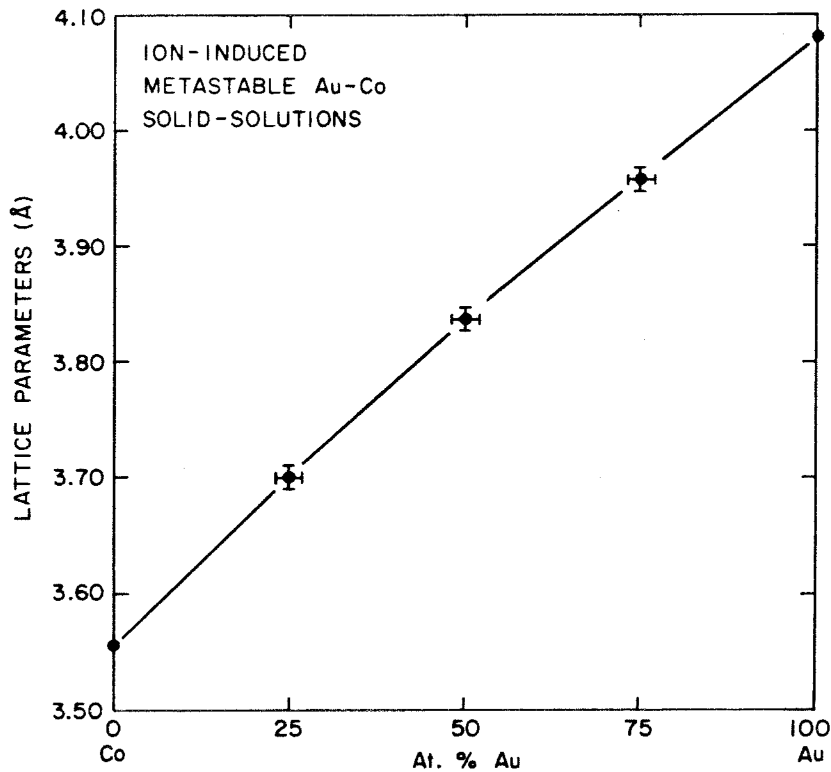

Figure 6.7 Lattice parameters of the ion-induced Au-Co solid-solutions versus compositions.

bombardment. The second stage, which appears broader near 300°C, involves the transformation to the equilibrium two phase states of Au and Co. Reversible annealing behavior with changing temperature was found for the single-phase solid-solution and the two-phase mixture as indicated by $\leftrightarrows$ in Fig. 6.8.

The microstructures of the alloy films at various stages of transformation were examined by transmission electron microscopy and diffraction. Fig. 6.9 shows the bright field micrographs and electron diffraction patterns for the Au-75 at.% Co alloys produced by LN_2 im-

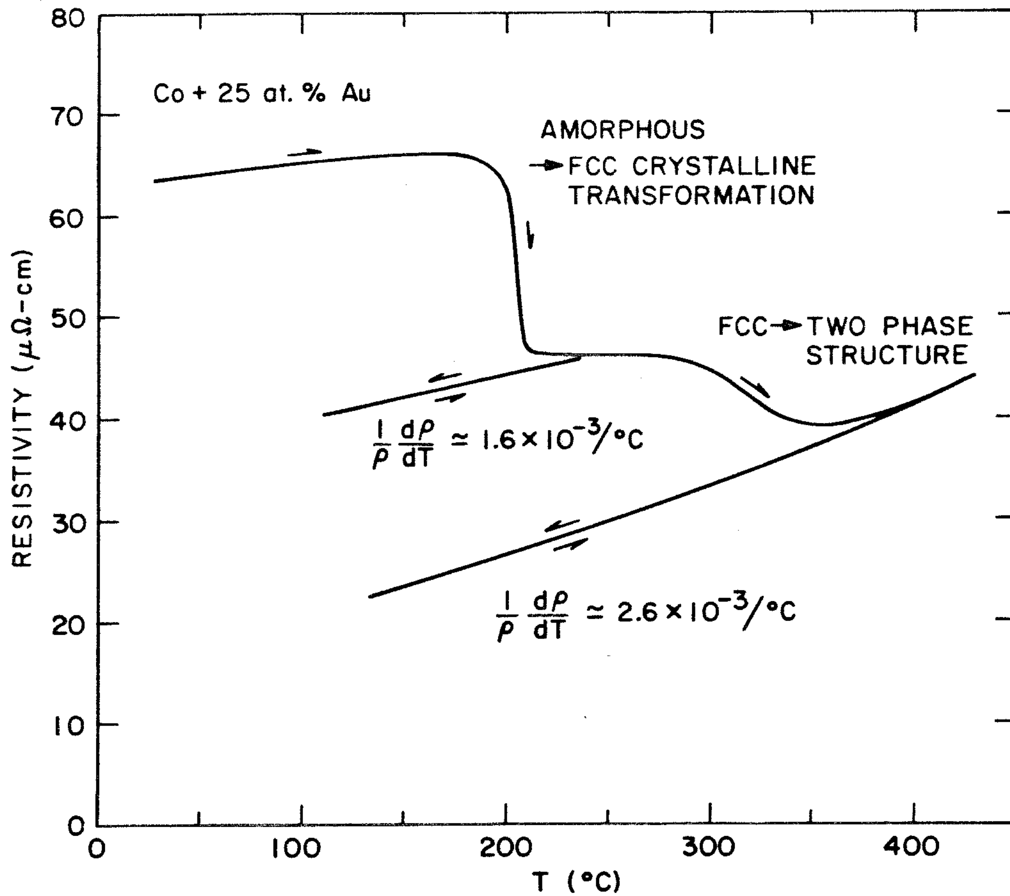

Fig. 6.8 Resistivity annealing curve for the amorphous Au- 75 at.% Co alloy during heating at about 2-3°C/min. The amorphous alloy transforms into a metastable f.c.c. solid-solution at about 200°C, which then gradually decomposes into an equilibrium Au and Co mixture at higher temperatures ~300°C.

plantation. Fig. 6.9a, representing the film after ion bombardment and warming up to room temperature, are typical of an amorphous film. A "particle size" of about 10-15 Å is obtained if one applies the Scherrer formula $C=2\pi/\Delta S$ (where ΔS is the width at half intensity of the Bragg reflections and C is the crystallite size). Fig. 6.9b shows the same film in the metastable crystalline f.c.c. modification after passing through the first annealing stage. The first amorphous halo splits into the (111) and (200) rings and the second halo splits into the (220) and (311) rings. The micrograph shows a fine grained microstructure. Dark field techniques revealed coherently diffracting particles of about 100-200 Å in diameter. Preferred orientation was not detected. Finally, Fig. 6.9c shows the equilibrium two-phase structure after annealing up to 450°C. A sequence of rings due to both Au and Co (f.c.c.) appear in the diffraction pattern. Both phases show a slight (111) preferred orientation.

The result of x-ray diffraction analysis indicates that ion-beam-mixing of thin alternate layers is capable of producing metastable Ag-Cu and Au-Co solid solutions over the entire range of composition. The similarities in the results between the rapid quenching techniques and ion-beam mixing are intriguing as, in the former, quenching starts from the liquid or vapor phase, whereas ion-mixing takes place, basically, in a solid state. We speculate the atomic processes for the formation of metastable alloys by ion beams as following: as energetic ions penetrate into the sample, they experience a series of energy degrading collisions with the host atoms and the kinetic energies are rapidly

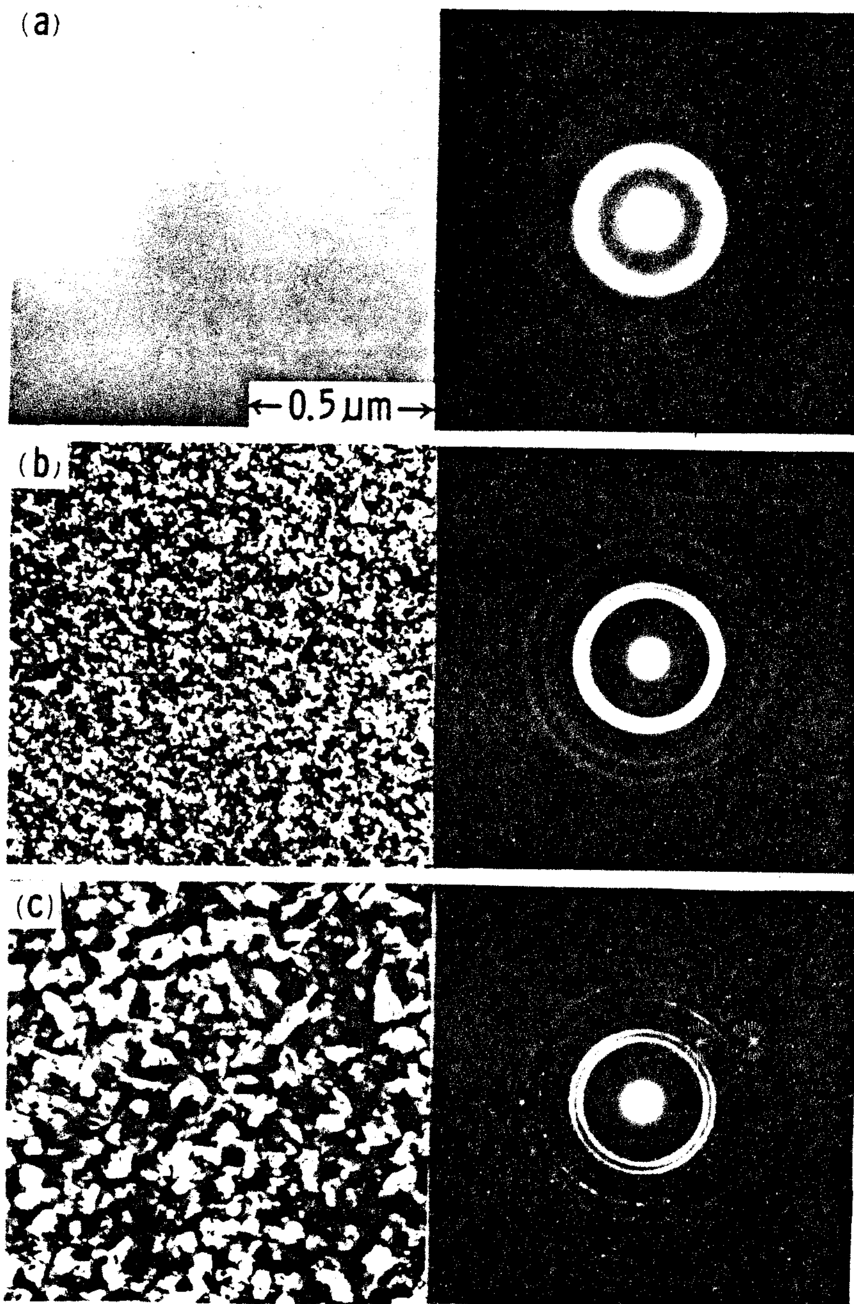

Fig. 6.9 Transmission electron micrographs and diffraction patterns from a film of Au- 75 at.% Co : (a) implanted at 80K and warm up to R.T., amorphous phase, (b) afer heating to 220°C, metastable f.c.c. solution, (c) after heating to 450°C, equilibrium Au and Co mixture.

deposited in a local region surrounding the ion track. As a consequence, the original discrete structure (multiple-layers) is smeared out due to the dynamic collision process and a uniformly mixed layer of Ag-Cu (or Au-Co) is formed. The initial structure of this layer is likely to be a mixture of randomly distributed Ag and Cu (or Au and Co) atoms. However, relaxation of structure may occur after the collision cascade (i.e., during the decay period) via small rearrangement of local atomic positions. This will presumably result in the formation of an ordered crystalline structure (single-phase f.c.c.) because it is energetically more stable than the random configuration. Since the atomic mobility during this relaxation period is strongly influenced by the temperature, one would expect that a relatively more ordered structure may be formed by increasing the substrate temperature during ion bombardment. Indeed, the experimental results showed that the Ag-Cu solid-solutions produced by R.T. implantations exhibited a somewhat stronger <111> texture structure than those formed by LN_2 temperature implantations. This temperature-dependence of structure is clearly demonstrated in the experimental observations in the Au-Co system: whereas the ion-mixed Au-75 at.% Co alloy showed a single-phase f.c.c. structure under R.T. ion bombardment, an amorphous phase was formed if the bombardment was performed at LN_2 temperature.

The origins for the formation of amorphous phase in the alloy of a composition Au-75 at.% Co are not clear. Numerous investigators have noted the enhanced stability of non-crystalline metals when alloyed with other metals or metalloids [11]. Recently, Nagel and Tauc [12], using

a nearly free electron approach, have suggested that this stability is attributed to a shift in the <u>effective valency</u> of the alloy, causing the Fermi level to lie at a minimum of the density-of-states function. Thus, an alloy with concentration of χ of element valency Z_2 in Z_1 should be most stable against crystallization when the effective valency = $1.7 \simeq Z_1(1-\chi)+Z_2\chi$. Substitution of $Z_1 = 1$ for Au and $Z_2 = 2$ for Co gives χ = 70%, similar to the 75% Co in the present case. On the other hand, both elemental Ag and Cu may be taken to have a valency of unity; the effective valency of a Ag-Cu alloy cannot rise above unity for any composition. Therefore, non-crystallinity of the Ag-Cu alloys would not be predicted. Nevertheless, the assignemnt of valences to different elements presents many uncertainties, so that the associated arguments must be treated with caution.

It is interesting to note that vapor-deposition techniques produce amorphous phases when the alloy concentration falls in the range of 35-65 at.% Ag for Ag-Cu and 25-65 at.% Au for Au-Co [7]. The arguments employed by Mader [13] in interpreting the formation and stability of vapor-deposited alloys are based on atomic size considerations: (i) large difference in atomic size leads to a wide compositional range for the stability of amorphous states and (ii) amorphous structure is more favorable for concentrated alloys than for diluted alloys. These results can be expected because alloys produced by vapor-deposition techniques are, basically, constructed layer by layer on atomic basis. This process is very different from liquisol quenching and ion-mixing

techniques in that quenching starts from a mixture of many atoms (in a liquid or a solid state). Consequently, the nearly free electron approach proposed by Nagel and Tauc, which deals with a group of atoms, may not be applicable in the case of vapor-deposited alloys.

Another factor which favors the formation of amorphous phase in the vapor-deposited alloys is that the evaporated atoms, which have small kinetic energy, are mostly frozen in without appreciate atomic movement upon condensation on a cold substrate. However, local rearrangement (or short-range diffusion) of atoms can still occur in the case of ion-beam mixing even at LN_2 temperature due to the relatively high kinetic energy of recoiled atoms and the high mobilities of the defects.

6.4 Extension of Alloy Solubility in the Ag-Ni System

The equilibrium Ag-Ni phase diagram is shown in Fig. 6.10 which indicates a wide range of miscibility gap not only in the solid-state but also in the liquid state [14]. The maximum equilibrium solid solubility is $\sim$0.1 at.% for Ni in Ag near 960°C and $\sim$2 at.% for Ag in Ni near the monotectic temperature 1435°C [15]. Extension of alloy solubility by liquisol-quenching techniques is difficult due to the large liquid-miscibility gap. There are no reports on the vapor-deposited Ag-Ni alloys in the literature. Consequently, the attempt to produce supersaturated Ag-Ni solid solutions by ion-beam-mixing techniques emerges because atomic mixing can be initiated in the solid state regardless of the constraint of liquid immiscibility.

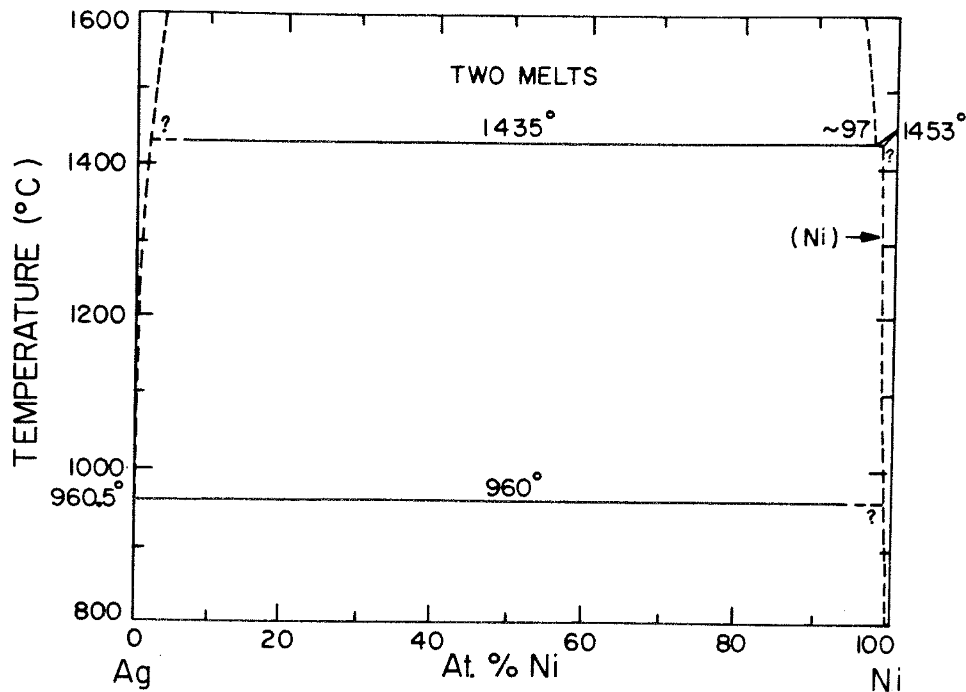

Figure 6.10 Equilibrium Ag-Ni phase diagram (from Ref. 14). Large miscibility gap exists not only in the solid state but also in the liquid state.

Multiple-layer Ag-Ni samples with compositions ranging from Ag-20 at.% Ni to Ag-80 at.% Ni were bombarded with 300 keV Xe^+ to a dose of $3x10^{15}cm^{-2}$. The samples were maintained at three different temperatures -190^0, 25^0 and 250^0C during the implantation. Backscattering measurements showed that uniform Ag-Ni mixed layers were formed after ion-bombardment and the compositions of the mixed layers remained the same as the initial film compositions.

The structures of those ion-induced Ag-Ni mixed layers were analyzed by glancing incidence x-ray diffraction at room temperature. All the

irradiated films showed poly-crystalline diffraction patterns which could be identified to belong to two f.c.c. phases. Fig. 6.11 shows the plot of lattice parameters of the two f.c.c. phases against specimen composition. For comparison, the dashed line for the lattice parameters of ideal solid-solutions (Vegard's law) is also included. The Ag-rich phase has a lattice parameter a = 4.062±0.005 Å, which is slightly smaller than that of a = 4.086 Å for elemental Ag measured from an as-deposited (without ion-bombardment) Ag-Ni film. This phase has been observed in all the implanted samples regardless of alloy composition and implantation temperature. However, the Ni-rich f.c.c. phase shows a variation of lattice parameters with composition and, more significantly, with implantation temperature. For a fixed implantation temperature, the lattice parameter increases with decreasing Ni content and approaches a constant value for the Ag-rich alloys. On the other hand, for a given specimen composition, there is a notable increase of lattice parameter with decreasing implantation temperature as shown in Fig. 6.11. Aside from the change of lattice parameter with implantation temperature, we also observed a change of diffraction intensity of the Ag-rich phase for films irradiated at different temperatures. This effect is illustrated in Table VI-2 where the lattice parameters and intensities of the two f.c.c. phases are shown for the $Ag_{40}Ni_{60}$ films irradiated at -190, 25 and 250°C, respectively. As can be seen in the table, the Ag-rich phase exhibits a constant lattice parameter and the intensity increases with increasing temperature. The

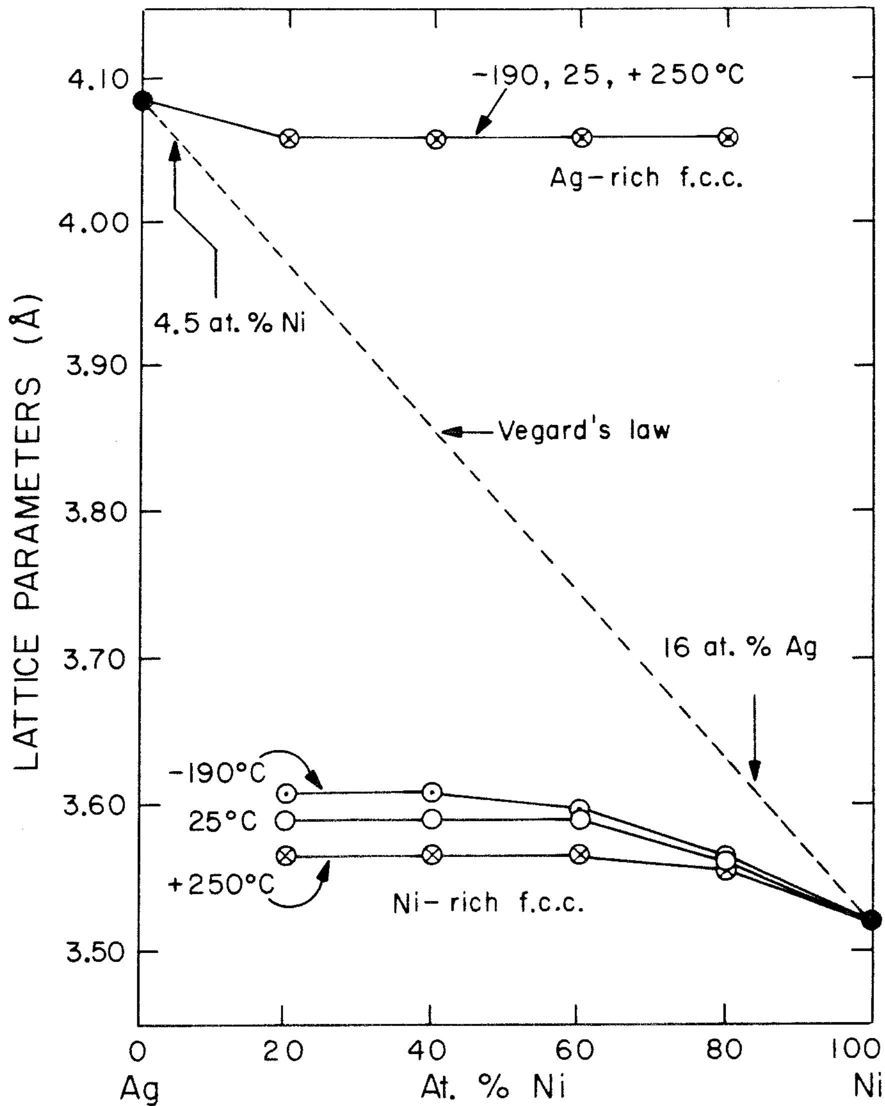

Fig. 6.11 Lattice parameters of the ion-induced Ag-Ni f.c.c. phases as a function of specimen composition. The lattice parameter of the Ag-rich phase is independent of composition and implantation temperature, while the Ni-rich phases show a variation of lattice parameter with composition and temperature.

TABLE VI - 2. Results of X-ray Diffraction Analysis of the $Ag_{40}Ni_{60}$ Films Bombarded at Various Temperatures

Implantation Temperature	Lattice Parameters and Intensities of the Ion-Induced f.c.c. Phases	
	Ag-Rich Phase	Ni-Rich Phase
- 190°C	a = 4.062 Å Medium	a = 3.608 Å Medium
25°C	a = 4.062 Å Medium Strong	a = 3.590 Å Medium
250°C	a = 4.062 Å Strong	a = 3.565 Å Medium

Remarks : a = 4.086 Å for pure Ag.
a = 3.524 Å for pure Ni.

Ni-rich phase, however, shows a gradual decrease of lattice parameter with increasing temperature (Fig. 6.11) but the intensity remains roughly unchanged. Similar trend in the change of intensity and lattice parameter with implantation temperature was observed for alloys of other compositions.

The absence of single-phase metastable Ag-Ni solid-solutions and the absence of amorphous structure in those ion-induced alloyed layers is suggestive of a large tendency for phase separation in this system. Although atomic mixing between Ag and Ni can be induced by dynamic cascade mixing, precipitation of the Ag-rich and Ni-rich phases from the ion-induced Ag-Ni mixture will take place during structural relaxation. This phenomenon seems to be correlated to the immiscible behavior between Ag and Ni (even in the liquid state).

Based on the concept of phase separation, the results of x-ray analysis shown in Fig. 6-11 and Table VI-2 can be rationalized by the following speculations. First, the observation of a constant lattice parameter for the Ag-rich f.c.c. phase independent of composition and temperature is suggestive of a high nucleation (and growth) rate for this phase compared to that of Ni-rich f.c.c. phases. The observed variations of lattice parameters for the Ni-rich phases are presumably caused by the slight changes of nucleation (and growth) rate of the Ag-rich phase with changing alloy composition and temperature. For example, for a given specimen composition, the formation rate of the Ag-rich phase is lower at lower implantation temperature so that the Ni-rich phase would have higher Ag content based on material conserva-

tion. Consequently, the Ni-rich phase observed in the sample implanted at lower temperature exhibits a larger lattice parameter (as shown in Fig. 6.11) because of higher Ag concentration in the phase. This argument is further supported by the intensity observations shown in Table I. The intensity of the Ag-rich phase decreases with decreasing temperature because the amount of the Ag-rich phase is smaller at lower temperature due to a reduction of nucleation (and growth) rate. On the other hand, the intensity of the Ni-rich phase will not change significantly with temperature because the diffraction intensity is mainly determined by the Ni content in the phase.

The exact composition of the Ag-rich and Ni-rich f.c.c. phases are not known. However, if we assume that they are ideal solid solutions, the compositions can then be estimated according to Vegard's law. Extrapolation of experimental data points to the dashed line (Fig. 6.11) gives 4.5 at.% Ni for the Ag-rich phase and a maximum 16 at.% Ag for the Ni-rich phase. The values are substantially greater than the maximum equilibrium solubility limits of Ni in Ag and Ag in Ni.

The stability of the ion-induced supersaturated Ag-Ni solid solutions has been studied by isothermal annealing up to 400°C. No visible changes of x-ray diffraction patterns were observed in films annealed at 300°C for 60 min. After 350°C 60 min. annealing, the Ni-rich phases disappeared along with appearance of crystalline reflections corresponding to pure Ni (strong) and Ag (weak). The diffraction lines due to the Ag-rich phase remained, however, unchanged. For films annealed at 400°C for 60 min., x-ray diffraction patterns showed

reflections due to pure Ni and Ag only. This result indicates that the ion-induced Ag-Ni f.c.c. alloys are supersaturated metastable solid solutions.

6.5 Formation of Amorphous Cu-Ta Alloys

The mutual solubility between Cu and Ta is almost zero in both solid and liquid state [16]. Productions of nonequilibrium Cu-Ta phases by liquisol-quenching techniques have not been attempted in the past due to the liquid-immiscibility. Recently, it was shown that amorphous Cu-Ta alloys can be obtained by direct ion implantation of Ta^+ in Cu at concentrations greater than 10 at.% Ta [17]. To test the possibility of metastable phase formation by ion-beam-mixing, we have carried out experiments using Cu-Ta multiple-layers and the results are described briefly in the following.

The sample preparation procedures and implantation conditions are similar to those for other systems described in the above. The results of x-ray diffraction analysis for four Cu-Ta samples bombarded at -190, 25 and 200^oC, respectively, are summarized in Table VI-3. Amorphous phases were observed for alloys with Ta concentrations greater than 25 at.%. The $Cu_{90}Ta_{10}$ alloys showed predominantly Cu (f.c.c.) reflections; amorphous phase was not detected or its amount was too small to be detected by our technique. The intensity variations for the Cu (f.c.c.) reflections observed for samples ($Cu_{90}Ta_{10}$ and $Cu_{75}Ta_{25}$) implanted at different temperatures can be again explained due to a large tendency for phase separation in this system. The

TABLE VI - 3. Results of X-ray Diffraction Analysis for the Cu-Ta Multiple-Layered Films Bombarded at Various Temperatures

Implantation Temperature	$Cu_{90}Ta_{10}$	$Cu_{75}Ta_{25}$	$Cu_{50}Ta_{50}$	$Cu_{25}Ta_{75}$
- 190°C	Cu(f.c.c.) Weak	Amorphous + Cu(f.c.c.) Very Weak	Amorphous	Amorphous
25°C	Cu(f.c.c.) Medium	Amorphous + Cu(f.c.c.) Weak	Amorphous	Amorphous
200°C	Cu(f.c.c.) Strong	Amorphous + Cu(f.c.c.) Medium	Amorphous + Cu(f.c.c.) Weak	Amorphous

intensity of Cu (f.c.c.) is stronger at higher implantation temperature presumably because of the enhanced nucleation (and growth) rate of Cu at higher temperature. Phase separation can be slightly reduced by lowering the sample temperature during implantation.

6.6 Summary

In summary, by using ion-beam-mixing techniques combined with multiple-layered structure, we have produced a thin film superconducting V_3Si phase (with T_c comparable to that of bulk alloy), as well as a variety of metastable phases. Metastable Ag-Cu and Au-Co solid solutions over the entire range of composition can be achieved this way and the results are either comparable (in the case of Ag-Cu) or superior to (in the case of Au-Co) those obtained by conventional splat-cooling techniques. In addition, extension of alloy solubilities and formation of amorphous phases have been obtained in the almost completely immiscible systems of Ag-Ni and Cu-Ta, respectively. The liquid-immiscibility, which sets a strict restraint on producing metastable phases by rapid quenching from a liquid state, can be overcome in the present case because atomic mixing takes place in the solid state. The present results strongly suggest that the ion-beam-mixing process may promise to be a potential scheme for exploiting metastable phases, which are difficult to form or inaccessible by conventional rapid quenching techniques.

References

1. ASTM card No. 8-347.
2. M. Hansen, Constitution of Binary Alloys, (McGraw-Hill, New York, 1958), p. 18 and 195.
3. W. Hume-Rothery, R. E. Smallman, and C. W. Haworth, The Structure of Metals and Alloys (Institute of Metals, London, 1969).
4. P. Duwez, R. H. Willens, and W. Klement, Jr., J. Appl. Phys. 31, 1136 (1960).
5. N. Nagakura, S. Toyama, and S. Oketani, Acta. Met., 14, 73 (1966).
6. W. A. Elliott, F. P. Gagliano, and G. Krauss, Metall. Trans. 4, 2031 (1973).
7. S. Mader, A. S. Nowick, and H. Widmer, Acta Metall. 15, 203 (1967).
8. W. Klement, Trans. Met. Soc. AIME 227, 965 (1963).
9. R. K. Linde, J. Appl. Phys. 37, 934 (1966).
10. Handbook of Chemistry and Physics, 44th Edition (Chemical Rubber Publishing Co. 1961), p. 2674.
11. G. S. Gargill III, in Solid-State Phys. 30, 227 (1975).
12. S. R. Nagel and J. Tauc, Phys. Rev. Lett., 35, 380 (1975).
13. S. Mader, J. Vac. Sci. Technol. 2, 35 (1955).
14. Ref. 2, p. 36.
15. G. Tammann and W. Oelsen, Z. anorg. Chem., 186, 264 (1930).
16. Ref. 2, p. 638.
17. A. G. Cullis, J. A. Borders, J. K. Hirvonen and J. M. Poate, Phil. Mag. B 37, 615 (1978).

Chapter 7
IMPLICATION OF ION-BEAM-MIXING TECHNIQUES IN MATERIAL SURFACE MODIFICATION

7.1 Introduction

We have shown in previous chapters that ion-beam-mixing of a thin film and a substrate or a layer containing multiple thin films can lead to the formation of a variety of compounds and alloys. Equilibrium phases as well as nonequilibrium phases such as amorphous alloys and metastable crystalline compounds have been obtained. Those ion-induced alloyed phases may possess unusual physical properties and they may prove to be useful for certain specific applications. Aside from production of metastable phases, we believe that ion-beam-mixing techniques have significant implication in the area of ion-beam material surface modification.

The use of ion implantation as a new method to modify the near-surface region of metals has experienced rapidly growing research interest in the past few years. Considerable attention has been directed toward the modification of physical properties of metals, such as improvements in friction, wear, fatigue and corrosion resistance (1,2) by direct implantation of foreign species into metals. Another aspect is the study of metastable phases in metals by ion implantation (3). Amorphous layers (4) as well as substitutional solid solutions (5) can be formed.

However, from a practical point of view the major drawback to direct implantation is that ion doses greater than 10^{17} ions/cm^2 are

generally required to produce concentrations of implanted ions in excess of a few atomic percents. Aside from the long implantation time, the process is limited by sputtering effects which establish the maximum concentration that can be achieved by implantation [6]. This sputtering limitation sets a strict restraint on using direct implantation to produce high concentration alloyed layers. In order to achieve higher concentrations than those obtained by direct implantation, one can use ion-beams to intermix a thin deposited layer into the underlying substrate. Since low ion doses ($\lesssim 10^{16} cm^{-2}$) are generally required for mixing, as inferred from the results in metal-Si systems, layers of high concentrations may be achieved before reaching the limitation imposed by sputtering at high doses.

In this chapter, we first demonstrate the production of substitutional solid solutions of Au (or Ag) in single-crystal of Cu using ion-beam-mixing techniques. The results are then compared with those obtained previously by direct high-dose implantation. A simple mathematical model for the evolution of ion-beam-mixing of a thin surface layer on a thick substrate will be presented next. The model predicts the influence of implantation conditions and material properties on the redistribution of the thin surface layer. Examples will be given to demonstrate this effect. Finally, the advantages and limitations of using ion-beam-mixing techniques in the area of material surface modification will be discussed.

7.2 Comparisons of Substitutional Au-Cu (Ag-Cu) Solid Solutions Formed by Direct Implantation and by Ion-Beam Mixing

It has been shown that direct implantation of Au or Ag ions into single-crystal of Cu can result in the formation of substitutional solid solutions [7]. A 100% substitutionality was found for both Au and Ag in the Cu crystal as indicated by channeling measurements. Under thermal equilibrium, Au is soluble in Cu, but Ag and Cu, as mentioned in Section 6.3, have very limited mutual solid solubility. The ion implanted Ag-Cu alloys are, therefore, supersaturated metastable solid solutions. However, with Au (or Ag) implantation into Cu at 150 keV, the maximum attainable concentration for random incidence is about 5 at.% at a dose of $1 \times 10^{17} cm^{-2}$ [6]. This concentration is essentially limited by the sputtering process. Implantation with higher energy ions or implantation along a major crystallograph (channeling) axis of the crystal should be used in order to achieve higher concentrations [8].

In Fig. 7.1, we demonstrate that similar results can be obtained by implanting a low dose ($5 \times 10^{15} cm^{-2}$) of Xe ions through a thin Au (or Ag) film deposited onto a single-crystal Cu <110> substrate. The implantations were performed at R.T. with 300 keV Xe ions. Low beam current ($\sim$ 1 μA) was used to avoid beam-heating effect. As can be seen in the spectra, a Au-Cu (Ag-Cu) intermixed layer about 500 - 600 Å thick is formed after ion bombardment. The concentrations of Au and Ag at the peak of the distribution are measured to be 12 at.% and 7 at.%, respectively. From the difference of random and aligned (along

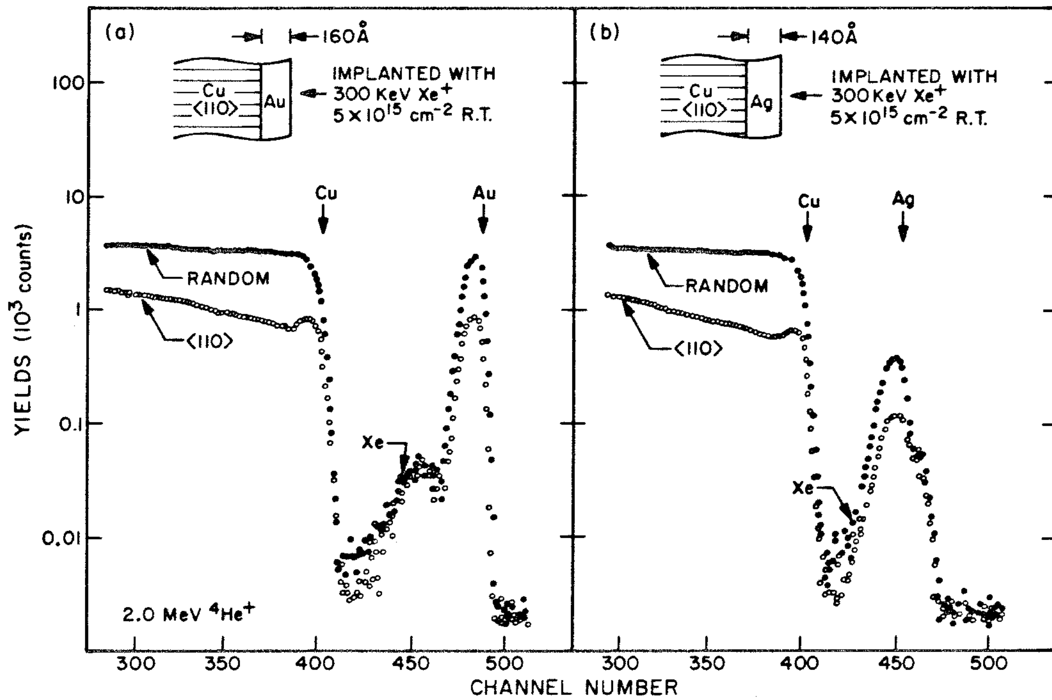

Fig. 7.1 Aligned and random ^{4}He ion channeling spectra for the (a) Au-Cu and (b) Ag-Cu intermixed layers produced by Xe^{+} ion bombardment. Substitutional Au-Cu and Ag-Cu solid solutions are formed. The implanted Xe ions are mainly non-substitutional.

<110> direction) spectra, approximately 96% of the Au and 93% of the Ag were on the substitutional sites of the Cu crystal matrix. A comparison between the present results and those obtained by high-dose implantation is shown in Table VII-1. The most distinct difference is that a much lower ion dose is required with ion-beam-mixing to achieve a relatively higher Au or Ag concentration as compared to high-dose implantation.

In order to achieve concentrations well in excess of those that can be obtained by direct high-dose implantation, experiments with a thicker deposited film (∿300 Å) were performed. We found that the substitutional fraction of Au (or Ag) in Cu was lower than that observed with a thinner film for the same implantation dosage. Increased ion doses led to increased amount of intermixing and hence, decreased concentration of Au (or Ag) in Cu. Fig. 7.2 shows a plot of atomic concentration and substitutional fraction of Au versus ion dose for 160 Å and 300 Å Au films on Cu <110> bombarded with 300 keV Xe ions. For a given film thickness, the concentration of Au decreases with increasing ion dose, while the substitutional fraction increases as the concentration decreases. Notice that a zero substitutional fraction of Au was found for the 300 Å Au film implanted at a dose of $2x10^{15}cm^{-2}$. X-ray diffraction measurements showed the presence of a polycrystalline layer with a single-phase f.c.c. structure. This result indicates that the mixing between the single-crystal Cu and the polycrystalline deposited Au film at low ion doses leads to the formation of a polycrystalline Au-Cu mixed layer. The substitutional

TABLE VII - 1. Comparison of Incorporation of Au and Ag in <110> Cu by High-Dose Implantation and Ion-Beam-Mixing

	High-Dose Implantation	Ion-Beam-Mixing
Au/Cu<110>	Cu<110> ← 150 keV Au^+ Au^+ dose: 1×10^{17} cm^{-2} Maximum Au concentration : 5 at.% (random incidence) Substitutionality: 100% From: Refs. 6 and 7	160 Å Au on Cu<110> ← 300 keV Xe^+ Xe^+ dose: 5×10^{15} cm^{-2} Peak Au concentration: 12 at.% Substitutionality: 96%
Ag/Cu<110>	Cu<110> ← 150 keV Ag^+ Ag^+ dose: 5×10^{16} cm^{-2} Peak Ag concentration: 4.3 at.% (channel implantation) Substitutionality: 100% From: Ref. 8	140 Å Ag on Cu<110> ← 300 keV Xe^+ Xe^+ dose: 5×10^{15} cm^{-2} Peak Ag concentration: 7 at.% Substitutionality: 93%

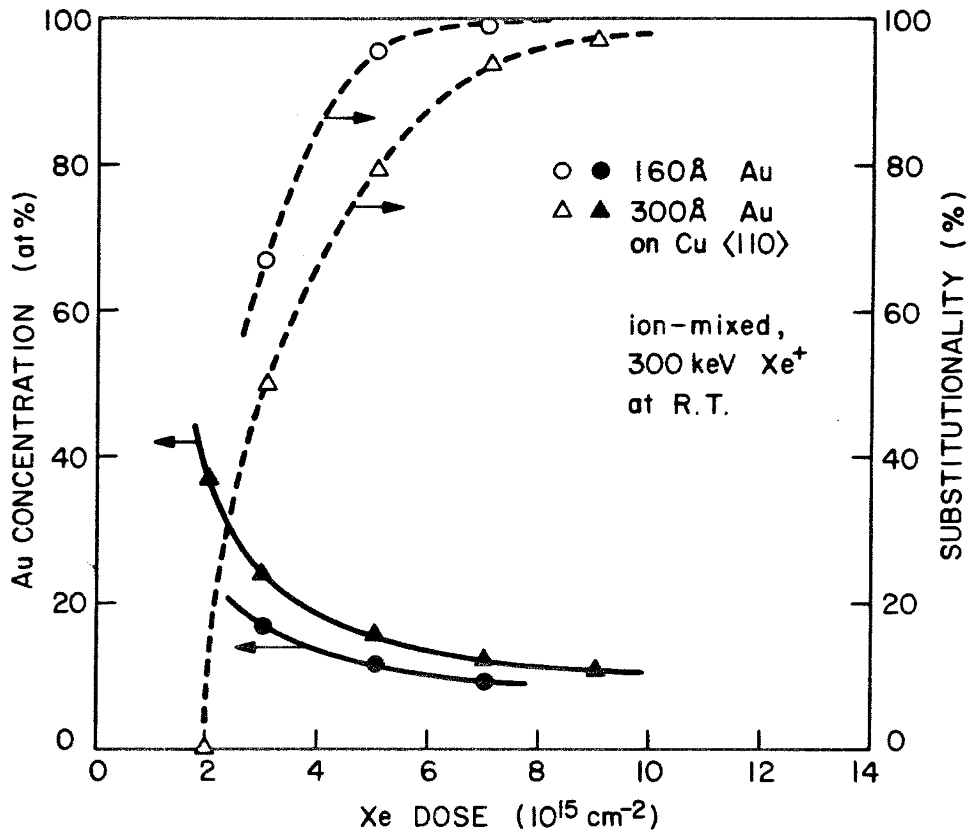

Fig. 7.2 Atomic concentration (left axis) and substitutional fraction (right axis) versus ion dose for two Au films, with different thicknesses, bombarded with 300 keV Xe ions at room temperature.

fraction of Au as determined by channeling measurements is very low ($\simeq$ zero) because of the random nature of the polycrystalline layer. Upon further ion bombardment, Au is mixed progressively into deeper regions of the crystal Cu substrate along with a successive sputter erosion of the initially polycrystalline Au-Cu layer. Consequently, the substitutional fraction of Au increases as the mixing process proceeds. The concentration of the Au-Cu layer is dependent on the initial Au film thickness and the amount of intermixing over the penetration depth of the incident ions.

7.3 Ion-Beam-Induced Mixing of a Thin Surface Film on a Thick Substrate

7.3.1 A Model

In this section, a simple mathematical model for the evolution of ion-beam mixing of a thin surface layer on an infinitely thick substrate is presented. Since we proposed ion-beam-mixing as an alternative approach to direct implantation for material surface modification, it will be essential to be able to estimate the impurity redistribution as a function of ion dose and how this process is affected by the material properties and implantation conditions.

The basic ideal of this model is to consider ion-induced intermixing (or impurity redistribution) as a diffusion process similar to "drive-in" of impurity by thermal diffusion. As mentioned in Section 2.4.3, radiation-enhanced diffusion is believed to be the dominant mechanism for interface mixing at elevated temperatures in metal/Si systems. The enhanced-mixing phenomenon along with formation of well-defined

silicide phases observed at high implantation temperatures occurs because compound formation as a result of atomic interdiffusion during ion bombardment is, basically, a thermally activated process. The present model deals with a system where enhanced mixing due to ratiation-enhanced-diffusion can occur and with a situation where enhanced-diffusion is the dominant mechanism for mixing. For simplicity, we assume that the ion penetration depth is much greater than the thickness of the thin surface layer. This condition can be fulfilled by using energetic light projectiles. With those assumptions, the redistribution of thin surface layers due to ion-beam-mixing can be treated as "diffusion" of an infinitesimal thin surface source into a thick substrate with a constant diffusion coefficient. Mathematically, this is similar to a one-dimensional diffusion problem with a delta function source on the surface. The solution for this one dimensional diffusion problem is a Gaussian distribution [9]

$$C_1(x,t) = \frac{Q_o}{\sqrt{\pi D t}} e^{-x^2/4Dt} \tag{7.1}$$

where D is the diffusion coefficient, t the diffusion time and Q_o the total amount of source material which is taken to be a constant in this solution.

The situation is slightly different in the case of ion-beam-induced diffusion and the above solution shall be modified. First, diffusion

of impurity initiated by one incident ion occurs only in a region surrounding the ion track, i.e., within the dimension of a single-collision cascade. Each incident ion generates a localized reaction, which does not extend over the whole sample area. The impurity profile we observe after many incident ions is an accumulated effect due to many such localized elemental processes. Consequently, a statistical consideration will first be given to account for those elemental processes because of the randomness of incident ions. Secondly, the amount of source material during the mixing process is not conserved due to successive sputter erosion of material on the surface. This effect will be considered later.

The "localization" of the effect of each incident ion has been mentioned before in interpreting the ion-induced interfacial reaction (Section 2.4.1, Fig. 2.2). A somewhat more detailed consideration will be given here. Figure 7.3 shows schematically the evolution of this process. Each incident ion triggers a local region of atomic mixing which results in forming an intermixed region near the surface (Fig. 7.3a). If we assume a diffusion process for atomic mixing, the concentration profile of impurity atoms in this intermixed region will be Gaussian with a characteristic length ℓ. The ℓ is equivalent to $\sqrt{D^*\tau}$, where D^* and τ are effective diffusivity and effective diffusion time in the mixing process. The characteristic length ℓ is a measure of mixing efficiency which is dependent on implantation conditions and material properties. The significances of ℓ will be discussed later.

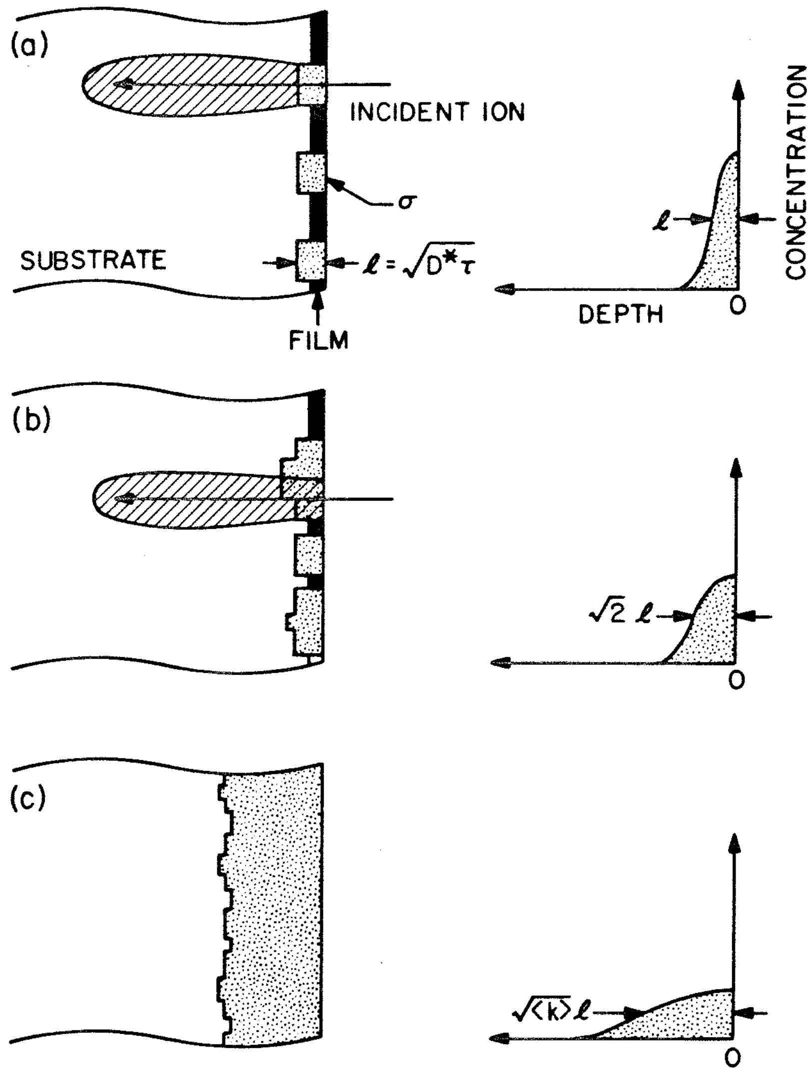

Fig. 7.3 Schematic picture which shows that ion-induced intermixing can be considered as being composed of many localized elemental processes, each initiated by one incident ion. The elemental processes overlap at high ion doses and an intermixed layer with an averaged Gaussian distribution is formed.

As more ions come in, more such intermixed regions are created. The regions are likely to cover the shole surface and an incident ion may therefore impinge on intermixed regions which are already present. We assume that this second collision cascade promotes the intermixing further. The situation is illustrated in Fig. 7.3b, where thicker intermixed regions represent overlaps of effects of two individual ions. The atomic distribution of impurity in the overlapped region will still be Gaussian, but with a characteristic length $\sqrt{2}\ell$. Further ion bombardment will cause more and more overlaps and result in the formation of an intermixed "layer" with an averaged Gaussian profile. The characteristic width of this layer will be equal to $\sqrt{\langle k \rangle}\ \ell$, where $\langle k \rangle$ is the statistical average of the number of overlapping track.

To estimate $\langle k \rangle$, a statistical model is given as follows: For simplicity, we assume the lateral (i.e., parallel to the surface) distribution of intermixing initiated by one incident ion to be uniform with a circular region of area σ (of which the center is the point of ion incidence). The top view of the sample will look like that shown in Fig. 7.4. The size of σ is likely to be related to the lateral extent of a single collision cascade, which in turn depends on ion energy and masses of ion and target materials. We shall take σ as a parameter, but with a much smaller size (say $\sim(100\ \mathring{A})^2$) compared to the sample area A, which is generally $(1\ cm)^2$.

After incidence of N ions, the interesting quantity is the fraction of total area which has been covered exactly k times by those N discs, where k ranges from 0 to N. From a statistical point

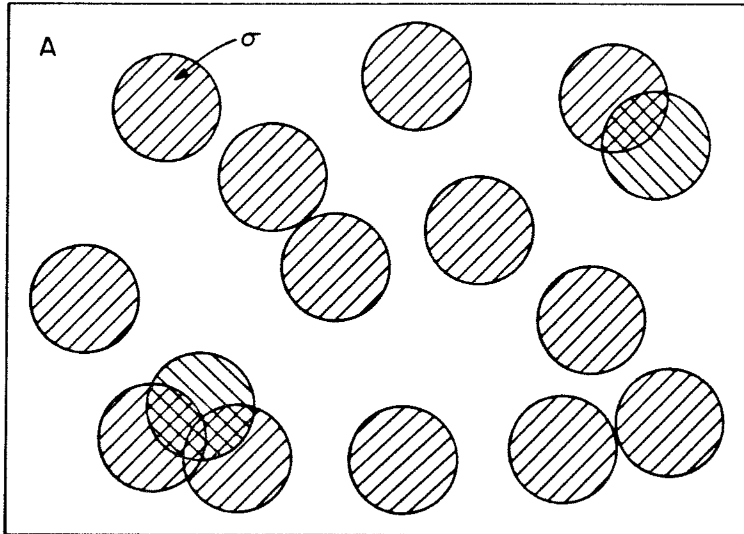

Figure 7.4 Top view of a sample after being bombarded by many ions. Each shaded area represents a reacted region of area σ.

of view, this quantity is equivalent to the probability, P_k, for any given point (in A) to be hit k times after N random incidences of discs onto area A. It can be shown that [10] P_k follows a Poisson distribution

$$P_k = \frac{\left(\frac{N\sigma}{A}\right)^k}{k!} e^{-\left(\frac{N\sigma}{A}\right)} \qquad (7.2)$$

Notice that N/A is equivalent to the ion dose, which is of the order of $10^{15} - 10^{16} cm^{-2}$ for typical ion-beam-mixing experiments. This

will yield $N\sigma/A$ a value in the range of 10^3 - 10^4 (>> 1), which indicates that any point in A will be covered many times and, hence, a statistical average is meaningful. For large $N\sigma/A$, the Poisson distribution will approach a Gaussian distribution [10] with a mean value of k given by $\langle k \rangle = N\sigma/A = \Phi\sigma$. The characteristic width ($= \sqrt{\langle k \rangle}\,\ell$) of the intermixed layer described in the above will be equal to $\sqrt{\Phi\sigma}\,\ell$.

With this, we can write down the impurity distribution function according to Eq. 7.1 with $\sqrt{Dt}$ replaced by $\sqrt{\Phi\sigma}\,\ell$:

$$C_1(x,t) = \frac{Q_o}{\sqrt{\pi\Phi\sigma}\,\ell}\, e^{-\frac{x^2}{4\Phi\sigma\ell^2}} \qquad (7.3)$$

Eq. 7.3 applies in the case where the total amount of impurity is conserved, i.e., sputter erosion of material is neglected. To include sputtering effects, we replace Q_o with a function $Q(\Phi)$, which decreases monotonously with increasing ion dose:

$$C_1(x,t) = \frac{Q(\Phi)}{\sqrt{\pi\Phi\sigma}\,\ell}\, e^{-\frac{x^2}{4\Phi\sigma\ell^2}} \qquad (7.4)$$

This formulation is similar to that of thermal diffusion of a sheet of surface source into a thick substrate, but with simultaneous loss of material (to the ambient) on the surface. The physical picture of Eq. 7.4 can be visualized as follows: sputtering causes a decrease of

total amount of impurity material and the remaining material will then diffuse inward to the substrate. Since sputtering takes place in a very short time period (10^{-13} - 10^{-14} sec, roughly corresponding to the slowing down time of the incident ion) and diffusion usually occurs during a much longer period of 10^{-10} - 10^{-8} sec after the short transient, these two processes can be essentially decoupled. In Eq. 7.4, x refers to the distance from the sample surface which will now recede due to sputtering loss of material. The $Q(\Phi)$ can be derived as follows: The conservation of material requires

$$-\frac{d\,Q(\Phi)}{d\,\Phi} = S_1(\Phi) \qquad (7.5)$$

where $S_1(\Phi)$ is the sputtering yield for the impurity atoms. The S_1 is related to the total sputtering yield S and the surface concentration $C_1(0,\Phi)$ by

$$S_1(\Phi) + S_2(\Phi) = S \qquad (7.6)$$

$$\frac{S_1(\Phi)}{S_2(\Phi)} = \frac{1}{r}\frac{C_1(0,\Phi)}{C_2(0,\Phi)} \qquad (7.7)$$

where $S_2(\Phi)$ is the sputtering yield for the substrate atoms and $C_2(0,\Phi)$ is the surface concentration of the substrate atoms.

Eq. 7.6 states that the total sputtering yield is constant, which has been found to be a good approximation for sputtering of binary compounds and alloys [11]. Eq. 7.7 relates sputtering yield of each

element in a two-component system to its surface concentration. The parameter, r, named as preferential sputtering factor by Liau [11], is defined as the ratio of the ejection probability for the substrate atoms to that of the impurity atoms. For simplicity, let r = 1, i.e., no preferential sputtering. Combining Eqs. 7.6 and 7.7, we obtain

$$S_1(\Phi) = \frac{C_1(0,\Phi)}{C_o} S \qquad (7.8)$$

where $C_o = C_1(0,\Phi) + C_2(0,\Phi)$ is the total atomic concentration which is nearly constant, independent of Φ.

Substituting Eq. 7.8 into 7.5 and using the relation $C_1(0,\Phi) = Q(\Phi)/\sqrt{\pi\Phi\sigma}\,\ell$ from Eq. 7.4, we have

$$-\frac{d\,Q(\Phi)}{d\,\Phi} = \frac{S}{C_o\sqrt{\pi\Phi\sigma}\,\ell}\,Q(\Phi) \qquad (7.9)$$

The solution for this differential equation is

$$Q(\Phi) = Q_o\,e^{-k\sqrt{\Phi}} \qquad (7.10)$$

where $k = \frac{2S}{C_o\sqrt{\pi\sigma}\,\ell}$ and $Q_o = Q(0)$, the initial amount of impurity material. Finally, we can write down the impurity distribution function as follows:

$$C_1(x,t) = \frac{Q_o\,e^{-\frac{2\,S}{C_o\sqrt{\pi\sigma}\,\ell}\sqrt{\Phi}}}{\sqrt{\pi\Phi\sigma}\,\ell}\,e^{-\frac{x^2}{4\Phi\sigma\ell^2}} \qquad (7.11)$$

In this model, we have introduced three parameters S, ℓ and σ, which are all included in the exponent k $(= 2S/C_0\sqrt{\pi\sigma}\,\ell)$. According to Eqs. 7.10 and 7.11, the total impurity content $Q(\Phi)$ and concentration $C_1(x,\Phi)$ will decrease by an additional exponential factor $\exp(-k\sqrt{\Phi})$ if sputtering is included. On the other hand, $Q(\Phi)$ will decrease slower for larger value of ℓ (and hence small value of k) according to Eq. 7.10. Therefore, in order to retain high impurity content during ion-beam-mixing, implantation conditions shall be selected to facilitate diffusion (i.e., to maximize ℓ). For systems where radiation-enhanced diffusion is the dominant mechanism for mixing, this can be accomplished by keeping the sample at elevated temperature during ion bombardment.

7.3.2 An Example

An example of ion-beam-induced intermixing of a thin Pd film on a thick Ti substrate is presented in this section. The Pd-Ti system was chosen because it has been shown [1] that high-dose ion implantation of Pd into Ti can dramatically improve the aqueous corrosion resistance of Ti. Consequently, we have carried out experiments in the Pd-Ti system in an attempt to incorporate Pd into Ti by ion-beam-mixing process. Samples were 4000 Å Ti film deposited on a Si wafer and then coated with a thin Pd (∿200 Å) film on the top as shown in the inset of Fig. 7.5. Implantations were performed at R.T. or $200^{\circ}C$ with 300 keV Ar ions. The projected range of 300 keV Ar^+ into

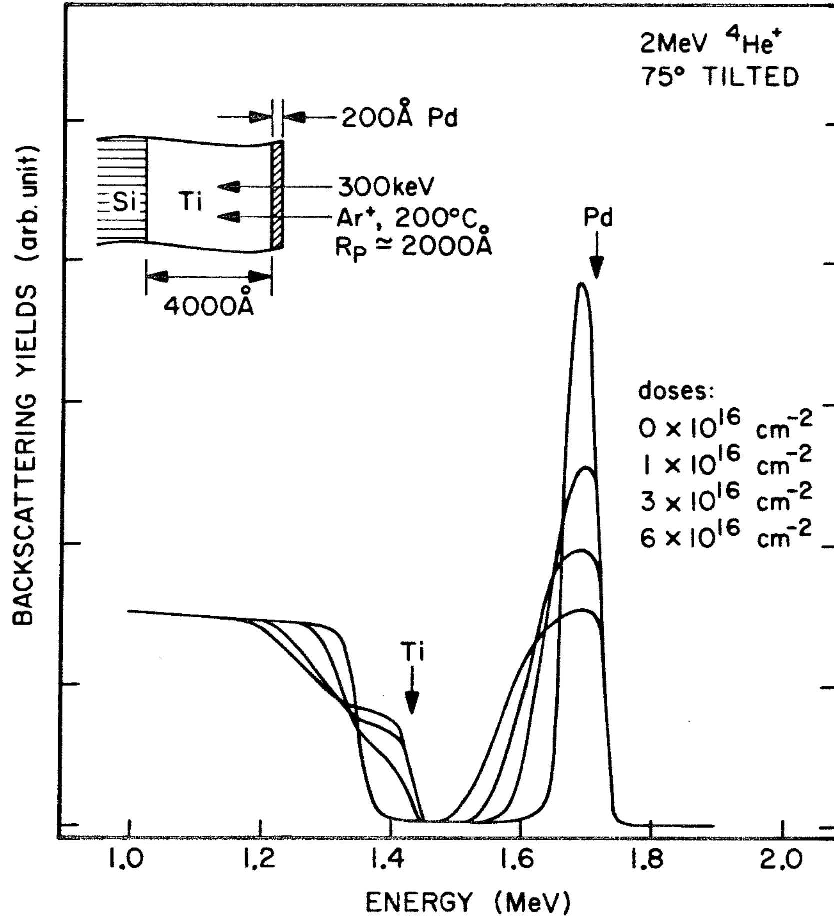

Fig. 7.5 Ion backscattering spetra of a thin Pd film on a thick Ti film after being bombarded with 300 keV Ar ions at 200°C to doses of 1, 3 and 6 x $1o^{16}$ cm^{-2}, respectively. The profile of intermixed Pd is similar to a Gaussian distribution.

Ti is ∿2000 Å, which is much greater than the Pd from thickness. Ion doses ranging from $5x10^{15}cm^{-2}$ to $6x10^{16}cm^{-2}$ were used.

Figure 7.5 shows the backscattering spectra of the Pd/Ti samples bombarded at $200^{o}C$ to doses of 1, 3 and $6x10^{16}cm^{-2}$, respectively. The Pd film has been mixed with Ti and spread progressively into deeper regions of the Ti substrate. As can be seen in the spectra, the evolution of Pd profile during the mixing is similar to the diffusion of a thin surface source with a Gaussian distribution.

To compare the experimental results with the model, the total amount of Pd atoms per cm^2, Q_{Pd}, were measured from the integrated Pd signals in the spectra for various ion doses. Figure 7.6 shows the plot of normalized Q_{Pd} (in log-scale) versus square root of ion-dose $\sqrt{\Phi}$. Two sets of data points are shown for samples implanted at R.T. and $200^{o}C$, respectively. In both cases, a straight line is least-square fitted to the data points. According to Eq. 7.10, Q_{Pd} shall fall off exponentially with $\sqrt{\Phi}$ and the experimental results agree well with the model prediction as shown in Fig. 7.6. The exponent k's, measured from the slope of the lines, are $5.3x10^{-10}cm$ and $3.1x10^{-10}cm$, for R.T. implantation and $200^{o}C$ implantation, respectively. The difference in the k value is most likely caused by the variation of mixing parameter ℓ with implantation temperature. The ℓ is expected to be larger at higher temperature since mixing can be enhanced due to the increased atomic mobility. We note that Pd forms solid solutions and a few inter-metallic compounds with Ti, and this temperature-enhancement effect, similar to that observed in

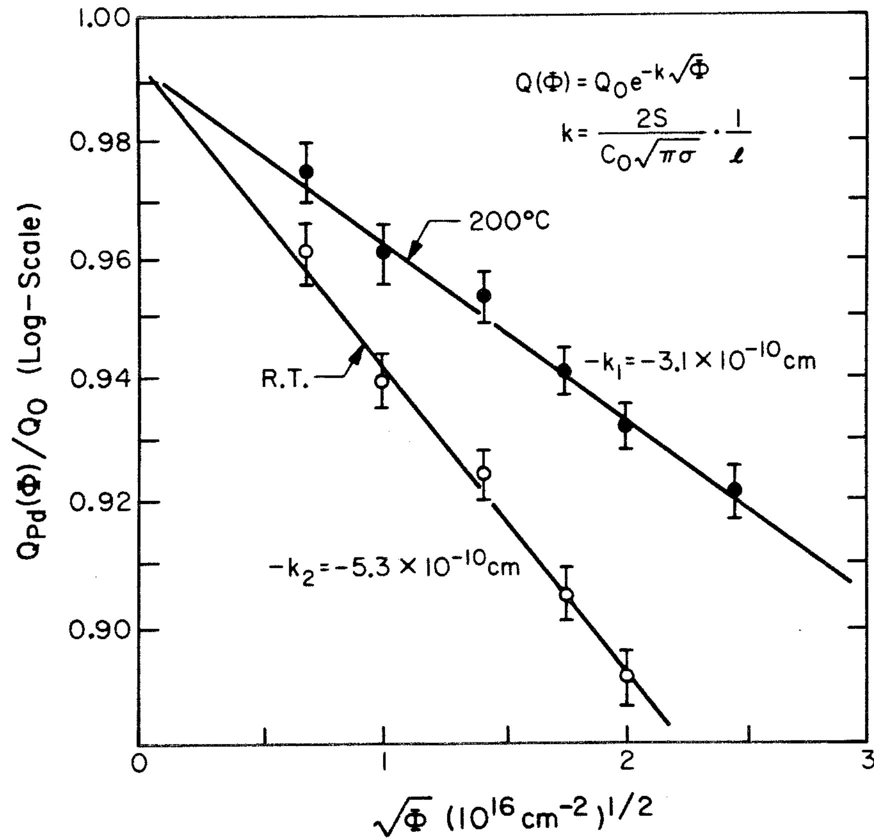

Fig. 7.6 Normalized Pd atoms per cm^2, Q_{Pd}, as a function of the square of ion dose $\sqrt{\Phi}$. The experimental results agree well with the model prediction.

the silicide forming systems, is predicted to be present. Notice that extrapolation of the two straight lines to zero ion dose does not yield a value of unity, contrary to the result obtained from Eq. 7.10. This is because at low ion doses the assumption of treating the film as an infinitesimal thin diffusion source is not valid. In fact, mixing starts near the Pd-Ti interface, rapidly consuming all the Pd because of the small film thickness and then a Pd-Ti mixed layer is formed. Good agreement between the model and the experimental results is found at high implantation ion doses.

The surface concentration of Pd has also been measured from the backscattering spectra and is plotted in Fig. 7.7 against ion dose. According to Eq. 7.11, the surface concentration $C_1(0,\Phi)$ should be proportional to $Q_{Pd}(\Phi)$ and inversely proportional to $\sqrt{\Phi}\ \ell$ as indicated by the function form shown in the plot. This function form is represented by the two solid curves in the plot using the k values determined from Fig. 7.6. The same normalization factor was used for these two curves to achieve a best match with the data points. For hot ($200^{o}C$) implants, the Pd concentration decreases more rapidly than R.T. implants because of the higher mixing efficiency (i.e., large ℓ). As a consequence, the total Pd concentration, Q_{Pd}, should, on the contrary, decrease slower (Fig. 7.6) for the hot implants because the sputter yield S_1, which is proportional to $C_1(0,\Phi)$ (Eq. 7.7), is smaller.

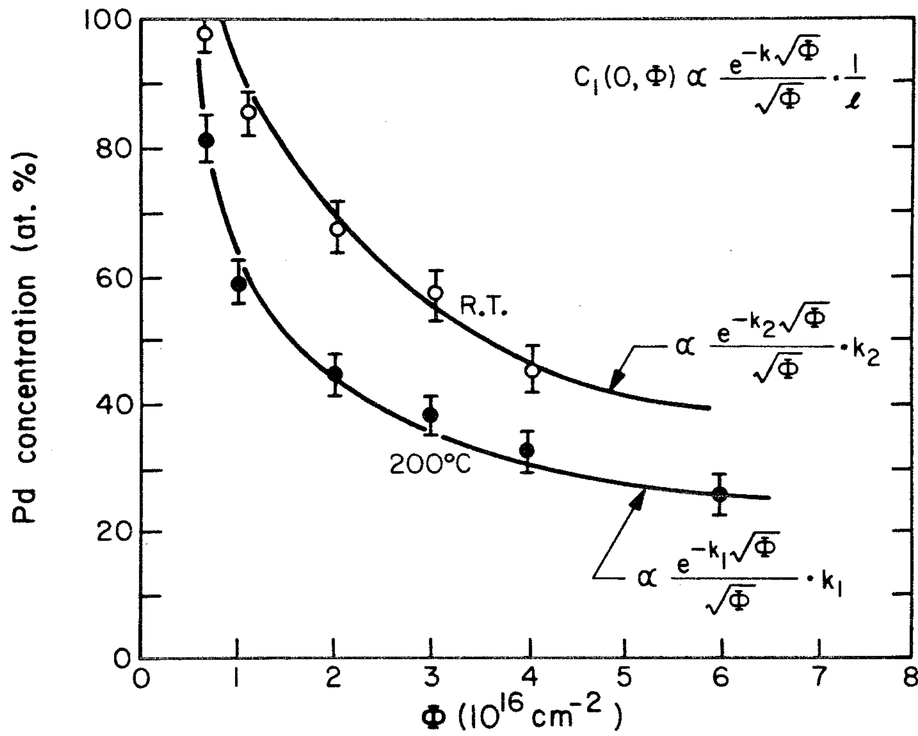

Fig. 7.7 Measured Pd surface concentration $C_1(0,\Phi)$ as a function of ion dose. The solid curves reprent the function form $e^{-k\sqrt{\Phi}}/\sqrt{\Phi}\ell$ using the k value determined from Fig. 7.6.

7.4 Discussion and Conclusion

Finally, we would like to compare the processes of direct implantation and ion-beam-mixing in introducing impurities into a substrate material. Their advantages and limitations will be discussed with emphasis on the aspect of ion-beam material surface modification.

Ion implantation is direct doping of near-surface region of a solid by implanting energetic ion species. The implanted species can be any element in the periodic table as long as ions can be generated. The profile of the implanted species is well approximated by a Gaussian distribution at low doping concentration on the order of 0.1 at.%. The corresponding ion doses are of the order of $\sim 10^{15} cm^{-2}$ or less. However, the use of ion implantation for metallurgical purpose calls for implanted concentration of a few atomic percent. This requires ion doses around 10^{17} ions cm^{-2}. At such high doses, sputtering and atomic mixing will become important in determining the profile of the implanted species. This phenomenon has been the subject of many recent investigations[6, 12-14]. Briefly speaking, the implanted species usually exhibit an approximately constant profile in the surface region as a result of sputtering and atomic mixing at high ion doses. Moreover, the maximum attainable concentration is limited by the sputtering process. The simplest estimate [15] gives the concentration of implanted species to be 1/S, where S is the sputtering yield or number of target atoms removed for an incident ion.

In the case of ion-beam-mixing, incorporation of impurities into a substrate by implanting through a thin film requires "interdiffusion" of atomic species within the collision cascades generated by the incident ions. The mechanisms involved in the mixing process consist of dynamic cascade mixing and radiation-enhanced diffusion (Chapter 2). Depending upon the implantation condition and material properties, one mechanism may dominate, while in some cases both are equally important. For systems where interdiffusion of the two elements is thermodynamically favorable such as due to compound (equilibrium or nonequilibrium) or alloy formation, mixing can usually be enhanced by increasing the substrate temperature during ion bombardment. Radiation-enhanced diffusion is the dominant mechanism for mixing at high temperatures in this case. However, for systems lacking the thermodynamic driving force such as immiscible systems, this temperature-enhancement effect of mixing is less likely to exist. The mixing in this case is predominantly contributed from dynamic cascade mixing which depends mainly on the ion energy and masses of projectile and target materials. The general observation is that, for energetic (say 300 keV) heavy ion (such as Xe) bombardment, the amount of atoms intermixed for one incident ion ranges from 10 to 200 for various systems we have studied. Therefore, ion-beam-mixing, generally speaking, is a more efficient process in introducing impurities into a substrate than direct implantation. However, optimization of mixing process by properly selecting implantation conditions requires knowledge of metallurgical properties of the system which is not important for direct implantation.

As a comparison, we show in Fig. 7.8 a plot of Au concentration versus ion dose for a Cu substrate incorporated with Au by direct implantation with 150 keV Au ions or by ion-beam-mixing of a 200 Å Au film with 300 keV Xe ions. By direct implantation, the Au concentration reaches a constant level of ∿5 at.% at dose levels of $\sim 10^{17}$ ions cm^{-2}. The sputtering yield of Cu for 150 keV Au^+ has been measured to be ∿20 [6]. Therefore, the maximum attainable Au concentration ($1/S \simeq 0.05$) is limited by the sputtering process. However, high concentration of Au in Cu can be achieved by ion-beam-mixing. The schematic diagrams in Fig. 7.8 indicate that at low doses, intermixing (or interdiffusion) is confined to the interface region; at higher doses, the Au layer is intermixed with Cu at concentrations dependent on the ion dose (solid curves), at even higher doses sputter erosion will determine concentration.

Another approach to produce alloyed layers on the surface of a metal by ion-beam-mixing is to utilize multiple-layered structure described in Chapter 6. This scheme is particularly useful for systems where mixing can not be enhanced at elevated implantation temperature due to the lack of thermodynamic driving force such as immiscible systems of Ag-Ni and Cu-Ta. Control of alloy composition and depth profile are much more versatile than that in the case of single-layered structure. Aside from the productions of metastable phases (Chapter 6),we believe the multiple-layer scheme may have potential in material surface modification as well.

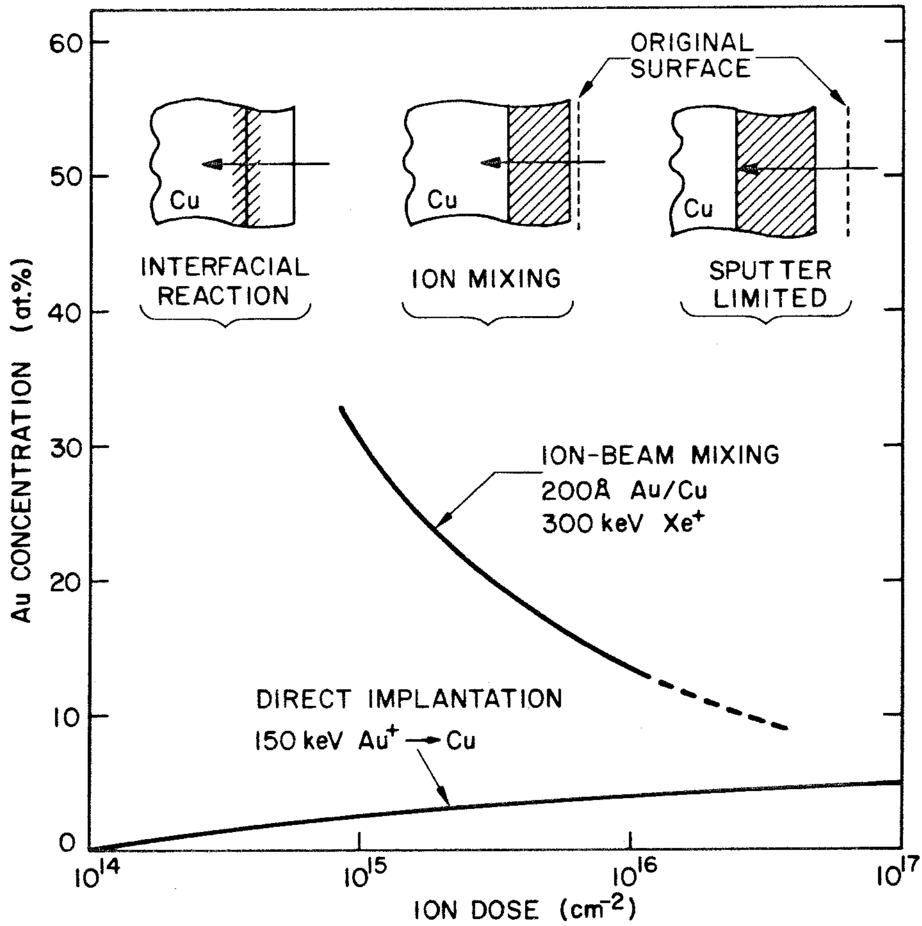

Fig. 7.8 Concentration versus dose for a Au film, 200 Å thick, ion-mixed with 300 keV Xe^+ ions. The lower curve is for the direct implantation of 150 keV Au ions (from Ref. 5).

The intrinsic limitation of direct implantation for material surface modification is the requirement of high implantation doses to achieve desirable concentrations (a few atomic percent or more). To reduce implantation time, the use of high current ion beams are required, but they are difficult to obtain especially when metal sources are used. This sets a strict restraint on using direct implantation for large area surface modification.

The limitation of ion-beam-mixing is that it can only be applied in cases where the doping species can be deposited as a thin film. The efficiency of mixing depends on the metallurgical properties of the system and it varies from system to system. This induces complications in selecting implantation conditions to optimize the mixing process. Furthermore, estimation of impurity concentration during the mixing process is more involved than that in the case of direct implantation. Precise compositional control can be accomplished by using multiple-layered structure although sample preparations are somewhat laborious in this case. However, from a practical point of view, the ion-beam-mixing techniques exhibit many attractive features. First, high concentration of impurity can be achieved at relatively low dose levels so that implantation time can be drastically reduced. Second, simple ion sources such as gas ions can be used and high current beams shall be easily obtained. This promises to be a method for large area surface modification and mass production. Further investigations along this direction are being conducted.

References

1. J. K. Hirvonen, J. Vac. Sci. Technol. 15, 1662 (1978).

2. N. E. W. Hartley, Thin Solid Films 64, 177 (1979).

3. J. A. Borders, in Annual Review of Materials Science, 9, R. A. Huggins, R. H. Bube and D. A. Vermilyea, Eds., (Annual Reviews, Inc., Palo Alto, California, 1979) p. 313.

4. W. A. Grant, J. Vac. Sci. Technol. 15, 1644 (1978).

5. J. M. Poate, J. Vac. Sci. Technol. 15, 1636 (1978).

6. Z. L. Liau and J. W. Mayer, J. Vac. Sci. Technol. 15, 1629 (1978).

7. J. A. Border and J. M. Poate, Phy. Rev. B 13, 963 (1976).

8. J. A. Poate, J. A. Border, A. G. Cullis and J. V. Hirvonen, Appl. Phys. Lett. 30, 365 (1977).

9. P. G. Shewmon, Diffusion in Solids (McGraw-Hill Book Company, 1963) p. 7.

10. See, for example, J. Mathews and R. L. Walker, Mathematical Methods of Physics , (W. A. Benjamin Inc., Menlo Park, California, 1972) p. 379.

11. Z. L. Liau, Thesis, California Institute of Technology, 1979.

12. G. Carter, J. N. Baruah and W. A. Grant, Rad. Eff. 16, 107 (1972).

13. F. Schulz and K. Wittmaack, Rad. Eff. 29, 31 (1976).

14. P. Blank, K. Wittmaack and F. Schulz, Nucl. Ins. Meth. 132, 387 (1976).

15. G. Carter, J. S. Calligon and J. H. Lesk, Proc. Phys. Soc. 79, 299 (1962).